

# **Field Line Resonance in Two and a Half Dimensions**

**DRAFT VERSION CREATED ON APRIL 12, 2016**

1

© Charles A. McEachern 2016

2



3

The text of this work is licensed under a Creative Commons

Attribution-ShareAlike 4.0 International license.

4

# <sup>5</sup> Acknowledgements

<sup>6</sup> Acknowledgement placeholder.

<sup>7</sup> MSI.

<sup>8</sup> Aaron, Scott, Sheng.

<sup>9</sup> Bob.

<sup>10</sup> John.

<sup>11</sup> Lei.

<sup>12</sup> Ian.

# <sup>13</sup> Dedication

<sup>14</sup> Dedication placeholder.

**Abstract**

<sup>16</sup> Abstract placeholder.

# <sup>17</sup> Contents

<sup>18</sup> Acknowledgements	i
<sup>19</sup> Dedication	ii
<sup>20</sup> Abstract	iii
<sup>21</sup> List of Tables	vii
<sup>22</sup> List of Figures	viii
<sup>23</sup> 1 Introduction	1
24 1.1 Structure of the Present Work . . . . .	2
<sup>25</sup> 2 The Near-Earth Environment	4
26 2.1 The Outer Magnetosphere . . . . .	5
27 2.2 The Inner Magnetosphere . . . . .	7
28 2.3 The Ionosphere . . . . .	8
29 2.4 Geomagnetic Storms and Substorms . . . . .	9
<sup>30</sup> 3 Field Line Resonance	12
31 3.1 Harmonic Structure . . . . .	16
32 3.2 Azimuthal Modenumber . . . . .	18
33 3.3 Poloidal and Toroidal Polarizations . . . . .	20
34 3.4 Giant Pulsations . . . . .	22
35 3.5 Motivations for the Present Work . . . . .	23

36	<b>4 Waves in Cold Resistive Plasma</b>	<b>25</b>
37	4.1 Guided Propagation . . . . .	27
38	4.2 Compressional Propagation . . . . .	28
39	4.3 High Altitude Limit . . . . .	30
40	4.4 Implications to the Present Work . . . . .	31
41	<b>5 “Tuna Half” Dimensional Model</b>	<b>33</b>
42	5.1 Coordinate System . . . . .	34
43	5.2 Physical Parameter Profiles . . . . .	38
44	5.3 Driving . . . . .	41
45	5.4 Maxwell’s Equations . . . . .	44
46	5.5 Boundary Conditions . . . . .	48
47	<b>6 Electron Inertial Effects</b>	<b>53</b>
48	6.1 The Boris Factor . . . . .	54
49	6.2 Parallel Currents and Electric Fields . . . . .	56
50	6.3 Inertial Length Scales . . . . .	61
51	6.4 Discussion . . . . .	63
52	<b>7 Numerical Results</b>	<b>65</b>
53	7.1 Modenumber and Compression . . . . .	65
54	7.2 Resonance and Rotation on the Dayside . . . . .	71
55	7.3 Resonance and Rotation on the Nightside . . . . .	78
56	7.4 Ground Signatures and Giant Pulsations . . . . .	82
57	7.5 Discussion . . . . .	86
58	<b>8 Van Allen Probe Observations</b>	<b>88</b>
59	8.1 Sampling Bias and Event Selection . . . . .	89
60	8.2 Events by Mode . . . . .	92
61	8.3 Events by Amplitude . . . . .	97
62	8.4 Events by Frequency . . . . .	102
63	8.5 Events by Phase . . . . .	106
64	8.6 Discussion . . . . .	111

65	<b>9 Conclusion</b>	<b>112</b>
66	9.1 Summary of Results . . . . .	112
67	9.2 Future Work . . . . .	112
68	<b>References</b>	<b>114</b>

# <sup>69</sup> List of Tables

<sup>70</sup>	3.1 IAGA Magnetic Pulsation Frequency Bands . . . . .	14
<sup>71</sup>	5.1 Typical Parameters for the Tuna Density Profile . . . . .	39
<sup>72</sup>	5.2 Integrated Atmospheric Conductivity . . . . .	49

# **List of Figures**

74	2.1	Reconnection in the Outer Magnetosphere . . . . .	5
75	2.2	Structures in the Inner Magnetosphere . . . . .	7
76	3.1	Alfvén Bounce Frequencies . . . . .	15
77	3.2	First and Second Harmonic Resonances . . . . .	17
78	3.3	Azimuthal Modenumbers Viewed from the Pole . . . . .	19
79	3.4	Poloidal Mode Structure . . . . .	21
80	3.5	Toroidal Mode Structure . . . . .	22
81	4.1	Compressional Alfvén Wave Cutoff Frequencies . . . . .	32
82	5.1	Nonorthogonal Dipole Grid . . . . .	38
83	5.2	Alfvén Speed Profiles . . . . .	40
84	5.3	Ionospheric Conductivity Profiles . . . . .	41
85	5.4	Decreasing Penetration with Increasing Modenumber . . . . .	43
86	5.5	Sym-H for June 2013 Storm . . . . .	44
87	6.1	Plasma Frequency Profile . . . . .	55
88	6.2	Electric Field Snapshots . . . . .	57
89	6.3	Current and Poynting Flux at 100 km . . . . .	58
90	6.4	Current and Poynting Flux at 1000 km . . . . .	60
91	6.5	Power Density at the Ionosphere . . . . .	61
92	6.6	Parallel Electric Fields by Perpendicular Grid Resolution . . . . .	62
93	7.1	Magnetic Field Snapshots from a Small- $m$ Run . . . . .	68
94	7.2	Magnetic Field Snapshots from a Large- $m$ Run . . . . .	69
95	7.3	Compressional Coupling to the Poloidal Mode . . . . .	70
96	7.4	Dayside Poloidal and Toroidal Energy . . . . .	75

97	7.5 Dayside Poloidal Energy Distribution . . . . .	76
98	7.6 Dayside Toroidal Energy Distribution . . . . .	77
99	7.7 Nightside Poloidal and Toroidal Energy . . . . .	79
100	7.8 Nightside Poloidal Energy Distribution . . . . .	80
101	7.9 Nightside Toroidal Energy Distribution . . . . .	81
102	7.10 Dayside Ground Magnetic Fields . . . . .	84
103	7.11 Nightside Ground Magnetic Fields . . . . .	85
104	8.1 Distribution of Usable Van Allen Probe Data . . . . .	90
105	8.2 Rate of Pc4 Events . . . . .	93
106	8.3 Rate of Pc4 Events by Mode . . . . .	94
107	8.4 Rate of Double Pc4 Events by Parity and Storm Index . . . . .	96
108	8.5 Amplitude Distribution of Pc4 Events by Mode . . . . .	98
109	8.6 Waveforms and Spectra for a Strong Pc4 Event . . . . .	100
110	8.7 Rate of Pc4 Events by Mode and Amplitude . . . . .	101
111	8.8 Rate of Pc4 Events by Mode and Frequency . . . . .	104
112	8.9 Frequency Distribution of Pc4 Events by Mode . . . . .	105
113	8.10 Waveforms and Spectra for a Pc4 Event . . . . .	108
114	8.11 Phase Distribution of Pc4 Events by Mode . . . . .	109
115	8.12 Rate of Pc4 Events by Mode and Phase . . . . .	110

<sup>116</sup> **Chapter 1**

<sup>117</sup> **Introduction**

<sup>118</sup> 1859 was a pivotal year in human history. The United States moved steadily toward  
<sup>119</sup> the American Civil War, which would abolish slavery and consolidate the power of  
<sup>120</sup> the federal government. A slew of conflicts in Southern Europe set the stage for the  
<sup>121</sup> unification of Italy. The Taiping Civil War — one of the bloodiest conflicts of all time  
<sup>122</sup> — is considered by many to mark the beginning of modern Chinese history. Origin of  
<sup>123</sup> Species was published. The first transatlantic telegraph cable was laid.

<sup>124</sup> Meanwhile, ambivalent to humanity, the Sun belched an intense burst of charged par-  
<sup>125</sup> ticles and magnetic energy directly toward Earth. The resulting geomagnetic storm<sup>1</sup>  
<sup>126</sup> caused telegraph systems to fail across the Western hemisphere, electrocuting operators  
<sup>127</sup> and starting fires[35, 96]. Displays of the northern lights were visible as far south as  
<sup>128</sup> Cuba.

<sup>129</sup> The Solar Storm of 1859 was perhaps the most powerful in recorded history, but by no  
<sup>130</sup> means was it a one-time event. The Sun discharges hundreds of coronal mass ejections  
<sup>131</sup> (CMEs) per year, of all sizes, in all directions. In fact, a comparably large CME narrowly  
<sup>132</sup> missed Earth in 2012[72]. Had it not, it's estimated it would have caused widespread,  
<sup>133</sup> long-term electrical outages, with a damage toll on the order of  $10^{12}$  dollars[68].

---

<sup>1</sup>The Solar Storm of 1859 is also called the Carrington Event, after English astronomer Richard Carrington. He drew a connection between the storm's geomagnetic activity and the sunspots he had observed the day before.

134 The Sun’s extreme — and temperamental — effect on Earth’s magnetic environment  
135 makes a compelling case for the ongoing study of space weather. Such research has  
136 evolved over the past century from sunspot counts and compass readings to multi-  
137 satellite missions and supercomputer simulations. Modern methods have dramatically  
138 increased humanity’s understanding of the relationship between the Sun and the Earth;  
139 however, significant uncertainty continues to surround geomagnetic storms, substorms,  
140 and the various energy transport mechanisms that make them up.

141 The present work focuses in particular on the phenomenon of field line resonance: Alfvén  
142 waves bouncing between the northern and southern hemispheres. Such waves play an  
143 important part in the energization of magnetospheric particles, the transport of energy  
144 from high to low altitude, the precipitation of particles into the atmosphere, and the  
145 driving of currents at the top of the atmosphere. It is these currents which give rise to  
146 potentially-catastrophic magnetic disturbances at Earth’s surface.

147 The study of resonance in the near-Earth environment is furthermore valuable as a proxy  
148 for other (less-accessible) plasma environments. Similar waves occur in astrophysical  
149 plasmas, observation of which is limited by distance. Field line resonance is also analo-  
150 gous to the so-called “fishbone instability” in fusion reactors. As a plasma laboratory,  
151 the magnetosphere is unique in that it is both close enough to measure directly, and  
152 also large enough that measurements can be performed without disrupting its behavior.

## 153 1.1 Structure of the Present Work

154 The present work is laid out as follows.

155 Chapter 2 surveys the near-Earth environment. Prominent features of the magneto-  
156 sphere are defined. The behavior of the magnetosphere during geomagnetic storms and  
157 substorms is summarized.

158 Chapter 3 introduces the field line resonance phenomenon, in terms of both the under-  
159 lying physics and notable work on the topic. Jargon is introduced to clarify important  
160 elements of wave structure. Several open questions about field line resonances (FLRs)  
161 are offered as motivations for the present work.

162 Chapter 4 lays the groundwork for a numerical model by exploring the fundamental  
163 equations of waves in a cold, resistive plasma — such as Earth’s magnetosphere. Char-  
164 acteristic scales are gleaned from the resulting dispersion relations.

165 Chapter 5 presents Tuna, a new two and a half dimensional simulation designed specif-  
166 ically for the realistic modeling of FLRs. Tuna’s non-orthogonal geometry, height-  
167 resolved ionosphere, novel driving mechanism, and coupling to the atmosphere are jus-  
168 tified and explained.

169 Chapter 6 considers the addition of electron inertial effects to Tuna, which are neglected  
170 in the core model presented in Chapter 5. These effects allow the computation of parallel  
171 currents and electric fields, which have not previously been included in global Alfvén  
172 models. The effects are shown to be instability-prone and computationally expensive,  
173 but some results are gleaned nonetheless.

174 Chapter 7 showcases the core numerical results of the present work, unifying several of  
175 the questions posed in Chapter 3. The interplay between compressional propagation,  
176 poloidal-to-toroidal rotation, and Joule dissipation is considered from several angles.

177 Chapter 8 puts the numerical results in context through the analysis of data from the  
178 Van Allen Probes mission. FLR occurrence rates are considered in terms of location,  
179 harmonic, and polarization, parameters which have been only partially addressed in  
180 past FLR surveys.

181 Chapter 9 briefly summarizes the results shown in the above chapters — code devel-  
182 opment, analysis of numerical results, and satellite observation — and suggests further  
183 directions.

<sup>184</sup> **Chapter 2**

<sup>185</sup> **The Near-Earth Environment**

<sup>186</sup> From Earth’s surface to a height of a hundred kilometers or so, the atmosphere is a  
<sup>187</sup> well-behaved fluid: a collisional ensemble of neutral atoms. Higher up, its behavior  
<sup>188</sup> changes dramatically. As altitude increases, solar ultraviolet radiation becomes more  
<sup>189</sup> intense, which ionizes atmospheric atoms and molecules. Density also decreases, slow-  
<sup>190</sup> ing collisional recombination. Whereas the neutral atmosphere is held against Earth’s  
<sup>191</sup> surface by gravity, the motion of charged particles is dominated by Earth’s geomagnetic  
<sup>192</sup> field, as well as the electromagnetic disturbances created as that field is hammered by  
<sup>193</sup> the solar wind.

<sup>194</sup> Before discussing specific interactions, it’s appropriate to introduce the so-called “frozen-  
<sup>195</sup> in condition.” In a collisionless plasma, magnetic field lines are equipotential contours.  
<sup>196</sup> Charged particles move freely along the contours, but cannot move across them. Com-  
<sup>197</sup> pression of the magnetic field is synonymous with compression of the ambient plasma,  
<sup>198</sup> as any magnetic field lines that thread a moving plasma are dragged along with it. This  
<sup>199</sup> assumption is valid throughout most of the magnetosphere — that is, the region of  
<sup>200</sup> space primarily governed by Earth’s magnetic field — and provides an invaluable tool  
<sup>201</sup> for understanding the large-scale motions of plasmas and fields.

## 2.1 The Outer Magnetosphere

Plasma behavior within Earth's magnetosphere is ultimately driven by the solar wind: a hot ( $\sim 100$  eV), fast-moving ( $\sim 100$  km/s) plasma threaded by the interplanetary magnetic field ( $\sim 10$  nT)<sup>1</sup>. The density of the solar wind is on the order of  $10^3$  /cm<sup>3</sup>; in a laboratory setting, this would constitute an ultra-high vacuum (atmospheric density at sea level is  $\sim 10^{19}$  /cm<sup>3</sup>), but compared to much of the magnetopause it's quite dense.

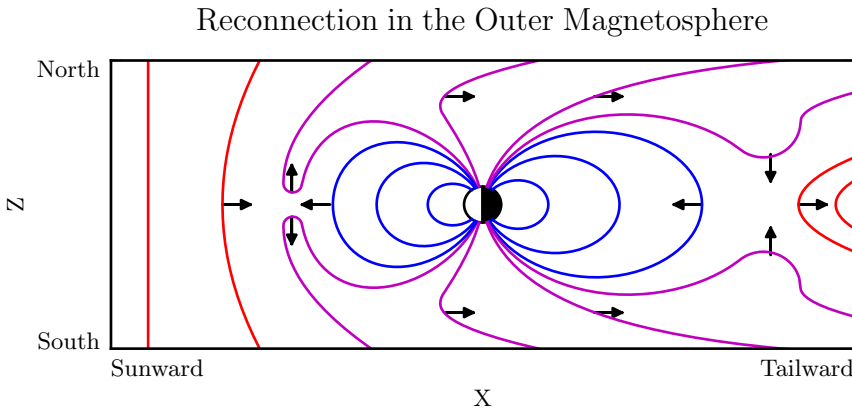


Figure 2.1: When the solar wind magnetic field (red) points southward, reconnection can occur between it and Earth's (northward) closed magnetic field lines (blue). The resulting open field lines (magenta) convect nightward over the poles, ultimately arriving in the magnetotail. There, the open field lines reconnect again. Newly closed field lines move Earthward, carrying flux across the flanks and back to the dayside. The rest are completely decoupled from Earth, and are lost to the solar wind.

- The magnetosphere's outer boundary represents a balance between the solar wind dynamic pressure and the magnetic pressure of Earth's dipole field. On the dayside, the dipole is compressed, pushing this boundary to within about  $10 R_E$  of Earth<sup>2</sup>. The nightside magnetosphere is stretched into a long tail which may exceed  $50 R_E$  in width and  $100 R_E$  in length.
- When the interplanetary magnetic field opposes the geomagnetic field at the nose of the magnetosphere, magnetic reconnection occurs. Closed magnetospheric field lines

<sup>1</sup>Listed values correspond to the solar wind at Earth's orbit.

<sup>2</sup>Distances in the magnetosphere are typically measured in units of Earth radii:  $1 R_E \equiv 6378$  km.

215 “break,” opening up to the interplanetary magnetic field<sup>3</sup>. They then move tailward  
216 across the poles, dragging their frozen-in plasma with them. Reconnection in the tail  
217 allows magnetic field lines to convect back to the day side, across the flanks. This  
218 process is called the Dungey cycle[21].

Viewed from the north, the Dungey cycle involves a clockwise flow of flux and plasma on  
the dusk side and a counterclockwise flow on the dawn side. The motion is accompanied  
by a convection electric field, per Ohm’s law in an ideal plasma:

$$\underline{E} + \underline{U} \times \underline{B} = 0 \quad (2.1)$$

219 Where  $\underline{B}$ ,  $\underline{E}$ , and  $\underline{U}$  are the magnetic field, electric field, and plasma velocity vectors  
220 respectively.

221 Consistent with Ampère’s law, the interplanetary magnetic field is separated from the  
222 magnetosphere by a current sheet: the magnetopause. On the dayside, the magne-  
223 topause current flows duskward; on the nightside, it flows downward around the mag-  
224 netotail.

225 Earth’s dipole is significantly deformed in the magnetotail; field lines in the northern  
226 lobe of the tail points more or less Earthward, and vice versa. Plasma within the lobes  
227 is cool ( $\sim 100$  eV) and rarefied ( $\sim 10^{-2}$  /cm<sup>3</sup>). The two lobes are divided by the plasma  
228 sheet, which is comparably hot ( $\sim 10^3$  eV) and dense ( $\sim 1$  /cm<sup>3</sup>). The plasma sheet  
229 carries a duskward current which connects to the magnetopause current.

---

<sup>3</sup>Closed field lines are more or less dipolar; one end connects to the north pole of Earth’s magnetic core, and the other end to the south pole. Open field lines are tethered to Earth at one end. In principle, the other end eventually doubles back to Earth, but for practical purposes it is lost to the solar wind. The distinction is important because charged particle motion is guided by magnetic field lines, as discussed in Chapter 3.

## 2.2 The Inner Magnetosphere

Within  $L \sim 8$  (where  $L$  is the McIlwain parameter<sup>4</sup>), the dipole magnetic field is not appreciably deformed by the solar wind. As a result, the structures in the inner magnetosphere follow closely from the motion of charged particles in an ideal dipole field.

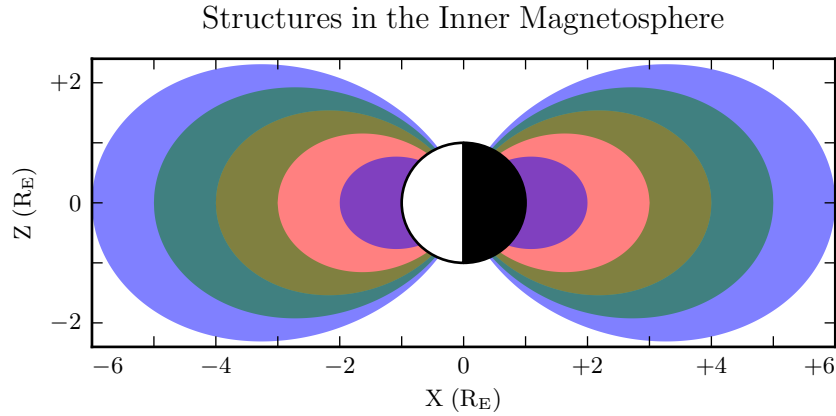


Figure 2.2: The above figure shows typical ranges in  $L$  for the plasmasphere (red,  $L < 4$ ), ring current (green,  $3 < L < 5$ ) and radiation belts (blue,  $L < 2$  and  $4 < L < 6$ ). These values, particularly the size of the plasmasphere, can vary significantly in response to geomagnetic activity.

The plasmasphere — a cold ( $\sim 1$  eV), dense ( $10^2 / \text{cm}^3$  to  $10^4 / \text{cm}^3$ ) torus of corotating plasma — is formed by the outward drift of atmospheric ions along magnetic closed field lines. Its outer boundary is thought to represent a balance between the corotation electric field (per the rotation of Earth's magnetic dipole) and the convection electric field (associated with the convection of magnetic flux during the Dungey cycle). Particle density drops sharply at the edge of the plasmasphere; the boundary is called the plasmapause. The plasmapause typically falls around  $L = 4$ , though during prolonged quiet times it can extend to  $L = 6$  or larger.

---

<sup>4</sup>The McIlwain parameter  $L$  is used to index field lines in Earth's dipole geometry:  $L \equiv \frac{r}{\sin^2 \theta}$  for colatitude  $\theta$  and radius  $r$  in Earth radii. For example, the  $L = 5$  field line passes through the equatorial plane at a geocentric radius of  $5 R_E$ , then meets the Earth at a colatitude of  $\arcsin \sqrt{\frac{1}{5}} \sim 27^\circ$  (equally, a latitude of  $\arccos \sqrt{\frac{1}{5}} \sim 63^\circ$ ).

242 Energetic particles trapped within the inner magnetosphere are divided into two popu-  
243 lations.

244 The Van Allen radiation belts are made up of particles with energy above  $10^5$  eV or  
245 so. The inner belt ( $L \lesssim 2$ ) is primarily composed of protons, the decay remnants of  
246 neutrons freed from the atmosphere by cosmic rays. The outer belt ( $L \gtrsim 4$ ) is primarily  
247 composed of high-energy electrons. The density of radiation belt particles is significantly  
248 affected by geomagnetic storms and substorms; a typical value is  $10 / \text{cm}^3$ .

249 Particles with energies of  $10^3$  eV to  $10^5$  eV make up the ring current, which extends  
250 from  $L \sim 3$  to  $L \sim 5$ . Gradient-curvature drift carries ions and electrons in opposite  
251 directions; the net result is a westward current. During quiet times, the ring current  
252 causes magnetic a southward magnetic field on the order of 1 nT at Earth's equator,  
253 while during geomagnetically active times (discussed in Section 2.4) the effect may be  
254 100 nT or more<sup>5</sup>.

## 255 2.3 The Ionosphere

256 Earth's neutral atmosphere is an excellent insulator. Collisions are so frequent that  
257 charged particles quickly thermalize and recombine. The breakdown of air molecules  
258 into a conductive plasma (as happens during a lightning strike, for example) requires  
259 electric fields on the order of  $10^9$  mV/m.

260 Cold particles in the magnetosphere are likewise not conducive to currents. In the  
261 absence of collisions, electrons and ions drift alongside one another in response to an  
262 electric field, creating no net current perpendicular to the magnetic field<sup>6</sup>. Magnetic  
263 field lines can typically be considered as equipotential contours, devoid of field-aligned  
264 potential structures.

265 The ionosphere is a sweet spot between the two regimes. Collisions are frequent enough  
266 to disrupt the drift of ions, but not frequent enough to immobilize the electrons. The

---

<sup>5</sup>For comparison, Earth's dipole field points north at the equator with a magnitude over  $10^4$  nT.

<sup>6</sup>The so-called  $E$ -cross- $B$  drift is associated with a velocity of  $\underline{U} = \frac{1}{B^2} \underline{E} \times \underline{B}$ , independent of a charged particle's mass or sign.

267 result is a finite-valued conductivity tensor. Pedersen currents (which scale with the  
268 Pedersen conductivity) flow in the direction of the perpendicular electric field. Hall  
269 currents (due to the Hall conductivity) flow in the  $\underline{B} \times \underline{E}$ . It is these currents — par-  
270 ticularly the Hall current — which give rise to magnetic fields at the ground. Collisions  
271 in the ionosphere also result in a finite parallel conductivity, allowing for the formation  
272 of potential structures along the magnetic field line.

273 The convection electric field (associated with the Dungey cycle, Section 2.1) drives  
274 Pedersen currents in the ionosphere. Pedersen currents flow downward on the flanks  
275 and duskward across the poles. The currents remain divergence-free by connecting  
276 to field-aligned currents at the edges of the polar cap. The field-aligned currents, in  
277 turn, connect to the magnetopause current, the cross-tail current, and the (partial) ring  
278 current.

279 When electron density is low, thermal velocities may be unable to carry enough current  
280 to satisfy  $\nabla \cdot \underline{J} = 0$ . This leads to the formation of potential structures along geomagnetic  
281 field lines in the ionosphere. Such structures accelerate particles along magnetic field  
282 lines, leading to the precipitation of energetic particles into the atmosphere. As the  
283 particles thermalize, they excite atmospheric atoms. The resulting spontaneous emission  
284 is often in the visible spectrum, giving rise to the aurora.

## 285 2.4 Geomagnetic Storms and Substorms

286 The quiet geomagnetic behavior described above is periodically disturbed by transient  
287 solar phenomena such as corotating interaction regions (CIRs) and coronal mass ejec-  
288 tions (CMEs). CMEs, such as the one that caused the Solar Storm of 1859 mentioned  
289 in Chapter 1, are bursts of unusually dense solar wind which are ejected from regions of  
290 high magnetic activity on the Sun; they are most common at the height of the eleven-  
291 year solar cycle. CIRs, on the other hand, occur when a relatively fast region of the  
292 solar wind catches up to an earlier and slower-moving pocket of solar wind, resulting in  
293 a pair of shockwaves.

294 During a storm, increased solar wind intensity results in enhanced magnetic reconnection  
295 on the dayside. As the newly-opened field lines are swept tailward, the convection  
296 electric field is strengthened. The plasmasphere — the outer boundary of which is set by  
297 a balance between the convection electric field and the (more or less constant) corotation  
298 electric field — sheds its outer layers[33]. A large number of energetic particles are also  
299 injected into the ring current[69].

300 The strength of the storm is gauged by the size of the magnetic perturbation created  
301 by the ring current<sup>7</sup>. A small storm has a magnitude of 50 nT to 100 nT. Large storms  
302 may reach 250 nT to 500 nT. The Carrington Event, mentioned in Chapter 1, is thought  
303 to have exceeded 1700 nT[96].

304 The main phase of a storm typically lasts for several hours. Storm recovery — the  
305 gradual return of the storm index to zero, and the refilling of the plasmasphere — lasts  
306 several days. Geomagnetic storms occur tens of times per year at the height of the solar  
307 cycle, and just a few times per year otherwise.

308 Whereas storms are prompted by large solar wind events on the dayside, geomagnetic  
309 substorms are primarily a nightside occurrence. As flux accumulates in the tail, mag-  
310 netic tension builds in the stretched field lines. A substorm is an impulsive release of  
311 that tension.

312 At substorm onset, a burst of reconnection occurs in the tail. A jet of plasma is launched  
313 Earthward from the reconnection site (and another is launched tailward, and lost to the  
314 solar wind). The Earthward plasma injection injects particles into the ring current.  
315 The outer radiation belt is depleted, then repopulated. Energetic particles precipitate  
316 into the atmosphere, giving rise to a distinctive sequence of auroral signatures over the  
317 course of about an hour.

318 Concurrent with substorm onset, impulsive Alfvén waves are observed with periods of  
319 a minute or two. The precise ordering of events — whether reconnection causes the  
320 waves, or vice versa, or if they share a common cause — remains controversial.

---

<sup>7</sup>The most commonly used storm index is DST, which is computed hourly using measurements from several ground magnetometers near the equator. The Sym-H index, used in Section 5.3, is computed once per minute.

- 321 Each substorm lasts several hours, including the time it takes for the ring current to  
322 return to pre-substorm levels. Several substorms may occur per day during quiet times.  
323 During a storm, substorms become far more frequent; by the time one has ended,  
324 another may have already begun.

<sup>325</sup> **Chapter 3**

<sup>326</sup> **Field Line Resonance**

<sup>327</sup> The motion of a charged particle in a dipole field can be described in terms of three  
<sup>328</sup> fundamental motions.

<sup>329</sup> The first is cyclotron motion. Given a uniform magnetic field line, a particle follows a  
<sup>330</sup> helical path. It moves in a circular path in a plane normal to the magnetic field line,  
<sup>331</sup> and keeps a constant velocity along the direction of the field. Close to Earth, where the  
<sup>332</sup> magnetic field is strongest, the proton (electron) cyclotron timescale is on the order of  
<sup>333</sup>  $10^{-3}$  s ( $10^{-6}$  s); at  $L \sim 5$ , a typical value is closer to 10 s ( $10^4$  s).

<sup>334</sup> The second fundamental motion is bounce motion. As it moves along the magnetic field  
<sup>335</sup> line like a bead on a wire, the particle experiences a change in magnetic field magnitude.

<sup>336</sup> In order to conserve its magnetic moment (also called the first adiabatic invariant), the  
<sup>337</sup> particle's perpendicular kinetic energy increases in proportion with the magnetic field.

<sup>338</sup> When the perpendicular kinetic energy can no longer increase — that is, when all of  
<sup>339</sup> the particle's kinetic energy is perpendicular — the particle bounces back. Particles  
<sup>340</sup> undergoing bounce motion continuously move back and forth between the northern and  
<sup>341</sup> southern hemispheres, with timescales of a few seconds to a few minutes.

<sup>342</sup> Particles with more parallel kinetic energy (compared to their perpendicular kinetic  
<sup>343</sup> energy) bounce at lower altitudes. If the particle's motion is sufficiently field-aligned, the

344 bounce altitude drops into the atmosphere, and the particle is collisionally thermalized.

345 This process is called precipitation.

346 The third fundamental motion is drift motion. Over the course of a particle's cyclotron  
347 motion, the Earthward half of the orbit experiences a slightly stronger magnetic field  
348 (and thus a slightly smaller orbit radius). The net effect, called the gradient-curvature  
349 drift, is an azimuthal motion around Earth on timescales of  $\sim 10^3$  s.

350 Wave-particle resonance arises when a particle's periodic motion matches with the fre-  
351 quency of a coincident electromagnetic wave[23, 65, 74, 85]. In the particle's rest frame,  
352 the wave then appears as a net electric field. This allows a net movement of energy  
353 between the wave and the particle. The interaction is analogous to a surfer moving  
354 along with — and being accelerated by — a wave in the ocean. Such resonance can  
355 arise for any of the three fundamental motions, or even for a combination of them.

356 In the present work, the waves under consideration are field line resonances (FLRs). An  
357 FLR is a standing harmonic on a geomagnetic field line. It can also be envisioned as  
358 a superposition of traveling waves, reflecting back and forth between its northern and  
359 southern foot points at the conducting ionosphere.

These waves travel at the Alfvén speed,  $v_A$ , defined per

$$v_A^2 \equiv \frac{B^2}{\mu_0 \rho} \quad \text{or, equally,} \quad v_A^2 \equiv \frac{1}{\mu_0 \epsilon_{\perp}} \quad (3.1)$$

360 Where  $B$  is the magnetic field magnitude,  $\rho$  is the mass density, and  $\mu_0$  is the magnetic  
361 constant. The perpendicular electric constant  $\epsilon_{\perp}$  is analogous to the electric constant  
362  $\epsilon_0$ , and arises in cases (such as the magnetosphere) where a dielectric medium exhibits  
363 a preferred direction. In the magnetosphere, mass density and magnetic field strength  
364 depend strongly on position. As a result, the Alfvén speed varies by several orders  
365 of magnitude over the length of a field line. The fundamental equations of field line  
366 resonance were presented by Dungey in 1954[20]. Since then, they have remained a  
367 topic of active study.

368 So-called ultra low frequency waves — of which FLRs are a subset — are categorized  
 369 by morphology. Continuous (long-lived) pulsations are termed Pc, while irregular pulsations  
 370 are called Pi. Within each are a number of frequency bands; see Table 3.1[45].  
 371 In practice, frequency demarcations are not strict, but rather serve as a heuristic for  
 372 grouping phenomenologically similar waves[42].

Table 3.1: IAGA Magnetic Pulsation Frequency Bands

	Pc1	Pc2	Pc3	Pc4	Pc5	Pi1	Pi2
Period (s)	0.2–5	5–10	10–45	45–150	150–600	1–40	40–150
Frequency (mHz)	200–5000	100–200	22–100	7–22	2–7	25–1000	7–25

373 FLRs fall into the Pc3, Pc4, and Pc5 ranges. The present work focuses specifically  
 374 on the Pc4 band: waves with periods of a minute or two. Frequencies in the Pc4  
 375 range typically coincide with Alfvén bounce times<sup>1</sup> near the plasmapause:  $L \sim 4$  to  
 376  $L \sim 6$ [2, 16, 24, 57]<sup>2</sup>. In fact, the large radial gradients in the Alfvén speed near the  
 377 plasmapause act as an effective potential well, trapping FLRs[15, 50, 54, 55, 64, 88].

378 In addition to being radially localized, FLRs in the Pc4 frequency band (also called Pc4  
 379 pulsations, or just Pc4s) are localized in magnetic local time (MLT<sup>3</sup>). They have also  
 380 been shown to occur preferentially on the dayside, during storms or storm recovery[2,  
 381 16, 24, 53, 57, 97].

382 In the inner magnetosphere, the Alfvén frequency — and thus the frequency of FLRs  
 383 — often coincides with integer or half-integer<sup>4</sup> multiples of particle drift frequencies[17].  
 384 The resulting wave-particle interactions can give rise to significant energization and ra-  
 385 dial diffusion of the particles. In some cases, the waves also include an electric field  
 386 parallel to the background magnetic field, breaking the assumption that magnetic field

<sup>1</sup>The Alfvén frequency is the inverse of the Alfvén bounce time:  $\frac{2\pi}{\omega_A} \equiv \oint \frac{dz}{v_A}$ .

<sup>2</sup>Not coincidentally, these are the same  $L$ -shells where the Van Allen Probes spend most of their time; see Chapter 8.

<sup>3</sup>Noon points toward the Sun and midnight away from it, with 06:00 and 18:00 at the respective dawn and dusk flanks.

<sup>4</sup>See Section 3.1.

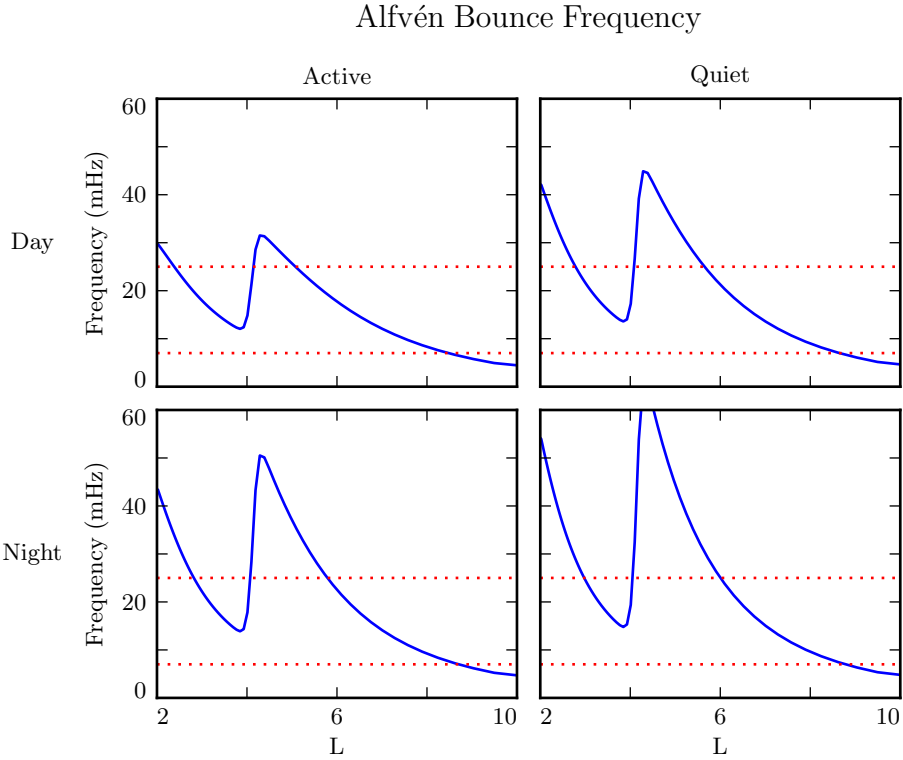


Figure 3.1: The above are bounce frequencies for an Alfvén wave moving back and forth along a geomagnetic field line. Alfvén speeds are computed based on profiles from Kelley[48], as discussed in Section 5.2. Notably, the bounce frequency depends significantly on the position of the plasmasphere, taken here to be at  $L = 4$ . Dotted lines indicate the Pc4 frequency range: 7 mHz to 25 mHz.

387 lines are equipotential contours, and contributing to the precipitation of energetic par-  
 388 ticles into the neutral atmosphere[31, 32, 94, 103].

389 The present chapter introduces the structural characteristics of FLRs, how those charac-  
 390 teristics affect wave behavior, and several unresolved questions related to that behavior.

<sub>391</sub> **3.1 Harmonic Structure**

<sub>392</sub> Wave structure along a geomagnetic field line is indicated by harmonic number. The  
<sub>393</sub> first (or fundamental) harmonic has a wavelength twice as long as the field line. The  
<sub>394</sub> electric field perturbation is zero at the ionospheric foot points of the field line, due to  
<sub>395</sub> the conductivity of the ionosphere. For the first harmonic, this puts an electric field  
<sub>396</sub> antinode at the equator, along with a node in the perpendicular<sup>5</sup> perturbation to the  
<sub>397</sub> magnetic field. For the second harmonic, the electric field has a third node at the  
<sub>398</sub> equator, in addition to the two at the ionospheric foot points, which is accompanied by  
<sub>399</sub> an antinode in the perpendicular wave magnetic field. Figure 3.2 shows a qualitative  
<sub>400</sub> sketch of the first and second harmonics: a series of snapshots in time, in the rest frame  
<sub>401</sub> of the wave. Perpendicular electric and magnetic field perturbations are shown in blue  
<sub>402</sub> and red respectively.

<sub>403</sub> A first-harmonic FLR that is periodic or localized in the azimuthal direction is conducive  
<sub>404</sub> to drift-resonant wave-particle interactions[17, 75]. The particle is like a child on a swing:  
<sub>405</sub> whenever the path of the particle (or child) gets close to the wave (parent), it gets a  
<sub>406</sub> push, and always in the same direction. The wave fields spend half its time pointing  
<sub>407</sub> the other direction, just as the parent must shift their weight backward to get ready for  
<sub>408</sub> the next push, but at that point the particle (child) is far away.

<sub>409</sub> Second-harmonic FLRs interact with particles through the drift-bounce resonance, which  
<sub>410</sub> is slightly more complicated. As the particle drifts azimuthally, it also zig-zags north-  
<sub>411</sub> south. The combination of those two periodic motions must align with the phase of  
<sub>412</sub> the wave electric field. An example path is shown by the purple line in Figure 3.2:  
<sub>413</sub> the particle's drift and bounce motions together ensure that it experiences a rightward  
<sub>414</sub> electric field throughout the wave's oscillation.

The drift and drift-bounce resonance conditions is written, respectively[89]:

$$\omega - m\omega_D = 0 \quad \text{and} \quad \omega - m\omega_D = \omega_B \quad (3.2)$$

---

<sup>5</sup>The parallel, or compressional, wave magnetic field exhibits the same nodes and antinodes as the perpendicular electric field[78].

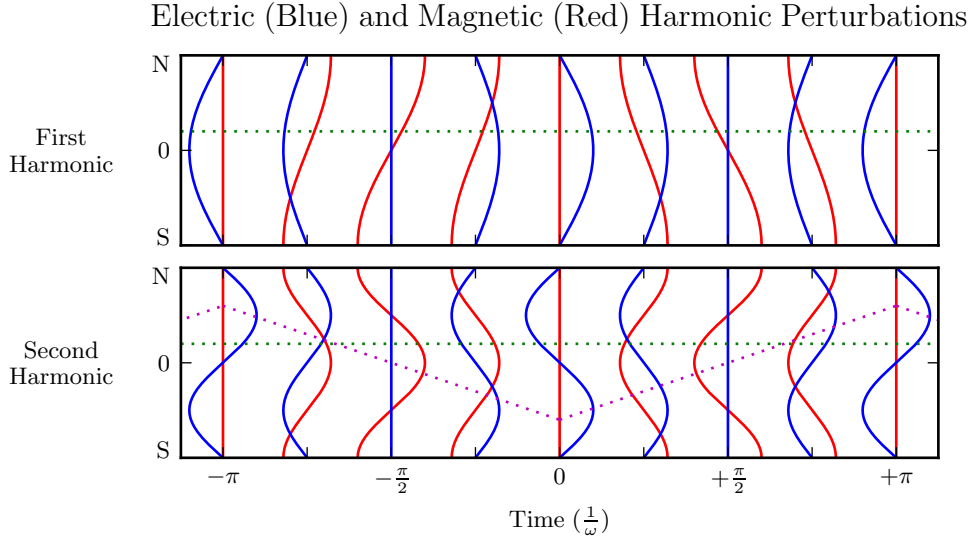


Figure 3.2: The first (or fundamental) harmonic has an antinode in its perpendicular electric field (blue) at the equator, along with a node in its perpendicular magnetic field perturbation (red). A single satellite can identify the first harmonic by the relative phase of the electric and magnetic field perturbations: an observer north of the equator (green) will see the magnetic field perturbation lead the electric field by  $\pm 90^\circ$ . The second harmonic is the opposite: it has an electric field node at the equator, and an observer north of the equator will see the magnetic field perturbation lag the electric field by  $\mp 90^\circ$ . Top and bottom signs correspond to the poloidal (shown) and toroidal polarizations respectively. The purple line sketches the path of a particle in drift-bounce resonance; in the particle's rest frame, the electric field is always to the right.

- 415    Where  $\omega$  is the frequency of the wave,  $\omega_D$  and  $\omega_B$  are the particle's drift and bounce
- 416    frequencies respectively, and  $m$  is the wave's azimuthal modenumber, as discussed in
- 417    Section 3.2.
- 418    In principle, the first and second harmonics can be distinguished by their frequencies,
- 419    even from a single-point observation[2, 14, 34]. In practice, however, this is not a reliable
- 420    approach[90]. Significant uncertainties surround the mass density profile — and thus
- 421    the Alfvén speed profile — along a geomagnetic field line.
- 422    Harmonic structure can also be deduced by noting the phase offset between the wave
- 423    magnetic field and its electric field (or the plasma velocity)[16, 93]. In Figure 3.2, the
- 424    green line indicates an observer just north of the magnetic equator. For a wave polarized

425 in the poloidal direction (see Section 3.3), the observer sees the electric field waveform  
426 offset from the magnetic field by a phase of  $\pm 90^\circ$ , where the top sign is for odd modes  
427 and the bottom sign is for even modes. The signs are flipped for toroidally-polarized  
428 waves, and again for waves observed south of the equator.

429 In addition to a wave’s parity, the phase indicates how energy is divided between stand-  
430 ing and traveling waves. Standing waves (phase of  $\pm 90^\circ$ ) have a purely imaginary  
431 Poynting flux. Traveling waves (phase of  $0^\circ$  or  $180^\circ$ ), on the other hand, have real  
432 Poynting flux, indicating a net movement of energy. Wave lifetimes can be estimated  
433 by comparing the energy density to the rate at which that energy is carried away by  
434 Poynting flux, as is done in Chapter 8.

435 Notably, the measurement of wave phase has only become viable with the advent of  
436 satellites carrying both electric and magnetic field instrumentation, such as THEMIS in  
437 2007[3] and the Van Allen Probes (formerly RBSP, for Radiation Belt Storm Probes)  
438 in 2012[86].

439 Strictly speaking, the the phase offset of the electric and magnetic fields does not provide  
440 the harmonic number — only its parity. It’s reasonably safe to assume that an even mode  
441 is the second harmonic; the second harmonic is by far the most commonly observed[44,  
442 83, 91], due in part to its excitement by the antisymmetric balloon instability[9, 11,  
443 12, 85]. However, the distinction between the first and third harmonics is not always  
444 clear[13, 34]; this issue is discussed further in Chapter 8. Higher harmonics than that  
445 are not expected in the Pc4 frequency band.

## 446 3.2 Azimuthal Modenumber

447 The wavelength of an FLR in the azimuthal direction is indicated by its azimuthal  
448 modenumber. A wave with modenumber  $m$  has an azimuthal wavelength that spans  $\frac{24}{m}$   
449 hours in MLT.

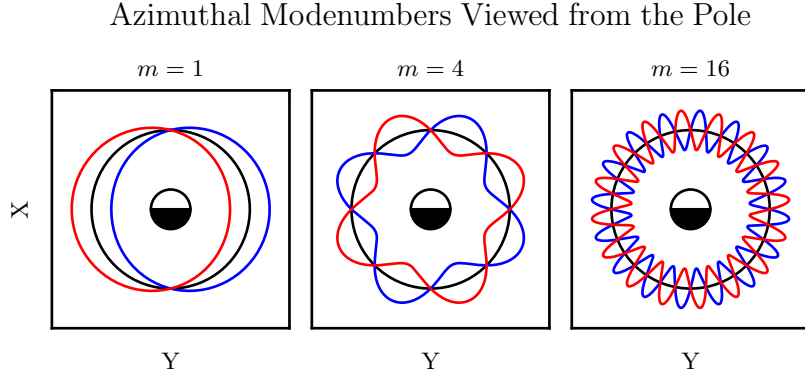


Figure 3.3: Above are qualitative sketches of waves with azimuthal modenumbers 1, 4, and 16, projected into the ecliptic plane. Black circles show unperturbed fields, while the blue and red curves show perturbations. At  $m = 1$ , the wave is more or less a uniform displacement, while at  $m = 16$  azimuthal variations take place on spatial scales small compared to Earth's radius.

- 450 Waves with small azimuthal modenumbers ( $0 < m < 10$ ) are typically driven by broad-  
 451 band energy sources at the magnetosphere's boundary, such as variations in the so-  
 452 lar wind pressure[18, 38, 49, 106, 107], sporadic magnetic reconnection[42], or Kelvin-  
 453 Helmholtz waves on the magnetopause[10, 58, 84]. In the low- $m$  regime, the shear and  
 454 compressional Alfvén waves are coupled, which allows energy to move across field lines  
 455 until the driving frequency lines up with the local Alfvén frequency[60]. Because of their  
 456 broadband energy source, low- $m$  FLRs often have a mishmash of frequencies present in  
 457 their spectra[16], though the spectra are coherent in terms of harmonic[25].
- 458 When the azimuthal modenumber is large (or, equally, when the azimuthal wavelength  
 459 is small), compressional propagation of Alfvén waves becomes evanescent, so the move-  
 460 ment of energy is guided by magnetic field lines[14, 78]<sup>6</sup>. As a result, FLRs must be  
 461 driven from within the magnetosphere. Proposed energy sources include phase space  
 462 gradients near the plasmapause[17], particularly as the plasmasphere refills after a storm  
 463 or substorm[24, 56].

---

<sup>6</sup>Equally, the strength of a wave's parallel component indicates its modenumber, a point which is revisited in Chapters 7 and 8.

464 The atmosphere is known to attenuate waves with small spatial extent in the perpendic-  
465 ular direction[43, 101, 105]. As a result, FLRs may create no signature on the ground if  
466 their azimuthal modenumber is large. For example, a recent paper by Takahashi shows  
467 a strong (2 nT at  $L \sim 10$ ), clear resonance with  $|m| \gtrsim 70$  and no corresponding ground  
468 signature[90].

Southwood[85] and Glassmeier[29] show that a low frequency wave passing through the ionosphere on its way to Earth will be attenuated per

$$\frac{B_E}{B_I} = \frac{\Sigma_H}{\Sigma_P} \exp\left(-m \frac{R_I - R_E}{R_E \sin \theta}\right) \quad (3.3)$$

469 Where  $B_E$  and  $B_I$  are the magnetic field strengths at  $R_E$  (Earth's surface, 6783 km  
470 geocentric) and  $R_I$  (the ionosphere,  $\sim$ 6900 km geocentric) respectively. The integrated  
471 ionospheric Pedersen and Hall conductivities,  $\Sigma_P$  and  $\Sigma_H$ , are typically within a factor  
472 of two of one another. Field lines near the plasmapause can be traced to Earth at  
473  $\sin \theta \sim 0.4$ . That is, by the time it reaches the ground, the magnetic field from an FLR  
474 with  $m = 10$  is weaker by a factor of two; at  $m = 100$ , the factor is closer to 100.

### 475 3.3 Poloidal and Toroidal Polarizations

476 Based on polarization, each FLR can be classified as either poloidal or toroidal. The  
477 poloidal mode is a field line displacement in the meridional plane, as shown in Figure 3.4,  
478 with an accompanying electric field in the azimuthal direction. The toroidal mode's  
479 magnetic displacement is azimuthal, per Figure 3.5; the associated electric field is in the  
480 meridional plane.

481 Both poloidal and toroidal waves are noted for their ability to contribute to the energiza-  
482 tion and radial diffusion of trapped particles. The poloidal mode interacts more strongly,  
483 since its electric field is aligned with the trapped particles' drift motion. Poloidally-  
484 polarized waves are also more prone to creating magnetic signatures on the ground, due  
485 to ducting in the ionosphere[27, 36].

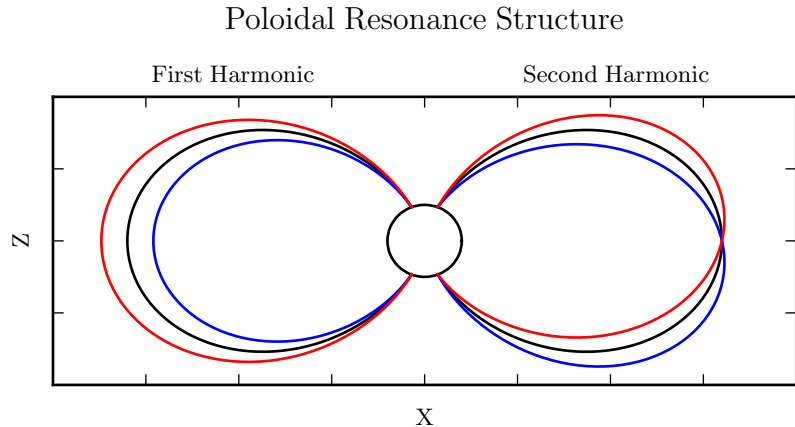


Figure 3.4: The poloidal resonance is a magnetic field in the meridional plane. The displacement is radial near the equator, and can be accompanied by enhancement in the parallel magnetic field near the ionosphere. The first harmonic is shown on the left, and the second harmonic on the right. Lines are colored red and blue only to contrast with the unperturbed black field line.

- 486 Toroidal modes have been shown to outnumber poloidal modes[2]. Perhaps not co-  
 487 incidentally, poloidally-polarized waves rotate asymptotically to the toroidal mode[66,  
 488 67, 78]. Poloidal waves with low azimuthal modenumber — such as those driven by  
 489 broadband sources at the magnetopause — rotate on timescales comparable to their  
 490 oscillation periods. The two modes are also coupled directly by the ionospheric Hall  
 491 conductivity[47].
- 492 The eigenfrequencies for poloidal and toroidal FLRs are similar, though not identical[34].  
 493 It has furthermore been noted that toroidally-polarized waves exhibit a strong relation-  
 494 ship between frequency and  $L$ -shell (or latitude), while poloidal waves at fixed frequency  
 495 are spread more broadly in  $L$ [25].

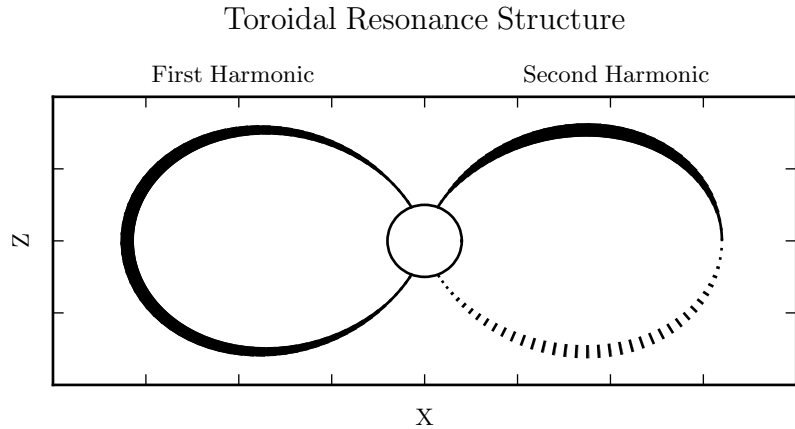


Figure 3.5: A toroidally-polarized FLR has a magnetic perturbation in the azimuthal direction, as shown. Bold lines are taken to be above the page, and dotted lines below the page, with the displacement indicated by the line’s width. The first harmonic — where the entire field line oscillates in and out of the page — is shown on the left. The second harmonic is on the right, with northern and southern halves perturbed in opposite directions.

### 496 3.4 Giant Pulsations

497 The study of geomagnetic pulsations long predates satellites, sounding rockets, or even  
498 the word “magnetohydrodynamics”<sup>7</sup>. Large, regular oscillations in the magnetic field  
499 were noted as early as 1901[5]. Eventually, the term “giant pulsation,” or Pg, arose to  
500 describe such pulsations.

501 On the ground, Pgs are notable for their strikingly sinusoidal waveforms, their eastward  
502 drifts, and their specific occurrence pattern: Pgs are typically seen pre-dawn, at latitudes  
503 of  $60^\circ$  to  $70^\circ$ . Pgs generally fall into the Pc4 frequency band<sup>8</sup>. Their harmonic structure  
504 was a source of controversy for decades, but recent multisatellite observations seem to be  
505 in agreement that they are odd harmonics, probably fundamental[30, 40, 52, 53, 89, 93].  
506 They are poloidally polarized, with modenumbers  $10 \lesssim m \lesssim 40$ [28, 40, 75, 81, 93].

---

<sup>7</sup>The term was first used by Alfvén in the 1940s[1].

<sup>8</sup>The Pc4 range is periods of 45 s to 140 s, while Pgs range from 60 s to 200 s[7].

507 Whereas FLRs are waves in space which may produce ground signatures, “giant pulsation” refers to the ground signature specifically<sup>9</sup>. That is, Takahashi’s satellite observation of a sinusoidal, morningside, high- $m$ , fundamental poloidal resonance was not  
508  
509  
510 classified as a Pg because it did not produce a signal on the ground[90].

511 Due to their remarkably clear waveforms, Pgs are typically found by “visual inspection  
512 of magnetometer data”[70]. Over the course of the past century, a number of multi-year  
513 (sometimes multi-decade[7]) surveys have totaled nearly one thousand Pg events. On  
514 average, a ground magnetometer near 66° magnetic latitude observes  $\sim$ 10 Pg events per  
515 year[7, 39, 80, 87]. Observations are not distributed uniformly; rather, giant pulsations  
516 are most common near the equinox and during times of low solar activity.

517 Unlike Pc4 pulsations in general, Pgs show no particular correlation with storm phase[70].  
518 However, they do often occur as the magnetosphere recovers from a substom[70, 81].

### 519 3.5 Motivations for the Present Work

520 A great deal has been learned — and continues to be learned — through observations of  
521 field line resonance. However, the cost-to-benefit ratio is climbing. As summarized in the  
522 sections above, FLR behavior depends significantly on harmonic structure, azimuthal  
523 modenumber, and polarization — not to mention frequency, spectral width, and so  
524 on. With each degree of freedom comes the necessity for an additional simultaneous  
525 observation.

526 Similarly, as FLRs have been shown to depend on ever-more-specific magnetospheric  
527 conditions, analytical techniques have fallen out of favor. The height-resolved iono-  
528 sphere, multidimensional Alfvén speed profile, and inconvenient geometry combine to  
529 create a problem beyond the reasonable purview of pencil and paper.

530 That is, the topic of field line resonance is ripe for numerical modeling.

---

<sup>9</sup>Historically, the wave designations shown in Table 3.1 all referred to ground phenomena. Over time, they have come to describe satellite observations as well, including those without corresponding signatures on the ground.

531 Past models of the magnetosphere have been limited in their consideration of FLRs.  
532 Reasons include overly-simplified treatment of the ionospheric boundary, no consider-  
533 ation of the plasmapause, limited range in  $m$ , and the inability to compute ground  
534 signatures. Chapter 5 presents a model which addresses these issues, allowing the com-  
535 putation of field line resonance with unparalleled attention to realism.

536 The model allows a bird’s-eye view of the structure and evolution of FLRs. As such,  
537 not only can several open questions be addressed, but their answers serve to unify a  
538 number of seemingly-disparate properties described in the sections above.

539 The rotation of poloidally-polarized waves to the toroidal mode is investigated. Par-  
540 ticular attention is paid to the importance of azimuthal modenumber and ionospheric  
541 conductivity. The interplay between said rotation and the transport of energy across  
542 field lines — which also depends on azimuthal modenumber — is considered as well.

543 By their nature, drifting particles have the potential to spur wave-particle interactions  
544 at all MLT. However, Pc4 observations are strongly peaked on the dayside. In a 2015  
545 paper, Dai notes, “It is not clear why noncompressional [high- $m$ ] Pc4 poloidal waves,  
546 which are presumably driven by instability within the magnetosphere, preferentially  
547 occur on the dayside”[16]. Motoba, later that year, echoes, “It is unclear whether other  
548 generation mechanisms of fundamental standing waves ... can explain the localization  
549 of Pgs in local time”[70]. This, too, is considered numerically: to what degree is field  
550 line resonance affected by the (day-night asymmetric) conditions of the ionosphere?

551 An attempt is also made to demystify giant pulsations. It’s been shown that toroidal  
552 Pc4s outnumber poloidal ones, and that most poloidal Pc4s are even, so perhaps it  
553 should come as no surprise that (poloidal, odd) Pgs are rare. Is it truly the case that  
554 Pgs are only “a small subset of fundamental poloidal waves”[90], set apart from the rest  
555 by their distinctive properties? Or, said another way, to what degree do the properties  
556 associated with Pgs arise in fundamental poloidal waves overall?

557 **Chapter 4**

558 **Waves in Cold Resistive Plasma**

559 Before delving into the implementation of the numerical model, it's instructive to con-  
560 sider the fundamental equations of waves in a cold, resistive plasma. Specifically, the  
561 present chapter is concerned with waves much slower than the electron cyclotron fre-  
562 quency. High-frequency waves such as the L and R modes are beyond the scope of the  
563 present work — and, in fact, beyond the limits of the model described in Chapter 5.

The evolution of electric and magnetic fields is governed by Ampère's law and Faraday's law. Notably, the present work takes the linearized versions of Maxwell's equations; the vectors  $\underline{E}$  and  $\underline{B}$  indicate perturbations above the zeroth-order magnetic field.

$$\underline{\epsilon} \cdot \frac{\partial}{\partial t} \underline{E} = \frac{1}{\mu_0} \nabla \times \underline{B} - \underline{J} \quad \frac{\partial}{\partial t} \underline{B} = -\nabla \times \underline{E} \quad (4.1)$$

Current follows Ohm's law. For currents perpendicular to the background magnetic field, Kirchhoff's formulation is sufficient. Conductivity is much higher along the magnetic field lines<sup>1</sup>, so it's appropriate to also include the electron inertial term<sup>2</sup>.

$$0 = \underline{\sigma}_{\perp} \cdot \underline{E}_{\perp} - \underline{J}_{\perp} \quad \frac{1}{\nu} \frac{\partial}{\partial t} J_z = \sigma_0 E_z - J_z \quad (4.2)$$

---

<sup>1</sup>The dipole coordinate system is defined rigorously in Section 5.1; at present, it's sufficient to take  $\hat{z}$  parallel to the zeroth-order magnetic field, and  $\hat{x}$  and  $\hat{y}$  perpendicular to  $\hat{z}$  (and to each other).

<sup>2</sup>Electron inertial effects are not included in the model described in Chapter 5, or in the results in Chapter 7; however, their implementation and impact are explored in Chapter 6.

Derivatives in Equations (4.1) and (4.2) can be evaluated by performing a Fourier transform. They can then be combined, eliminating the magnetic field and current terms.

$$\begin{aligned} 0 &= \underline{\underline{E}}_{\perp} + \frac{v_A^2}{\omega^2} (\underline{k} \times \underline{k} \times \underline{E})_{\perp} + \frac{i}{\epsilon_{\perp}\omega} \underline{\sigma}_{\perp} \cdot \underline{\underline{E}}_{\perp} \\ 0 &= E_z + \frac{c^2}{\omega^2} (\underline{k} \times \underline{k} \times \underline{E})_z + \frac{i\omega_P^2}{\omega(\nu - i\omega)} E_z \end{aligned} \quad (4.3)$$

The speed of light, Alfvén speed (including the displacement current correction), plasma frequency, and parallel conductivity are defined in the usual way:

$$c^2 \equiv \frac{1}{\mu_0\epsilon_0} \quad v_A^2 \equiv \frac{1}{\mu_0\epsilon_{\perp}} \quad \omega_P^2 \equiv \frac{ne^2}{m_e\epsilon_0} \quad \sigma_0 \equiv \frac{ne^2}{m_e\nu} \quad (4.4)$$

Where the perpendicular dielectric constant  $\epsilon_{\perp}$  is analogous to the electric constant  $\epsilon_0$ , but for electric fields which are perpendicular to the preferred direction of the dielectric medium. As noted in Equation (3.1),  $\epsilon_{\perp} \equiv \frac{\rho}{B^2}$  where  $\rho$  is the mass density and  $B$  is the magnitude of the (zeroth-order) magnetic field.

Using the vector identity  $\underline{k} \times \underline{k} \times \underline{E} = \underline{k} \underline{k} \cdot \underline{E} - k^2 \underline{E}$ , Equation (4.3) can be reassembled into a single expression,

$$0 = \left( \underline{\underline{\mathbb{I}}} + \frac{1}{\omega^2} \underline{\underline{V}}^2 \cdot \underline{k} \underline{k} - \frac{k^2}{\omega^2} \underline{\underline{V}}^2 + \frac{i}{\omega} \underline{\underline{\Omega}} \right) \cdot \underline{E} \quad (4.5)$$

Where  $\underline{\underline{\mathbb{I}}}$  is the identity tensor and in  $x$ - $y$ - $z$  coordinates,

$$\underline{\underline{V}}^2 \equiv \begin{bmatrix} v_A^2 & 0 & 0 \\ 0 & v_A^2 & 0 \\ 0 & 0 & c^2 \end{bmatrix} \quad \text{and} \quad \underline{\underline{\Omega}} \equiv \begin{bmatrix} \frac{\sigma_P}{\epsilon_{\perp}} & \frac{-\sigma_H}{\epsilon_{\perp}} & 0 \\ \frac{\sigma_H}{\epsilon_{\perp}} & \frac{\sigma_P}{\epsilon_{\perp}} & 0 \\ 0 & 0 & \frac{\omega_P^2}{(\nu - i\omega)} \end{bmatrix} \quad (4.6)$$

In Equation (4.5), the expression in parentheses is the dispersion tensor. Nontrivial solutions exist only when its determinant is zero. This gives rise to a seventh-order polynomial in  $\omega$ , so rather than a direct solution it's necessary to consider limits of specific interest.

572 Without loss of generality, the wave vector  $\underline{k}$  may be taken to lie in the  $x$ - $z$  plane — that  
573 is, with  $k_y = 0$ . The distinction between the two perpendicular directions is discussed  
574 in Section 4.4.

## 575 4.1 Guided Propagation

576 The wave vector of a field line resonance aligns closely to the background magnetic  
577 field. By supposing that the two align exactly (that is, taking  $k_x = 0$ ), the parallel and  
578 perpendicular components of the dispersion relation are decoupled.

The parallel-polarized component — that is, the solution when  $E_x = E_y = 0$  — is quadratic, and thus can be solved directly.

$$0 = \omega^2 + i\nu\omega - \omega_P^2 \quad \text{so} \quad \omega = -\frac{i\nu}{2} \pm \sqrt{\omega_P^2 - \frac{\nu^2}{4}} \quad (4.7)$$

579 It bears noting that the plasma frequency is large — not just compared to Pc4 frequencies,  
580 but even compared to the collision frequencies in the ionosphere<sup>3</sup>.

Expanding Equation (4.7) with respect to large  $\omega_P$ , the dispersion relation becomes

$$\omega^2 = \omega_P^2 \pm i\nu\omega_P + \dots \quad (4.8)$$

581 Equation (4.8) can hardly be called a wave, as it does not depend on the wave vector  
582  $\underline{k}$ . Rather, it is the plasma oscillation<sup>4</sup>: electrons vibrating in response to a charge  
583 separation along the background magnetic field.

584 The plasma oscillation is not specifically relevant to the study of field line resonance.  
585 The two phenomena are separated by six orders of magnitude in frequency. The topic

---

<sup>3</sup>The collision frequency may match or exceed the plasma frequency for a thin slice at the bottom of the ionosphere, where the density of neutral atoms is large; however, it falls off quickly. Above an altitude of 200 km, conservatively[73], the plasma frequency exceeds the collision frequency by an order of magnitude or more.

<sup>4</sup>The plasma oscillation is also called the Langmuir wave, after Irving Langmuir.

586 is revisited in Chapter 6 insomuch as it is inseparable from the electron inertial effects  
587 in Ohm's law.

The perpendicular ( $E_z = 0$ ) components of the dispersion relation give an expression quartic in  $\omega$ .

$$0 = \omega^4 + 2i\frac{\sigma_P}{\epsilon_\perp}\omega^3 - \left(2k_z^2v_A^2 + \frac{\sigma_P^2 + \sigma_H^2}{\epsilon_\perp^2}\right)\omega^2 - 2ik_z^2v_A^2\frac{\sigma_P}{\epsilon_\perp}\omega + k_z^4v_A^4 \quad (4.9)$$

Like the parallel-polarized component above, Equation (4.9) can be solved directly. Noting that  $\pm$  and  $\oplus$  are independent,

$$\omega = \left(\frac{\pm\sigma_H - i\sigma_P}{2\epsilon_\perp}\right) \oplus \sqrt{k_z^2v_A^2 + \left(\frac{\pm\sigma_H - i\sigma_P}{2\epsilon_\perp}\right)^2} \quad (4.10)$$

Also like the parallel-polarized component, the exact solution is less useful than its Taylor expansion. The Pedersen and Hall conductivities are large near the ionospheric boundary, but fall off quickly; for the vast majority of the field line, the ratios  $\frac{\sigma_P}{\epsilon_\perp}$  and  $\frac{\sigma_H}{\epsilon_\perp}$  are small compared to field line resonance frequencies. Expanding with respect to small conductivity gives

$$\omega^2 = k_z^2v_A^2 \oplus k_zv_A\frac{\sigma_H \pm i\sigma_P}{\epsilon_\perp} + \dots \quad (4.11)$$

588 This is the shear Alfvén wave, with a shift to its frequency due to the conductivity of  
589 the ionosphere. It travels along the background magnetic field like a bead on a string,  
590 with electric and magnetic field perturbations perpendicular to the magnetic field line  
591 (and to one another).

## 592 4.2 Compressional Propagation

593 The partner to guided motion is compressional motion; in order for energy to move  
594 across field lines, the wave vector must have a component perpendicular to  $\hat{z}$ . If the

595 wave vector is completely perpendicular to the magnetic field line ( $k_z = 0$ ), the parallel  
 596 and perpendicular components of the dispersion relation decouple, as in Section 4.1.

The parallel-polarized ( $E_x = E_y = 0$ ) component of the dispersion relation is

$$0 = \omega^3 + i\nu\omega^2 - (k_x^2 c^2 + \omega_P^2) \omega - ik_x^2 c^2 \nu \quad (4.12)$$

Equation (4.12) can be solved directly, though its solution (as a cubic) is far too long to be useful. Expanding with respect to the large plasma frequency, gives

$$\omega^2 = k^2 c^2 + \omega_P^2 - i\nu\omega_P + \dots \quad (4.13)$$

597 This is the O mode, a compressional wave with an electric field perturbation along  
 598 the background magnetic field. Like the plasma oscillation discussed in Section 4.1, its  
 599 frequency is very large compared to that of a field line resonance.

The perpendicular-polarized ( $E_z = 0$ ) component of the compressional dispersion relation is also cubic.

$$0 = \omega^3 + 2i\frac{\sigma_P}{\epsilon_\perp}\omega^2 - \left(2k_x^2 v_A^2 + \frac{\sigma_P^2 + \sigma_H^2}{\epsilon_\perp^2}\right) \omega - ik_x^2 v_A^2 \frac{\sigma_P}{\epsilon_\perp} \quad (4.14)$$

A wave moving across magnetic field lines near the ionospheric boundary will encounter large  $\frac{\sigma_P}{\epsilon_\perp}$  and  $\frac{\sigma_H}{\epsilon_\perp}$ , while at moderate to high altitudes those ratios will be small. Solving Equation (4.14) in those two limits respectively gives:

$$\omega^2 = k_x^2 v_A^2 \pm ik_x v_A \frac{\sigma_P}{\epsilon_\perp} + \dots \quad \text{and} \quad \omega^2 = k_x^2 v_A^2 + \left(\frac{\sigma_H \pm i\sigma_P}{\epsilon_\perp}\right)^2 + \dots \quad (4.15)$$

600 At first glance, both limits of Equation (4.15) appear to describe a compressional Alfvén  
 601 wave. The magnetic perturbation is along the background magnetic field — indicating  
 602 compression of the frozen-in plasma — while the electric field perturbation is perpen-  
 603 dicular to both the magnetic field and the wave vector.

604 However, in the high-conductivity limit, the parenthetical term actually dominates the  
 605 Alfvén term, taking values as large as  $\sim 10^6$  Hz. Waves at such frequencies are beyond  
 606 the scope of the present work. As a matter of curiosity, however, it bears noting that  
 607 (as long as  $\nu \ll 10^6$  Hz)  $\frac{\sigma_H}{\epsilon_{\perp}}$  reduces to the electron cyclotron frequency,  $\frac{eB}{m_e}$ .

### 608 4.3 High Altitude Limit

609 In the limit of large radial distance, it's reasonable to take the collision frequency to  
 610 zero; doing so also neglects the Pedersen and Hall conductivities.

Whereas in Sections 4.1 and 4.2 it was the parallel-polarized component of the dispersion relation that factored out from the other two, the high altitude limit decouples the component polarized out of the  $x$ - $z$  plane. The  $y$ -polarized dispersion ( $E_x = E_z = 0$ ) is simply:

$$\omega^2 = k^2 v_A^2 \quad (4.16)$$

611 Equation (4.16) describes an Alfvén wave with an arbitrary angle of propagation. De-  
 612 pending on the angle between the wave vector and the background magnetic field, it  
 613 could be guided, compressional, or somewhere in between. Regardless of propagation  
 614 angle, the electric field perturbation is perpendicular to both the direction of propaga-  
 615 tion and the magnetic field perturbation.

The other two components (from  $E_y = 0$ ) of the high altitude dispersion tensor give an expression quadratic in  $\omega^2$ :

$$0 = \omega^4 - (k_x^2 c^2 + k_z^2 v_A^2 + \omega_P^2) \omega^2 + k_z^2 v_A^2 \omega_P^2 \quad (4.17)$$

Which can be solved for

$$\omega^2 = \frac{1}{2} (k_x^2 c^2 + k_z^2 v_A^2 + \omega_P^2) \pm \sqrt{\frac{1}{4} (k_x^2 c^2 + k_z^2 v_A^2 + \omega_P^2)^2 - k_z^2 v_A^2 \omega_P^2} \quad (4.18)$$

Noting again that  $\omega_P$  is very large, the two roots can be expanded to

$$\omega^2 = k_z^2 v_A^2 \left( 1 - \frac{k_x^2 c^2 + k_z^2 v_A^2}{\omega_P^2} \right) + \dots \quad \text{and} \quad \omega^2 = k_x^2 c^2 + k_z^2 v_A^2 + \omega_P^2 + \dots \quad (4.19)$$

- 616 The first solution of Equation (4.19) is a shear Alfvén wave, as in Equation (4.11).
- 617 Notably, this form arises only when the parenthetical quantity is close to unity — as it
- 618 is for FLRs. The inertial limit, where frequencies are close to the plasma frequency, is
- 619 beyond the scope of the present work. For that same reason, the second solution (which
- 620 describes an oscillation faster than the plasma frequency) is not further considered.

## 621 4.4 Implications to the Present Work

- 622 The present section's findings carry three significant implications for the present work.
- 623 First — with the exception of the plasma oscillation and similar modes, which are
- 624 revisited in Chapter 6 — waves propagate at the Alfvén speed. This, in combination
- 625 with the grid configuration, will constrain the time step that can be used to model them
- 626 numerically. The time step must be sufficiently small that information traveling at the
- 627 Alfvén speed cannot “skip over” entire grid cells<sup>5</sup>.

Second, the results of the present section allow an estimate of the magnitude of parallel electric field that might be expected from a field line resonance compared to its perpendicular electric field. Between the full dispersion tenfor form in Equation (4.5) and the Alfvén wave described by Equation (4.19),

$$\left| \frac{E_z}{E_x} \right| = \frac{k_x k_z c^2}{\omega^2 - k_x^2 c^2 - \omega_P^2} \sim \frac{k^2 c^2}{\omega_P^2} \quad (4.20)$$

- 628 In essence, the relative magnitudes of the parallel and perpendicular electric fields should
- 629 be in proportion to the square of the relative magnitudes of the electron inertial length

---

<sup>5</sup>As is the convention, the time step is scaled down from the smallest Alfvén zone crossing time by a Courant factor, typically 0.1, meaning that it takes at least ten time steps to cross a grid cell.

630 (1 km to 100 km) and the wavelength ( $\sim 10^5$  km). That is, parallel electric fields should  
 631 be smaller than the perpendicular electric fields by six or more orders of magnitude.

632 Finally, the dispersion relations shown above indicate how the behavior of a field line  
 633 resonance should behave as the azimuthal modenumber becomes large.

634 Whereas the shear Alfvén wave's dispersion relation depends only on the parallel com-  
 635 ponent of the wave vector, the compressional Alfvén wave depends on its magnitude:  
 636  $\omega^2 = k^2 v_A^2$ . If the frequency is smaller than  $k v_A$ , the wave will become evanescent. The  
 637 wave vector's magnitude can be no smaller than its smallest component, however, and  
 638 the azimuthal component scales with the azimuthal modenumber:  $k_y \sim \frac{m}{2\pi r}$ .

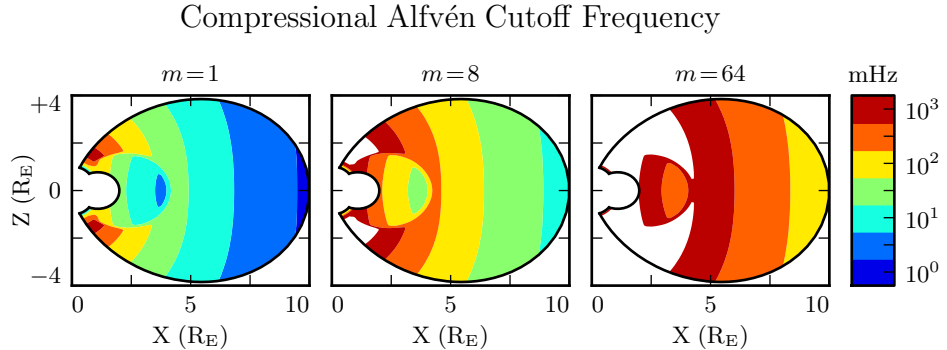


Figure 4.1: Taking  $k_y \sim \frac{m}{2\pi r}$  as a lower bound for the magnitude of the wave vector, the above figure demonstrates the lowest frequency at which compressional Alfvén waves may propagate as a function of position and  $m$ . Regions shown in white are off the color scale — they have a lower bound on the order of  $10^4$  mHz or more. The above Alfvén frequency profile is from Kelley[48], for quiet dayside conditions, as discussed in Section 5.2.

639 This imposes a frequency cutoff on compressional Alfvén waves which scales with the  
 640 azimuthal modenumber, as shown in Figure 4.1. At small values of  $m$ , most of the mag-  
 641 netosphere is conducive to compressional Alfvén waves in the Pc4 frequency range. As  
 642  $m$  increases, and the wave vector with it, the inner magnetosphere becomes increasingly  
 643 inaccessible to them.

644 **Chapter 5**

645 **“Tuna Half” Dimensional Model**

646 The present section describes the implementation of Tuna, a new two and a half dimensional  
647 Alfvén wave code based largely on work by Lysak[59, 63].

648 The half-integer dimensionality refers to the fact that Tuna’s spatial grid resolves a  
649 two-dimensional slice of the magnetosphere, but that electric and magnetic fields —  
650 as well as their curls — are three-dimensional vectors. This apparent contradiction is  
651 reconciled by the use of a fixed azimuthal modenumber,  $m$ . Electric and magnetic fields  
652 are taken to be complex-valued, varying azimuthally per  $\exp(im\phi)$ ; derivatives with  
653 respect to  $\phi$  are then replaced by a factor of  $im$ .

654 Unlike a fully three-dimensional code, Tuna cannot resolve the evolution of wave structures  
655 in the azimuthal direction. Furthermore, the model does not allow coupling between  
656 the dayside and nightside magnetospheres. What Tuna does offer is efficiency.  
657 The model’s economical geometry allows it to include a realistic Earthward boundary:  
658 grid spacing on the order of 10 km, a height-resolved ionospheric conductivity tensor,  
659 and even the computation of magnetic field signatures at the ground. Such features are  
660 computationally infeasible for a large global code.

661 Tuna was developed with field line resonance in mind. As discussed in Chapter 3,  
662 such waves are azimuthally localized, minimizing the importance of Tuna’s missing half  
663 dimension. Moreover, because field line resonances are known to be affected by both

664 the ionosphere and the plasmasphere, a faithful treatment of the inner magnetosphere  
665 is a crucial part of studying them numerically.

666 Perhaps the most exciting feature of Tuna is its novel driving mechanism: ring current  
667 perturbation. Codes similar to Tuna have traditionally been driven using compressional  
668 pulses at the outer boundary[59, 63, 99, 100]. This has precluded the investigation of  
669 waves with large azimuthal modenumber — such as giant pulsations — which are guided,  
670 and thus must be driven from within the magnetosphere.

671 TODO: The dipole geometry isn't super new, but it's not widely used. The height-  
672 resolved ionosphere is new and exciting! Ground signatures are new and exciting!

673 TODO: The support software — the driver and the plotter — are also significant. Do  
674 they get mentioned here? Does the Git repository where the code can be accessed get  
675 mentioned here?

## 676 5.1 Coordinate System

Field line resonance has traditionally been modeled by straightening the field lines into a rectangular configuration[20, 66], by unrolling the azimuthal coordinate into a cylindrical coordinate system[78], or through the use of dipole coordinates[77]<sup>1</sup>:

$$x \equiv -\frac{\sin^2 \theta}{r} \quad y \equiv \phi \quad z \equiv \frac{\cos \theta}{r^2} \quad (5.1)$$

677 Where  $r$ ,  $\theta$ , and  $\phi$  take on their usual spherical meanings of radial distance, colatitude,  
678 and azimuthal angle respectively.

679 The dipole coordinate  $x$  is constant over each equipotential shell<sup>2</sup>,  $y$  is azimuthal angle,  
680 and  $z$  indexes each field line from south to north. The unit vectors  $\hat{x}$ ,  $\hat{y}$ , and  $\hat{z}$  point

---

<sup>1</sup>The dipole coordinates  $x$ ,  $y$  and  $z$  are perhaps more commonly named  $\mu$ ,  $\phi$ , and  $\nu$  respectively; however, in the present work,  $\mu$  and  $\nu$  take other meanings.

<sup>2</sup>In fact,  $x$  is inversely proportional to the McIlwain parameter  $L$ .

681 in the crosswise<sup>3</sup> (radially outward at the equator), azimuthal (eastward), and parallel  
 682 (northward at the equator) directions respectively.

Notably, the dipole coordinates in Equation (5.1) are normal to one another. While mathematically convenient, they do not readily accommodate a fixed-altitude boundary at the ionosphere, nor do they allow the dipole magnetic field to intersect the boundary at an oblique angle, as Earth's field does. As a solution, a nonorthogonal set of dipole coordinates was developed numerically by Proehl[76], then formalized analytically by Lysak[59] in terms of their contravariant components:

$$u^1 = -\frac{R_I}{r} \sin^2 \theta \quad u^2 = \phi \quad u^3 = \frac{R_I^2}{r^2} \frac{\cos \theta}{\cos \theta_0} \quad (5.2)$$

683 Above,  $R_I$  is the position of the ionosphere relative to Earth's center; it's typically taken  
 684 to be  $1 R_E + 100 \text{ km}$ .

685 Like the dipole coordinates  $x$ ,  $y$ , and  $z$ , Lysak's coordinates  $u^1$ ,  $u^2$ , and  $u^3$  correspond to  
 686  $L$ -shell, azimuthal angle, and position along a field line respectively. However, compared  
 687 to  $z$ ,  $u^3$  has been renormalized using the invariant colatitude<sup>4</sup>  $\theta_0$ . As a result,  $u^3$  takes  
 688 the value  $+1$  at the northern ionospheric boundary and  $-1$  at the southern ionospheric  
 689 boundary for all field lines.

Because Lysak's coordinate system is not orthogonal<sup>5</sup>, it's necessary to consider covariant and contravariant basis vectors separately.

$$\hat{e}_i \equiv \frac{\partial}{\partial u^i} \underline{x} \quad \hat{e}^i \equiv \frac{\partial}{\partial \underline{x}} u^i \quad (5.3)$$

Covariant basis vectors  $\hat{e}_i$  are normal to the curve defined by constant  $u^i$ , while contravariant basis vectors  $\hat{e}^i$  are tangent to the coordinate curve (equivalently,  $\hat{e}^i$  is normal

---

<sup>3</sup>In the context of in situ measurements taken near the equatorial plane,  $\hat{x}$  is referred to as the radial direction; however, the present work extends the dipole grid to low altitudes, where  $\hat{x}$  can be more horizontal than vertical. The term "crosswise" is meant to indicate that  $\hat{x}$  is defined by the cross product of  $\hat{y}$  and  $\hat{z}$ .

<sup>4</sup>The invariant colatitude is the colatitude  $\theta$  at which a field line intersects the ionosphere. It is related to the McIlwain parameter by  $\cos \theta_0 \equiv \sqrt{1 - \frac{R_I}{L}}$ .

<sup>5</sup>Curves of constant  $u^1$  and curves of constant  $u^3$  can intersect at non-right angles.

to the plane defined by constant  $u^j$  for all  $j \neq i$ ). These vectors are reciprocal<sup>6</sup> to one another, and can be combined to give components of the metric tensor  $\underline{\underline{g}}$ [19].

$$\hat{e}^i \cdot \hat{e}_j = \delta_j^i \quad g_{ij} \equiv \hat{e}_i \cdot \hat{e}_j \quad g^{ij} \equiv \hat{e}^i \cdot \hat{e}^j \quad (5.4)$$

The metric tensor allows rotation between covariant and contravariant representations of vectors.

$$A_i = g_{ij} A^j \quad \text{and} \quad A^i = g^{ij} A_j \quad \text{where} \quad A_i \equiv \underline{A} \cdot \hat{e}_i \quad \text{and} \quad A^i \equiv \underline{A} \cdot \hat{e}^i \quad (5.5)$$

In addition, the determinant of the metric tensor is used to define cross products and curls<sup>7</sup>.

$$(\underline{A} \times \underline{B})^i = \frac{\varepsilon^{ijk}}{\sqrt{g}} A_j B_k \quad \text{and} \quad (\nabla \times \underline{A})^i = \frac{\varepsilon^{ijk}}{\sqrt{g}} \frac{\partial}{\partial u^j} A_k \quad \text{where} \quad g \equiv \det \underline{\underline{g}} \quad (5.6)$$

Explicit forms of the basis vectors and metric tensor can be found in the appendix of Lysak's 2004 paper[59]. At present, it's sufficient to note the mapping between Lysak's basis vectors and the usual dipole unit vectors.

$$\hat{x} = \frac{1}{\sqrt{g^{11}}} \hat{e}^1 \quad \hat{y} = \frac{1}{\sqrt{g^{22}}} \hat{e}^2 \quad \hat{z} = \frac{1}{\sqrt{g^{33}}} \hat{e}^3 \quad (5.7)$$

690 TODO: Do these need to be written out? Referring people to the code, which will be  
691 in a public Git repository, is also a possibility.

The basis vectors can also be mapped to the spherical unit vectors, though Equation (5.8) is valid only at the ionospheric boundary.

$$\hat{\theta} = \frac{1}{\sqrt{g_{11}}} \hat{e}_1 \quad \hat{\phi} = \frac{1}{\sqrt{g_{22}}} \hat{e}_2 \quad \hat{r} = \frac{1}{\sqrt{g_{33}}} \hat{e}_3 \quad (5.8)$$

---

<sup>6</sup>The symbol  $\delta_j^i$  is the Kronecker delta; the present work also makes use of the Levi-Civita symbol  $\varepsilon^{ijk}$  and Einstein's convention of implied summation over repeated indeces[22].

<sup>7</sup>The square root of the determinant of the metric tensor is called the Jacobian. It's sometimes denoted using the letter  $J$ , which is reserved for current in the present work.

692 The coordinates converge at the equatorial ionosphere, so an inner boundary is necessary  
693 to maintain finite grid spacing. It's typically placed at  $L = 2$ . The outer boundary is  
694 at  $L = 10$ . The dipole approximation of Earth's magnetic field is tenuous at the outer  
695 boundary (particularly on the dayside); however, in practice, wave activity is localized  
696 inside  $L \sim 7$ . The grid is spaced uniformly in  $u^1$ , which gives finer resolution close to  
697 Earth and coarser resolution at large distances.

698 Spacing in  $u^3$  is set by placing grid points along the outermost field line. The points are  
699 closest together at the ionosphere, and grow towards the equator. The spacing increases  
700 in a geometric fashion, typically by 3%.

701 Typically, Tuna uses a grid 150 points in  $u^1$  by 350 points in  $u^3$ . The result is a resolution  
702 on the order of 10 km at the ionosphere, which increases to the order of 10<sup>3</sup> km at the  
703 midpoint of the outermost field line.

704 There are no grid points in  $u^2$  due to the two-and-a-half-dimensional nature of the  
705 model. Fields are assumed to vary as  $\exp(imu^2)$  — equally,  $\exp(im\phi)$  — so derivatives  
706 with respect to  $u^2$  are equivalent to a factor of  $im$ . In effect, the real component of  
707 each field is azimuthally in phase with the (purely real) driving, while imaginary values  
708 represent behavior that is azimuthally offset.

709 The simulation's time step is set based on the grid spacing. As is the convention,  $\delta t$  is  
710 set to match the smallest Alfvén zone crossing time, scaled down by a Courant factor  
711 (typically 0.1). It bears noting that the smallest crossing time need not correspond to  
712 the smallest zone; the Alfvén speed peaks several thousand kilometers above Earth's  
713 surface, in the so-called Ionospheric Alfvén Resonator[63]. A typical time step is on the  
714 order of 10<sup>-5</sup> s.

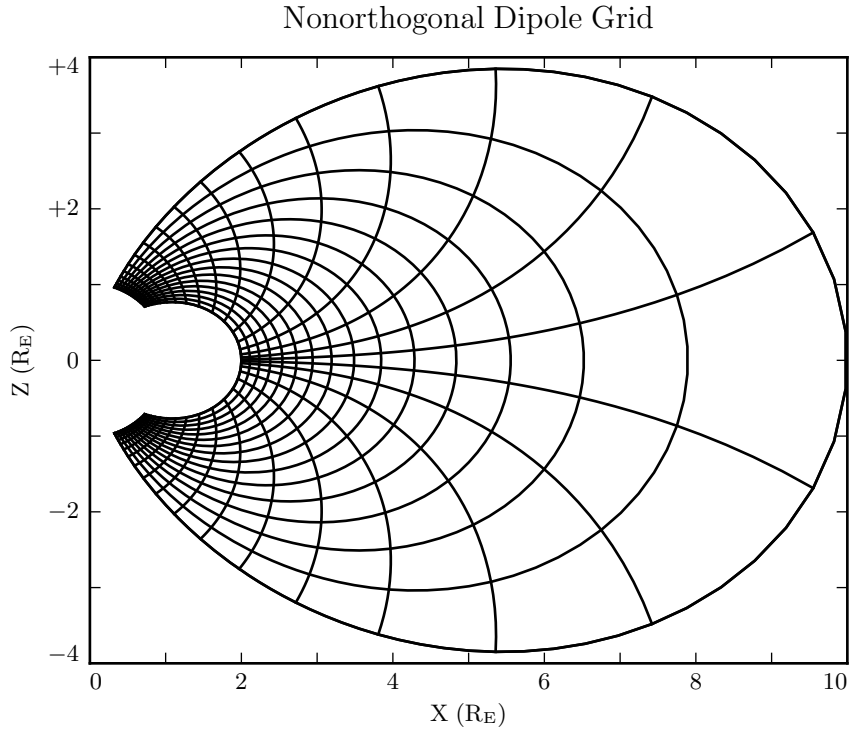


Figure 5.1: The model's nonorthogonal dipole grid. Every fifth point is shown in each direction. The high concentration of grid points near Earth's equator is a consequence of the coordinate system, which converges at the equatorial ionosphere. Earth (not shown) is centered at the origin with unit radius.

715 **5.2 Physical Parameter Profiles**

Tuna models Earth's magnetic field to be an ideal dipole, so the zeroth-order field strength is written in the usual form:

$$\underline{B}_0 = 3.1 \times 10^4 \text{ nT} \left( \frac{R_E}{r} \right)^3 \left( 2 \cos \theta \hat{r} - \sin \theta \hat{\theta} \right) \quad (5.9)$$

Number density is taken to be the sum of an inverse-radial-dependent auroral profile and a plasmaspheric profile dependent on the  $L$ -shell[63]:

$$n = n_{AZ} \frac{r_{AZ}}{r} + n_{PS} \exp\left(\frac{-L}{L_{PS}}\right) \left( \frac{1}{2} - \frac{1}{2} \tanh \frac{L - L_{PP}}{\delta L_{PP}} \right) \quad (5.10)$$

<sup>716</sup> Where typical values are shown in Table 5.1.

Table 5.1: Typical Parameters for the Tuna Density Profile

Variable	Value	Description
$L_{PS}$	1.1	Scale $L$ of the plasmasphere.
$L_{PP}$	4.0	Location of the plasmapause.
$\delta L_{PP}$	0.1	Thickness of the plasmapause.
$n_{AZ}$	$10 / \text{cm}^3$	Number density at the base of the auroral zone.
$n_{PS}$	$10^4 / \text{cm}^3$	Number density at the base of the plasmasphere.
$r_{AZ}$	$1 \text{ R}_E$	Scale height of the auroral density distribution.

The perpendicular component of the electric tensor,  $\epsilon_{\perp}$ , is computed based on Kelley's[48] tabulated low-density values,  $\epsilon_K$ , which are adjusted to take into account the effects of high density in the plasmapause.

$$\epsilon_{\perp} = \epsilon_K + \frac{Mn}{B_0^2} \quad (5.11)$$

<sup>717</sup> Where  $M$  is the mean molecular mass, which is large ( $\sim 28 \text{ u}$ ) at 100 km altitude, then  
<sup>718</sup> drops quickly (down to 1 u by  $\sim 1000 \text{ km}$ )[63].

<sup>719</sup> The Alfvén speed profile is computed from the perpendicular electric constant in the  
<sup>720</sup> usual way,  $v_A^2 \equiv \frac{1}{\mu_0 \epsilon_{\perp}}$ . This form takes into account the effect of the displacement  
<sup>721</sup> current, which becomes important in regions where the Alfvén speed approaches the  
<sup>722</sup> speed of light.

<sup>723</sup> While the density profile is held constant for all runs discussed in the present work,  
<sup>724</sup> the Alfvén speed profile is not. Four different profiles are used for the low-density

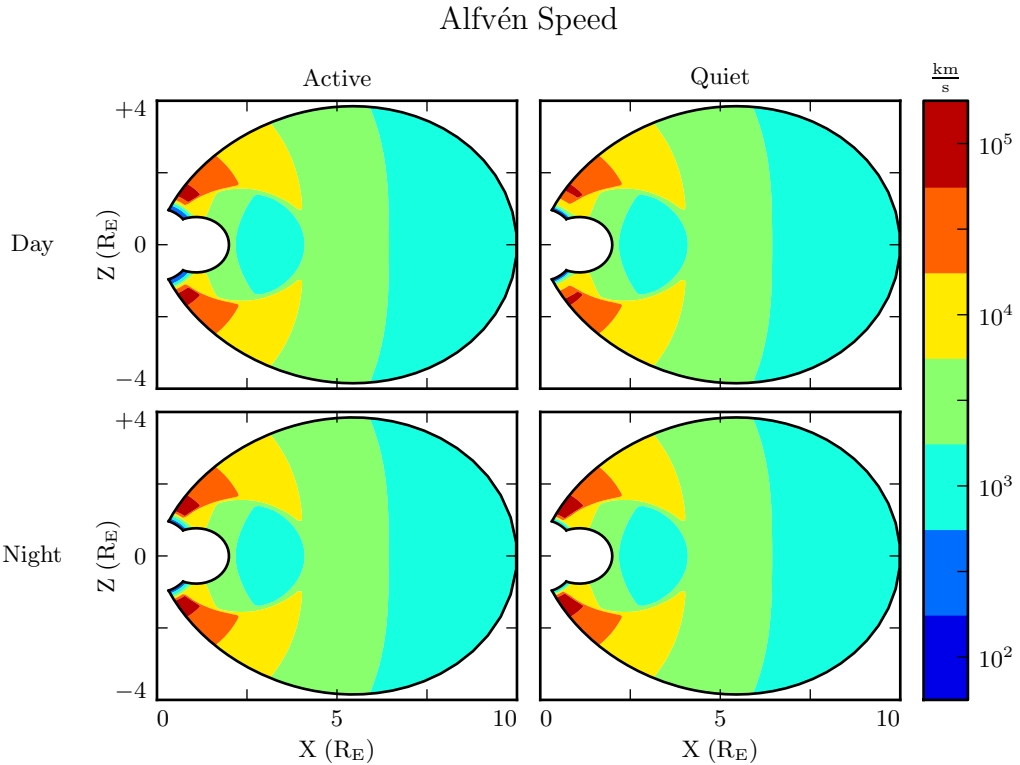


Figure 5.2: Alfvén speed profiles are based on low-density values tabulated by Kelley[48]. They are adjusted to take into account the density of the plasmapause and mass loading near the Earthward boundary.

725 perpendicular electric constant  $\epsilon_K$ , corresponding to the differing ionospheric conditions  
 726 between the dayside and the nightside, and between the high and low points in the  
 727 solar cycle. These differences are visible in Figure 5.2, particularly in the size of the  
 728 ionospheric Alfvén resonator (the peak in Alfvén speed in the high-latitude ionosphere).

729 **TODO:** Runs are only carried out for day and night... is it even worth showing the  
 730 flank profile?

731 Ionospheric conductivity profiles are also based on values tabulated by Kelley, adjusted  
 732 by Lysak[63] to take into account the abundance of heavy ions near the Earthward  
 733 boundary. Pedersen, Hall, and parallel conductivities are each resolved by altitude, as  
 734 shown in Figure 5.3.

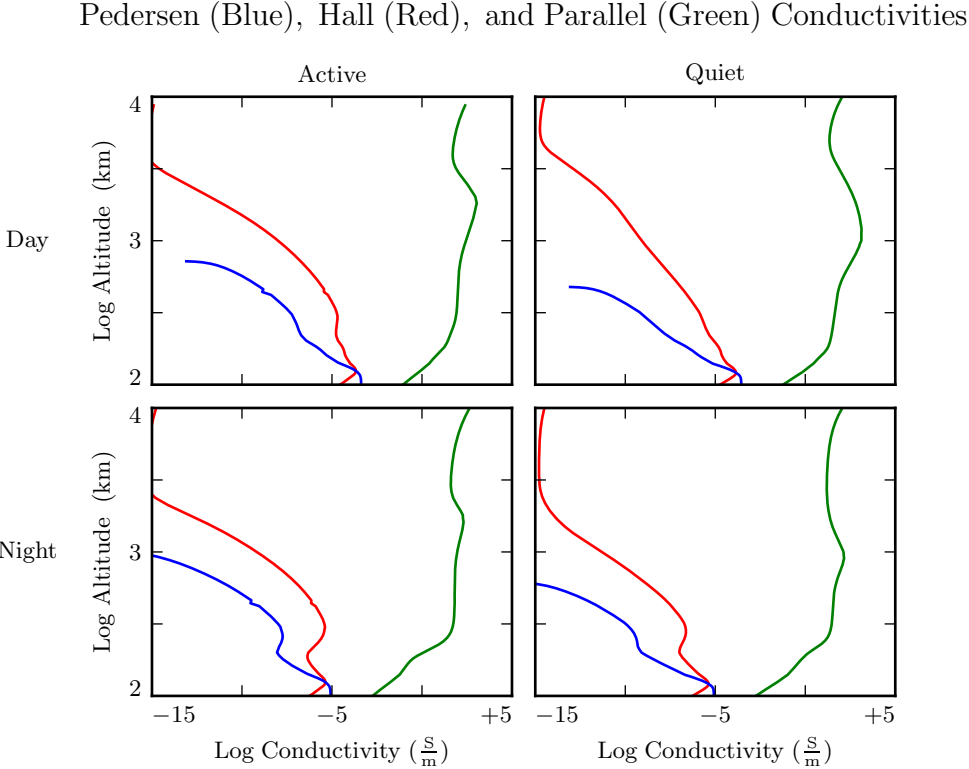


Figure 5.3: Ionospheric conductivity profiles are adapted by Lysak[63] from Kelley's tabulated values[48]. These profiles allow Tuna to simulate magnetosphere-ionosphere coupling under a variety of conditions.

735 Tuna's physical parameter profiles are static over the course of each run. Even so-called  
 736 ultra low frequency waves like Pc4 pulsations are fast compared to convective timescales  
 737 in the magnetosphere.

### 738 5.3 Driving

739 Models similar to Tuna have traditionally been driven using compression at the outer  
 740 boundary[59, 63, 99, 100]. Such driving acts as a proxy for solar wind compression,  
 741 Kelvin-Helmholtz effects at the magnetopause, and so on. However, because of the

742 constraints imposed by the dispersion relation for Alfvén waves<sup>8</sup>, simulations driven from  
743 the outer boundary are constrained to the consideration of waves with low azimuthal  
744 modenumber (equivalently, large azimuthal wavelength).

745 This issue is demonstrated in Figure 5.4. At low modenumber, energy delivered at  
746 the outer boundary propagates across field lines in order to stimulate resonances in  
747 the inner magnetosphere. However, as modenumber increases, Alfvén waves become  
748 increasingly guided, and the inner magnetosphere is unaffected by perturbations at the  
749 outer boundary.

750 In order to simulate high-modenumber Alfvén waves in the inner magnetosphere — such  
751 as giant pulsations — a new driving mechanism is necessary. Perturbation of the ring  
752 current is a natural choice, as Alfvén waves in the Pc4 range are known to interact with  
753 ring current particles through drift and drift-bounce resonances. The ring current is a  
754 dynamic region, particularly during and after geomagnetic storms; it's easy to imagine  
755 the formation of localized inhomogeneities.

756 In order to estimate an appropriate magnitude for perturbations of the ring current,  
757 the Sym-H storm index is used. The index is measured once per minute, and so cannot  
758 directly detect ring current modulations in the Pc4 frequency range. Instead, the index  
759 is transformed into the frequency domain, allowing a fit of its pink noise<sup>9</sup>.

760 **TODO:** Sym-H is basically the same as DST [98].

761 As shown in Figure 5.5, a Fourier transform of the Sym-H index (taken here from the  
762 June 2013 storm) suggests that magnetic field perturbations at Earth's surface due to  
763 ring current activity in the Pc4 frequency range could be up to the order of  $10^{-2}$  nT.  
764 Supposing that the ring current is centered around  $5 R_E$  geocentric, that corresponds to  
765 a current on the order of 0.1 MA. Tuna's driving is spread using a Gaussian profile in  
766  $u^1$  (typically centered at  $L = 5$ ) and  $u^3$  (typically centered just off the equator), with a  
767 characteristic area of  $1 R_E^2$ ; this gives a current density on the order of  $10^{-4} \mu\text{A}/\text{m}^2$ .

---

<sup>8</sup>See Section 4.4.

<sup>9</sup>Pink noise, also called  $\frac{1}{f}$  noise, refers to the power law decay present in the Fourier transforms of all manner of physical signals.

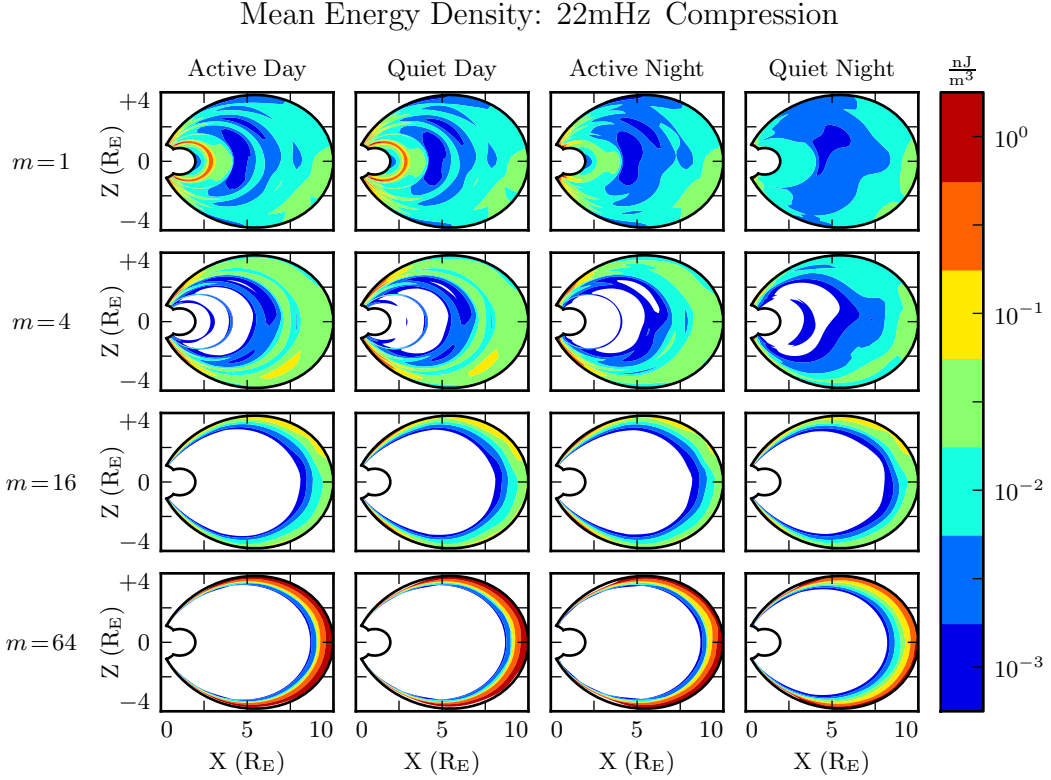


Figure 5.4: Each cell presents the mean energy density over the course of a 300 s run, as a function of position, due to compressional driving at the outer boundary. Azimuthal modenumber varies by row, and ionospheric conditions vary by column. For runs with small azimuthal modenumber, it's clear that energy is able to propagate across field lines and stimulate wave activity in the inner magnetosphere. When the modenumber is large, energy is unable to penetrate to the inner magnetosphere. Notably, the large values on the bottom row should be taken with a grain of salt; it's not clear that the model's results are reliable when waves are continuously forced against the boundary.

- 768 TODO: Admittedly, estimating the strength of localized perturbations using Sym-H —  
 769 an index averaged over the entire globe — is a bit of a kludge.
- 770 In situ observations of Pc4 pulsations and giant pulsations have shown waves with  
 771 modenumbers across the range  $1 \lesssim m \lesssim 100$ [16, 17, 90]. Simulations are carried out  
 772 across that range, corresponding to ring current perturbations with azimuthal extent as  
 773 small as  $0.5 R_E$ .

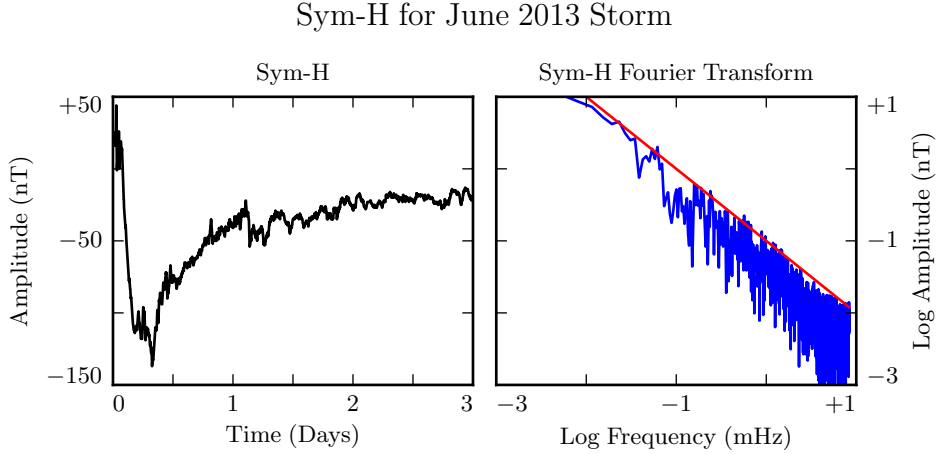


Figure 5.5: The Sym-H storm index[71] measures magnetic perturbations on Earth’s surface due to ring current activity. The amplitude of oscillations in the Pc4 range is estimated by fitting the pink noise in its Fourier transform.

774 TODO: Driving is delivered in the azimuthal component of the current only.

775 TODO: Driving is sinusoidal.

776 TODO: In case it’s not clear: Chapter 7 discusses ONLY simulations using ring current driving.  
777 The only compressional driving we look at is Figure 5.4.

## 778 5.4 Maxwell’s Equations

779 Tuna simulates the evolution of electromagnetic waves in accordance with Ampère’s  
780 law and Faraday’s law. Computation is carried out on a Yee grid[104]: electric fields  
781 and magnetic fields are offset by half a time step, and each field component is defined  
782 on either odd or even grid points in each dimension to ensure that curls are computed  
783 using centered differences.

The Ohmic current in Ampère’s law is replaced with  $\underline{\sigma} \cdot \underline{E}$  per Kirchhoff’s formulation of Ohm’s law. Then, taking  $\underline{J}$  to represent the driving current discussed in Section 5.3,

Maxwell's equations can be written

$$\frac{\partial}{\partial t} \underline{B} = -\nabla \times \underline{E} \quad \underline{\epsilon} \cdot \frac{\partial}{\partial t} \underline{E} = \frac{1}{\mu_0} \nabla \times \underline{B} - \underline{J} - \underline{\sigma} \cdot \underline{E} \quad (5.12)$$

It is convenient to introduce shorthand for the curl of each field:  $\underline{C} \equiv \nabla \times \underline{E}$  and  $\underline{F} \equiv \nabla \times \underline{B} - \mu_0 \underline{J}$ . Or, recalling Equation (5.6),

$$C^i = \frac{\varepsilon^{ijk}}{\sqrt{g}} \frac{\partial}{\partial u^j} E_k \quad F^i = \frac{\varepsilon^{ijk}}{\sqrt{g}} \frac{\partial}{\partial u^j} B_k - J^i \quad (5.13)$$

In these terms, Faraday's law can simply be written:

$$\frac{\partial}{\partial t} B^i = -C^i \quad (5.14)$$

Writing each component out explicitly, and using the metric tensor (per Equation (5.5)) to eliminate contravariant magnetic field components<sup>10</sup>, Equation (5.14) becomes:

$$\begin{aligned} B_1 &\leftarrow B_1 - g_{11} \delta t C^1 - g_{13} \delta t C^3 \\ B_2 &\leftarrow B_2 - g_{22} \delta t C^2 \\ B_3 &\leftarrow B_3 - g_{31} \delta t C^1 - g_{33} \delta t C^3 \end{aligned} \quad (5.15)$$

<sup>784</sup> Note that the  $\leftarrow$  operator is used in Equation (5.15) to indicate assignment, rather than equality. Terms on the left are new, while those on the right are old.

Unlike Faraday's law, Ampère's law cannot be trivially solved. Not only does the derivative of  $\underline{E}$  depend on its own future value, but the crosswise and azimuthal components of the equation are coupled by the Hall terms in the conductivity tensor. Fortunately,

---

<sup>10</sup>Fields are stored only in terms of their covariant components, and curls in terms of their contravariant components. This reduces Tuna's memory footprint (since each field need not be stored twice) as well as its computational cost (since time need not be spent rotating between bases). As a result, Tuna's solutions to Maxwell's equations are linear expressions whose coefficients are a mishmash of physical constants and geometric factors. To save time, each coefficient is computed once and stored, rather than being multiplied out from scratch with each time step.

the electric tensor can be inverted, allowing a solution by integrating factors:

$$\underline{\epsilon} \cdot \frac{\partial}{\partial t} \underline{E} = \frac{1}{\mu_0} \underline{F} - \underline{\sigma} \cdot \underline{E} \quad \text{becomes} \quad \left( \underline{\Omega} + \underline{\mathbb{I}} \frac{\partial}{\partial t} \right) \cdot \underline{E} = \underline{V}^2 \cdot \underline{F} \quad (5.16)$$

Where  $\underline{\mathbb{I}}$  is the identity tensor and in  $x$ - $y$ - $z$  coordinates<sup>11</sup>,

$$\underline{V}^2 \equiv \frac{1}{\mu_0} \underline{\epsilon}^{-1} = \begin{bmatrix} v_A^2 & 0 & 0 \\ 0 & v_A^2 & 0 \\ 0 & 0 & c^2 \end{bmatrix} \quad \text{and} \quad \underline{\Omega} \equiv \underline{\epsilon}^{-1} \cdot \underline{\sigma} = \begin{bmatrix} \frac{\sigma_P}{\epsilon_{\perp}} & \frac{-\sigma_H}{\epsilon_{\perp}} & 0 \\ \frac{\sigma_H}{\epsilon_{\perp}} & \frac{\sigma_P}{\epsilon_{\perp}} & 0 \\ 0 & 0 & \frac{\sigma_0}{\epsilon_0} \end{bmatrix} \quad (5.17)$$

Multiplying through by  $\exp(\underline{\Omega} t)$  and applying the product rule, Equation (5.16) becomes<sup>12</sup>

$$\frac{\partial}{\partial t} \left( \exp(\underline{\Omega} t) \cdot \underline{E} \right) = \exp(\underline{\Omega} t) \cdot \underline{V}^2 \cdot \underline{F} \quad (5.18)$$

Equation (5.18) can then be integrated over a small time step  $\delta t$  and expressed in terms of the assignment operator introduced in Equation (5.15).

$$\underline{E} \leftarrow \exp(-\underline{\Omega} \delta t) \cdot \underline{E} + \delta t \exp(-\underline{\Omega} \frac{\delta t}{2}) \cdot \underline{V}^2 \cdot \underline{F} \quad (5.19)$$

The tensor exponential can be evaluated by splitting  $\underline{\Omega}$  into the sum of its diagonal and Hall components<sup>13</sup>. The Hall exponential condenses into sines and cosines, giving a rotation around the magnetic field line:

$$\underline{E} \leftarrow \exp(-\underline{\Omega}' \delta t) \cdot \underline{R}_z \left( \frac{-\sigma_H \delta t}{\epsilon_{\perp}} \right) \cdot \underline{E} + \delta t \underline{V}^2 \cdot \exp(-\underline{\Omega}' \frac{\delta t}{2}) \cdot \underline{R}_z \left( \frac{-\sigma_H \delta t}{2\epsilon_{\perp}} \right) \cdot \underline{F} \quad (5.20)$$

---

<sup>11</sup>Note the parallel component of the present definition of  $\underline{\Omega}$  differs slightly from that used in Chapter 4, due to the present neglect of inertial effects; see Chapter 6.

<sup>12</sup>Tensor exponentiation is analogous to scalar exponentiation[37]:  $\exp(\underline{T}) \equiv \sum_n \frac{1}{n!} \underline{T}^n$ .

<sup>13</sup>For tensors,  $\exp(\underline{S} + \underline{T}) = \exp(\underline{S}) \exp(\underline{T})$  as long as  $\underline{S} \cdot \underline{T} = \underline{T} \cdot \underline{S}$ .

Where

$$\underline{\underline{R}}_z(\theta) = \begin{bmatrix} \cos \theta & -\sin \theta & 0 \\ \sin \theta & \cos \theta & 0 \\ 0 & 0 & 1 \end{bmatrix} \quad \text{and} \quad \underline{\underline{\Omega}}' \equiv \begin{bmatrix} \frac{\sigma_P}{\epsilon_{\perp}} & 0 & 0 \\ 0 & \frac{\sigma_P}{\epsilon_{\perp}} & 0 \\ 0 & 0 & \frac{\sigma_0}{\epsilon_0} \end{bmatrix} \quad (5.21)$$

The parallel component of term of Equation (5.20) is simply

$$E_z \leftarrow E_z \exp\left(\frac{-\sigma_0 \delta t}{\epsilon_0}\right) + c^2 \delta t F_z \exp\left(\frac{-\sigma_0 \delta t}{2\epsilon_0}\right) \quad (5.22)$$

Or, using Equation (5.7) to map to the covariant basis,

$$E_3 \leftarrow E_3 \exp\left(\frac{-\sigma_0 \delta t}{\epsilon_0}\right) + c^2 \delta t (g_{31} F^1 + g_{33} F^3) \exp\left(\frac{-\sigma_0 \delta t}{2\epsilon_0}\right) \quad (5.23)$$

786 Tuna's conductivity profile gives a minimum value of  $\frac{\sigma_0 \delta t}{\epsilon_0}$  on the order of  $10^3$ , making  
 787  $\exp\left(\frac{-\sigma_0 \delta t}{\epsilon_0}\right)$  far too small to be stored in a double precision variable<sup>14</sup>. That is, this  
 788 model takes  $E_3$  (and, proportionally,  $E_z$ ) to be uniformly zero. This issue is revisited  
 789 in Chapter 6.

The perpendicular components of Equation (5.20) give the expressions:

$$\begin{aligned} E_1 + \frac{g^{13}}{g^{11}} E_3 &\leftarrow E_1 \cos\left(\frac{-\sigma_H \delta t}{\epsilon_{\perp}}\right) \exp\left(\frac{-\sigma_P \delta t}{\epsilon_{\perp}}\right) \\ &\quad + E_2 \sin\left(\frac{-\sigma_H \delta t}{\epsilon_{\perp}}\right) \exp\left(\frac{-\sigma_P \delta t}{\epsilon_{\perp}}\right) \sqrt{\frac{g^{22}}{g^{11}}} \\ &\quad + E_3 \cos\left(\frac{-\sigma_H \delta t}{\epsilon_{\perp}}\right) \exp\left(\frac{-\sigma_P \delta t}{\epsilon_{\perp}}\right) \frac{g^{13}}{g^{11}} \\ &\quad + F^1 \cos\left(\frac{-\sigma_H \delta t}{2\epsilon_{\perp}}\right) \exp\left(\frac{-\sigma_P \delta t}{2\epsilon_{\perp}}\right) \frac{v_A^2 \delta t}{g^{11}} \\ &\quad + F^2 \sin\left(\frac{-\sigma_H \delta t}{2\epsilon_{\perp}}\right) \exp\left(\frac{-\sigma_P \delta t}{2\epsilon_{\perp}}\right) \frac{v_A^2 \delta t}{\sqrt{g^{11} g^{22}}} \end{aligned} \quad (5.24)$$

---

<sup>14</sup>Not coincidentally,  $\frac{\sigma_0}{\epsilon_0}$  can also be written  $\frac{\omega_P^2}{\nu}$ . At the ionosphere, the collision frequency  $\nu$  is fast compared to field line resonance timescales, but it's still slow compared to the plasma frequency.

and

$$\begin{aligned}
E_2 \leftarrow & -E_1 \sin\left(\frac{-\sigma_H \delta t}{\epsilon_{\perp}}\right) \exp\left(\frac{-\sigma_P \delta t}{\epsilon_{\perp}}\right) \sqrt{\frac{g^{11}}{g^{22}}} \\
& + E_2 \cos\left(\frac{-\sigma_H \delta t}{\epsilon_{\perp}}\right) \exp\left(\frac{-\sigma_P \delta t}{\epsilon_{\perp}}\right) \\
& - E_3 \sin\left(\frac{-\sigma_H \delta t}{\epsilon_{\perp}}\right) \exp\left(\frac{-\sigma_P \delta t}{\epsilon_{\perp}}\right) \frac{g^{13}}{\sqrt{g^{11} g^{22}}} \\
& - F^1 \sin\left(\frac{-\sigma_H \delta t}{2\epsilon_{\perp}}\right) \exp\left(\frac{-\sigma_P \delta t}{2\epsilon_{\perp}}\right) \frac{v_A^2 \delta t}{\sqrt{g^{11} g^{22}}} \\
& + F^2 \cos\left(\frac{-\sigma_H \delta t}{2\epsilon_{\perp}}\right) \exp\left(\frac{-\sigma_P \delta t}{2\epsilon_{\perp}}\right) \frac{v_A^2 \delta t}{g^{22}}
\end{aligned} \tag{5.25}$$

790 The  $E_3$  terms in Equations (5.24) and (5.25) can be ignored at present. They are  
791 revisited in Chapter 6.

792 It bears recalling that the driving current is defined as part of  $\underline{F}$ , per Equation (5.13).  
793 When the driving current is purely azimuthal ( $J^1 = J^3 = 0$ ), the driving is in principle  
794 applied to both the poloidal and the toroidal electric fields through  $F^2$ . However,  
795 in practice, the driving applied to the toroidal electric field is vanishingly small. The  
796 driving current  $J^2$  is localized around  $5 R_E$  geocentric, and  $\exp\left(\frac{-\sigma_P \delta t}{2\epsilon_{\perp}}\right)$  drops off quickly  
797 with altitude.

## 798 5.5 Boundary Conditions

799 Dirichlet and Neumann boundary conditions are applied to the electric field components  
800 and magnetic field components respectively. That is, electric fields are forced to go to  
801 zero at the inner and outer boundaries, and magnetic fields are forced to have a zero  
802 derivative normal to the inner and outer boundaries.

803 These boundary conditions can in principle cause nonphysical reflections at the bound-  
804 ary<sup>15</sup>. However, in practice, wave activity is concentrated well within the simulation  
805 domain. Simulation results are robust under an exchange of Dirichlet and Neumann

---

<sup>15</sup>See, for example, the bottom row of Figure 5.4.

806 boundary conditions (though a self-inconsistent set of boundary condidtions, such as  
 807 applying Neumann boundary conditions to  $B_1$  but Dirichlet boundary conditions to  $B_3$ ,  
 808 quickly causes instability).

809 The Earthward boundary conditions are as follows.

Between the top of the neutral atmosphere and the bottom of the ionosphere, the model includes a thin, horizontal current sheet representing the ionosphere's  $E$  layer[59]. By integrating Ampère's law over the layer, it can be shown[27] that the horizontal electric field values at the edge of the grid are determined by the jump in the horizontal magnetic fields:

$$\underline{\underline{\Sigma}} \cdot \underline{E} = \frac{1}{\mu_0} \lim_{\delta r \rightarrow 0} \left[ \hat{r} \times \underline{B} \right]_{R_I - \delta r}^{R_I + \delta r} \quad (5.26)$$

The integrated conductivity tensor  $\underline{\underline{\Sigma}}$  can be written in  $\theta$ - $\phi$  coordinates as[59]:

$$\underline{\underline{\Sigma}} \equiv \begin{bmatrix} \frac{\Sigma_0 \Sigma_P}{\Sigma_0 \cos^2 \alpha + \Sigma_P \sin^2 \alpha} & \frac{-\Sigma_0 \Sigma_H}{\Sigma_0 \cos^2 \alpha + \Sigma_P \sin^2 \alpha} \\ \frac{\Sigma_0 \Sigma_H}{\Sigma_0 \cos^2 \alpha + \Sigma_P \sin^2 \alpha} & \Sigma_P + \frac{\Sigma_H^2 \sin^2 \alpha}{\Sigma_0 \cos^2 \alpha + \Sigma_P \sin^2 \alpha} \end{bmatrix} \quad (5.27)$$

810 Where  $\alpha$  is the angle between the magnetic field and the vertical direction, given by  
 811  $\cos \alpha \equiv \frac{-2 \cos \theta}{\sqrt{1+3 \cos^2 \theta}}$ , and  $\Sigma_P$ ,  $\Sigma_H$ , and  $\Sigma_0$  are the height-integrated Pedersen, Hall,  
 812 and parallel conductivities respectively. Their values are determined by integrating  
 813 Kelley's[48] conductivity profiles from Earth's surface to the ionospheric boundary; val-  
 814 ues are shown in Table 5.2.

Table 5.2: Integrated Atmospheric Conductivity (S)

	$\Sigma_0$	$\Sigma_P$	$\Sigma_H$
Active Day	424	0.65	6.03
Quiet Day	284	0.44	4.02
Active Night	9	0.01	0.12
Quiet Night	9	0.01	0.12

An expression for the horizontal electric fields at the boundary can be obtained by inverting Equation (5.26). After mapping to covariant coordinates per Equation (5.8), and taking  $\Sigma \equiv \det \underline{\underline{\Sigma}}$ ,

$$\begin{aligned} E_1 &\leftarrow \frac{1}{\mu_0 \Sigma} \lim_{\delta r \rightarrow 0} \left[ -\Sigma_{\theta\phi} B_1 - \sqrt{\frac{g_{11}}{g_{22}}} \Sigma_{\phi\phi} B_2 \right]_{R_I-\delta r}^{R_I+\delta r} \\ E_2 &\leftarrow \frac{1}{\mu_0 \Sigma} \lim_{\delta r \rightarrow 0} \left[ \sqrt{\frac{g_{22}}{g_{11}}} \Sigma_{\theta\theta} B_1 + \Sigma_{\phi\theta} B_2 \right]_{R_I-\delta r}^{R_I+\delta r} \end{aligned} \quad (5.28)$$

815 In order to compute the atmospheric magnetic field, a scalar magnetic potential ( $\Psi$   
816 such that  $\underline{B} = \nabla\Psi$ ) is computed as a linear combination of harmonics. The neutral  
817 atmosphere is considered to be a perfect insulator, giving  $\nabla \times \underline{B} = 0$ . Combined with  
818  $\nabla \cdot \underline{B} = 0$  (per Maxwell's equations),  $\Psi$  satisfies Laplace's equation,  $\nabla^2\Psi = 0$ .

Laplace's equation can be solved analytically; however, a numerical solution is preferable to ensure orthonormality on a discrete and incomplete<sup>16</sup> grid. After separating out the radial and azimuthal dependence in the usual way, the latitudinal component of Laplace's equation can be written in terms of  $s \equiv -\sin^2\theta$ :

$$(4s^2 + 4s) \frac{d^2}{ds^2} Y_\ell + (4 + 6s) \frac{d}{ds} Y_\ell - \frac{m^2}{s} Y_\ell = \ell(\ell+1) Y_\ell \quad (5.29)$$

Using centered differences to linearize the derivatives, Equation (5.29) becomes a system of coupled linear equations, one per field line. It can be solved numerically for eigenvalues  $\ell(\ell+1)$  and eigenfunctions  $Y_\ell$ <sup>17</sup>. In terms of the harmonics  $Y_\ell$ ,  $\Psi$  between the Earth's surface and the top of the atmosphere can be written using eigenweights  $a_\ell$  and  $b_\ell$ :

$$\Psi = \sum_\ell \left( a_\ell r^\ell + b_\ell r^{-\ell-1} \right) Y_\ell \quad (5.30)$$

---

<sup>16</sup>As discussed in Section 5.1, the grid is constrained to finite  $L$ , which excludes the equator as well as the poles.

<sup>17</sup>Solving Laplace's equation analytically results in spherical harmonics indexed by both  $\ell$  and  $m$ , the separation constants for  $\theta$  and  $\phi$  respectively. In two and a half dimensions,  $\phi$  is not explicitly resolved, so  $m$  is set manually.

As a boundary condition for  $\Psi$ , Earth is assumed to be a perfect conductor. This forces the magnetic field at Earth's surface to be horizontal; that is,  $B_r = \frac{\partial}{\partial r}\Psi = 0$ . Noting that solutions to Laplace's equation are orthonormal, each element of the sum in Equation (5.30) must be independently zero at  $R_E$ . This allows the coefficients  $a_\ell$  and  $b_\ell$  to be expressed in terms of one another.

$$b_\ell = \frac{\ell}{\ell + 1} R_E^{2\ell+1} a_\ell \quad (5.31)$$

The current sheet at the top of the atmosphere is assumed to be horizontal, so the radial component of the magnetic field must be the same just above and just below it. Taking the radial derivative of Equation (5.30) at the top of the atmosphere, and eliminating  $b_\ell$  with Equation (5.31), gives

$$B_r = \sum_\ell \ell a_\ell R_I^{\ell-1} \left(1 - \lambda^{2\ell+1}\right) Y_\ell \quad \text{where} \quad \lambda \equiv \frac{R_E}{R_I} \sim 0.975 \quad (5.32)$$

The summation can be collapsed by “integrating” over a harmonic<sup>18</sup>. Inverse harmonics can be obtained by inverting the eigenvector matrix. Then  $Y_\ell \cdot Y_{\ell'}^{-1} = \delta_{\ell\ell'}$  by construction.

$$a_\ell = \frac{1}{\ell R_I^{\ell-1}} \frac{B_r \cdot Y_\ell^{-1}}{1 - \lambda^{2\ell+1}} \quad (5.33)$$

Combining Equations (5.30), (5.31), and (5.33) allows the expression of  $\Psi$  at the top and bottom of the atmosphere as a linear combination of radial magnetic field components at the bottom of the ionosphere.

$$\begin{aligned} \Psi_E &= \sum_\ell Y_\ell \frac{R_I}{\ell (\ell - 1)} \frac{(2\ell - 1) \lambda^\ell}{1 - \lambda^{2\ell+1}} B_r \cdot Y_\ell^{-1} \\ \Psi_I &= \sum_\ell Y_\ell \frac{R_I}{\ell (\ell - 1)} \frac{(\ell - 1) + \ell \lambda^{2\ell+1}}{1 - \lambda^{2\ell+1}} B_r \cdot Y_\ell^{-1} \end{aligned} \quad (5.34)$$

---

<sup>18</sup>Because the functions are defined on a discrete grid, their inner product is not an integral, but a sum:  $B_r \cdot Y_\ell^{-1} \equiv \sum_i B_r[i] Y_\ell^{-1}[i]$ .

Horizontal magnetic fields are obtained by taking derivatives of  $\Psi$ .

$$B_1 = \frac{\partial}{\partial u^1} \Psi \quad B_2 = \frac{\partial}{\partial u^2} \Psi \quad (5.35)$$

- 819 Horizontal magnetic field values at the top of the atmosphere are used to impose bound-  
820 ary conditions on the electric fields at the bottom of the ionosphere, per Equation (5.28).  
821 Those at Earth's surface are valuable because they allow a direct comparison between  
822 model output and ground magnetometer data, after being mapped to physical coordi-  
823 nates per Equation (5.8).

824 **Chapter 6**

825 **Electron Inertial Effects**

826 As laid out in Chapter 5, Tuna resolves neither parallel currents nor parallel electric  
827 fields. This is unfortunate; parallel electric fields generated by kinetic and inertial Alfvén  
828 waves (including fundamental field line resonances[79, 95]) are a topic of particular  
829 interest in the study of auroral particle precipitation.

Parallel currents and electric fields can be added to Tuna through the consideration of electron inertial effects in Ohm's law:

$$0 = \sigma_0 E_z - J_z \quad \text{becomes} \quad \frac{1}{\nu} \frac{\partial}{\partial t} J_z = \sigma_0 E_z - J_z \quad (6.1)$$

With the addition of the electron inertial term, it is necessary to track the parallel current independent of the parallel electric field<sup>1</sup>. Solving by integrating factors<sup>2</sup> gives

$$J_3 \leftarrow J_3 \exp(-\nu \delta t) + \delta t \frac{ne^2}{m_e} E_3 \exp\left(-\nu \frac{\delta t}{2}\right) \quad (6.2)$$

---

<sup>1</sup>The parallel current  $J_z$  is defined on the same points of the Yee grid as  $E_z$ . It is offset in time by half of a time step.

<sup>2</sup>The integrating factors technique is laid out explicitly for Ampère's law in Section 5.4.

From there, the parallel electric field can be updated directly; Equation (5.23) is replaced by the following:

$$E_3 \leftarrow E_3 + c^2 \delta t (g_{31} F^1 + g_{33} F^3) - \frac{\delta t}{\epsilon_0} J_3 \quad (6.3)$$

830 The present section explores the complications that arise from the addition of the elec-  
 831 tron inertial term to Ohm's law, as well as a few results that may be gleaned despite  
 832 those complications. Notably — for reasons discussed in Section 6.3 — the results  
 833 presented in Chapter 7 do not make use of the electron inertial term.

834 Inertial effects have been considered in previous numerical work, such as by Lysak and  
 835 Song in 2001[61], but never at the global scale. Lysak and Song considered waves in  
 836 the ionospheric Alfvén resonator, with frequencies of hundreds of mHz. Their work did  
 837 not account for the effects of the dipolar geometry, such as differences that might arise  
 838 between poloidal and toroidal resonances. In fact, in that work, circular polarization  
 839 (essentially a superposition of poloidal and toroidal modes) was noted to be a promising  
 840 avenue for future work.

## 841 6.1 The Boris Factor

With the addition of the electron inertial term, a cyclical dependence appears between Ampère's law and Ohm's law:

$$\frac{\partial}{\partial t} E_z \sim -\frac{1}{\epsilon_0} J_z \quad \text{and} \quad \frac{\partial}{\partial t} J_z \sim \frac{n e^2}{m_e} E_z \quad \text{so} \quad \frac{\partial^2}{\partial t^2} E_z \sim -\omega_P^2 E_z \quad (6.4)$$

842 That is, electron inertial effects come hand in hand with the plasma oscillation.  
 843 As mentioned in Chapter 4 and shown in Figure 6.1, plasma oscillation is quite fast —  
 844 several orders of magnitude smaller than Tuna's time step as determined in Section 5.1  
 845 ( $\sim 10 \mu\text{s}$ ). This poses a conundrum. At Tuna's usual time step, the plasma oscillation  
 846 becomes unstable within seconds<sup>3</sup>. On the other hand, reducing the time step by three

---

<sup>3</sup>For stability,  $\omega_P \delta t < 1$  is necessary.

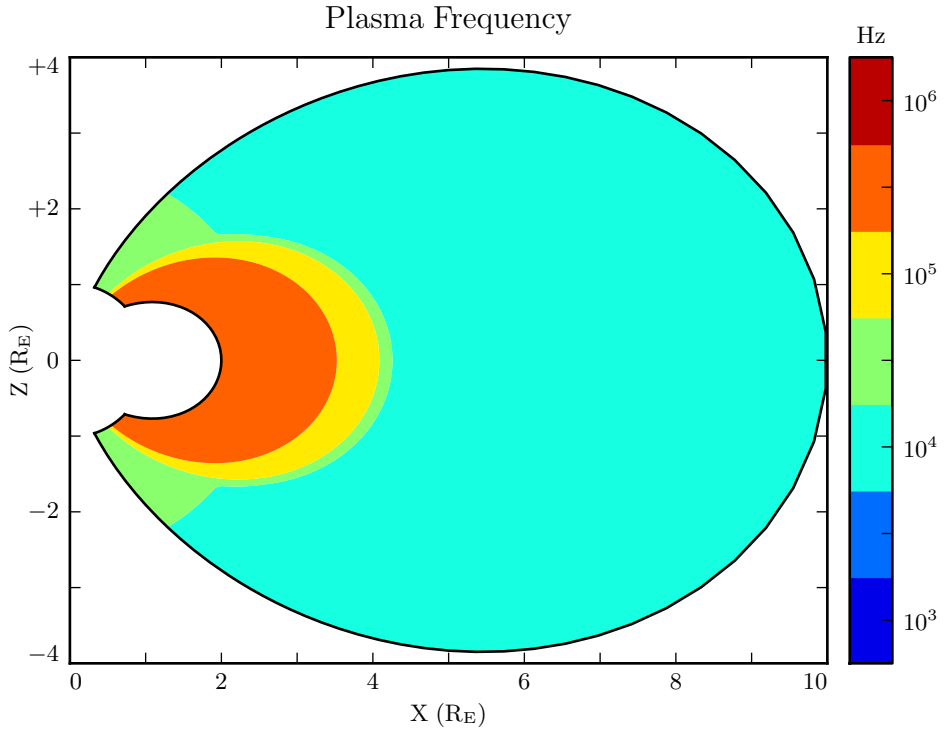


Figure 6.1: The plasma frequency reaches a peak value just under  $10^6$  Hz near the equator. Outside the plasmasphere, its value is closer to  $10^4$  Hz, which is still not well-resolved by Tuna's usual time step.

orders of magnitude to resolve the plasma oscillation is computationally infeasible; a run slated for an hour would require six weeks to complete.

As it happens, this problem can be solved by artificially increasing the parallel electric constant above its usual value of  $\epsilon_0$ . Doing so lowers both the speed of light and the plasma frequency within the simulation.

This technique — and others like it — has been widespread in numerical modeling since it was presented by Boris in 1970[6]. The following paraphrases an argument by Lysak and Song[61], outlining its validity specifically in the case of electron inertial effects.

Supposing that the current and electric field are oscillating at frequency  $\omega$ , the parallel components of Ampère's law and Ohm's law can be written

$$-i\omega\epsilon_0 E_z = \frac{1}{\mu_0} (\nabla \times \underline{B})_z - J_z \quad -\frac{i\omega}{\nu} J_z = \sigma_0 E_z - J_z \quad (6.5)$$

Then, eliminating the current, the parallel electric field can be related to the curl of the magnetic field by<sup>4</sup>

$$\left(1 - \frac{\omega^2 - i\nu\omega}{\omega_P^2}\right) E_z = \frac{c^2}{\omega_P^2} (\nu - i\omega) (\nabla \times \underline{B})_z \quad (6.6)$$

- 855 In Equation (6.6),  $\frac{c}{\omega_P}$  is the electron inertial length. While the speed of light and the  
 856 plasma frequency each depend on  $\epsilon_0$ , their ratio does not. This allows an estimation of  
 857 how much the model should be affected by an artificially-large electric constant (and  
 858 thus an artificially-small plasma frequency). So long as  $\frac{\omega^2 - i\nu\omega}{\omega_P^2}$  remains small compared  
 859 to unity, the model should behave faithfully.
- 860 For waves with periods of a minute or so, even perhaps-implausibly large Boris factors  
 861 are allowed; for example, increasing  $\epsilon_0$  by a factor of  $10^6$  gives  $\left|\frac{\omega^2 + i\omega\nu}{\omega_P^2}\right| \lesssim 0.01$ .

## 862 6.2 Parallel Currents and Electric Fields

- 863 As discussed in Section 4.4, parallel electric fields in this regime are expected to be six  
 864 or more orders of magnitude smaller than the perpendicular electric fields. Numerical  
 865 results show general agreement: in Figure 6.2, the parallel electric field appears com-  
 866 parable to its perpendicular counterparts only after its been scaled up by six orders of  
 867 magnitude.
- 868 As such, the inclusion of electron inertial effects does not appreciably impact the simu-  
 869 lation's gross behavior; in Faraday's law,  $\nabla \times \underline{E}$  is essentially unaffected. Side by side

---

<sup>4</sup>From Equation (4.4),  $c^2 \equiv \frac{1}{\mu_0\epsilon_0}$  and  $\sigma_0 \equiv \frac{ne^2}{m_e\nu}$  and  $\omega_P^2 \equiv \frac{ne^2}{m_e\epsilon_0}$ .

Electric Field Snapshots: Quiet Day, 10mHz Current,  $m = 16$

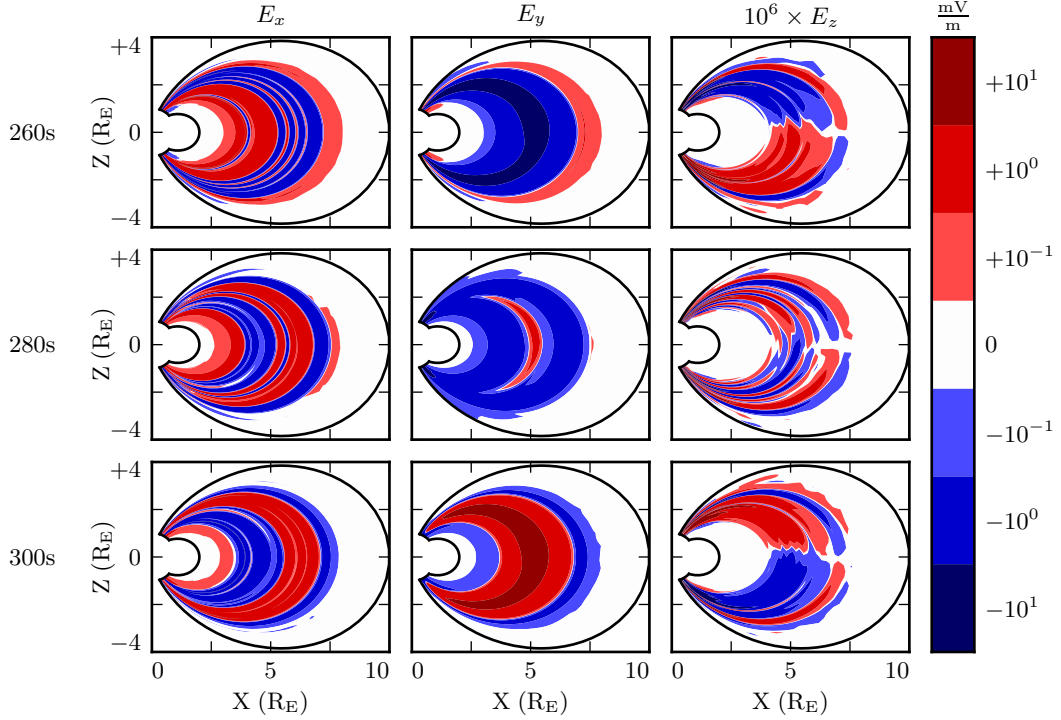


Figure 6.2: Parallel electric fields are smaller than perpendicular electric fields by about six orders of magnitude. As a result, parallel electric fields do not contribute significantly to  $\nabla \times \underline{E}$  in Faraday's law.

870 snapshots of the magnetic fields in runs carried out with and without electron inertial  
871 effects are not visibly distinguishable<sup>5</sup> (not shown).

872 Even if there is no significant feedback through Faraday's law, it's informative to con-  
873 sider the structures that arise in parallel currents and electric fields driven by pertur-  
874 bations in the ring current. For example, in Figure 6.2, the parallel electric field per-  
875 turbation (with maxima near the ionosphere) exhibits the opposite harmonic structure  
876 to the perpendicular electric field components (which peak near the equator).

<sup>5</sup>In a sense, this is reassuring. It ensures that the present section does not cast doubt on the results presented in Chapter 7, where electron inertial effects are neglected.

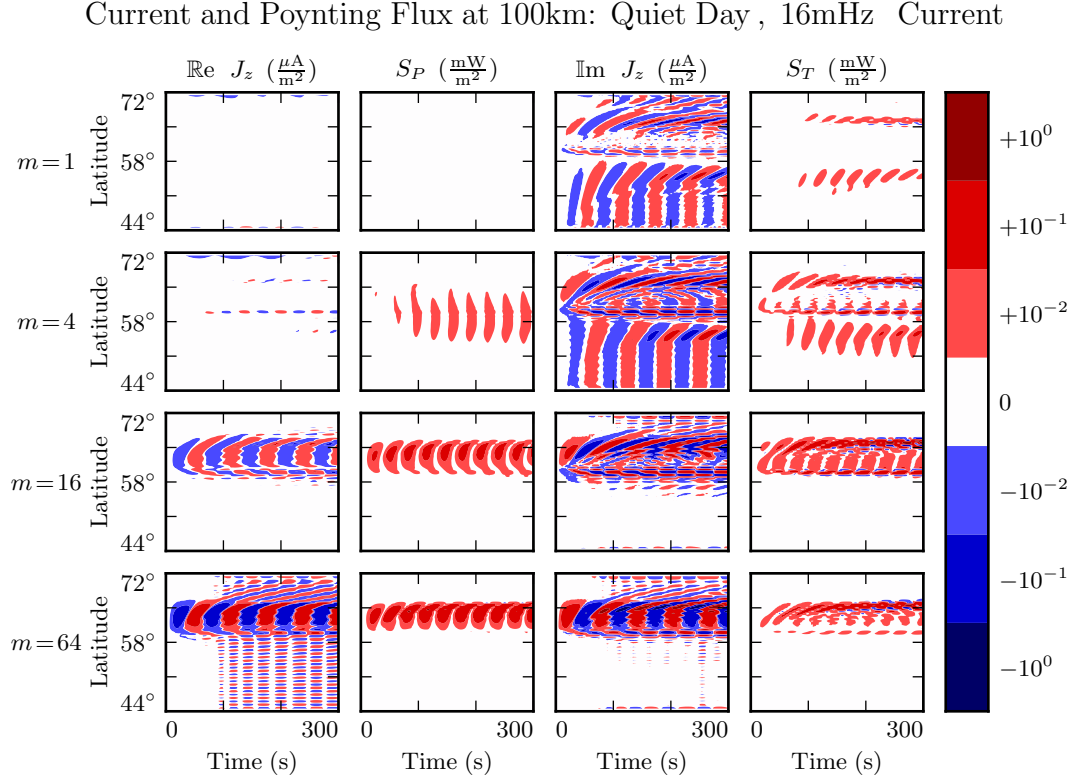


Figure 6.3: Four runs are shown above, one per row, with azimuthal modenumbers of 1, 4, 16, and 64. Columns show slices at 100 km of the real parallel current, poloidal Poynting flux, imaginary current, and toroidal Poynting flux respectively. The similarity visible across columns suggests that the real parallel current follows the poloidal Poynting flux, while the imaginary parallel current follows the toroidal Poynting flux (the toroidal fields are imaginary). At least, this is the case in regions of significant Hall conductivity.

877 At low altitude, the Hall conductivity muddles the poloidal and toroidal electric fields.  
 878 In this region, as shown in Figure 6.3, parallel currents coincide with strong Poynting  
 879 flux. The imaginary component of the current lines up with the toroidal Poynting flux  
 880 (which comes from imaginary  $E_x$  and imaginary  $B_y^*$ ), while the real current lines up  
 881 with the poloidal Poynting flux ( $E_y$  and  $B_x^*$  are real)<sup>6</sup>.

<sup>6</sup>As mentioned in Chapter 5, poloidal field components are in practice overwhelmingly real, indicating that they coincide azimuthally with the (real) driving. Toroidal components are overwhelmingly imaginary, which corresponds to an azimuthal offset.

882 Four runs are shown in Figure 6.3, one per row, with azimuthal modenumbers 1, 4, 16,  
883 and 64. The first and third columns show the real and imaginary components of the  
884 parallel current respectively, in units of  $\mu\text{A}/\text{m}^2$ , sliced at an altitude of 100 km, the edge  
885 of the simulation domain. The second and fourth columns are the poloidal and toroidal  
886 Poynting flux respectively, in units of  $\text{mW}/\text{m}^2$ . Latitude is shown on the vertical axis,  
887 and time on the horizontal axis.

888 At higher altitude, where the Hall conductivity is small, parallel current is associated  
889 only with the toroidal mode. Figure 6.4 shows data from the same runs as Figure 6.3,  
890 arranged in the same way, but the values are taken at an altitude of 1000 km instead of  
891 100 km.

892 In Figure 6.4, as in Figure 6.3, the imaginary component of the parallel current (third  
893 column) coincides more or less with the toroidal Poynting flux (fourth column). How-  
894 ever, the real component of the parallel current (first column) is vanishingly small, even  
895 when the poloidal Poynting flux (second column) is strong.

896 **TODO:** Is this expected? Tikhonchuk[95] looks specifically at the toroidal mode when  
897 considering shear Alfvén waves. Does the poloidal mode count as compressional even  
898 when it's guided? In his 2001 paper, Lysak[61] talks about how circularly-polarized  
899 waves might be interesting. That would be a superposition of the poloidal and toroidal  
900 modes, right? In that paper, he's looking at modes with frequencies of 1 Hz or so, in  
901 the context of the IAR. Lysak and Song's 2003 paper[62] looks at the toroidal mode,  
902 also in the IAR (?).

903 Notably, the Poynting flux waveforms are rectified — they primarily carry energy Earth-  
904 ward. The current, on the other hand, alternates between upward and downward flow.  
905 This effect presumably arises because the current is a linear quantity while the Poynting  
906 flux is quadratic: the electric and magnetic fields that make it up oscillate in phase, so  
907 their product is positive even when they are negative.

908 The magnitude of the parallel current tops out over  $1 \mu\text{A}/\text{m}^2$ , just shy of the up-to-tens  
909 of  $\mu\text{A}/\text{m}^2$  inferred from ground observations and seen in situ[8, 46, 82].

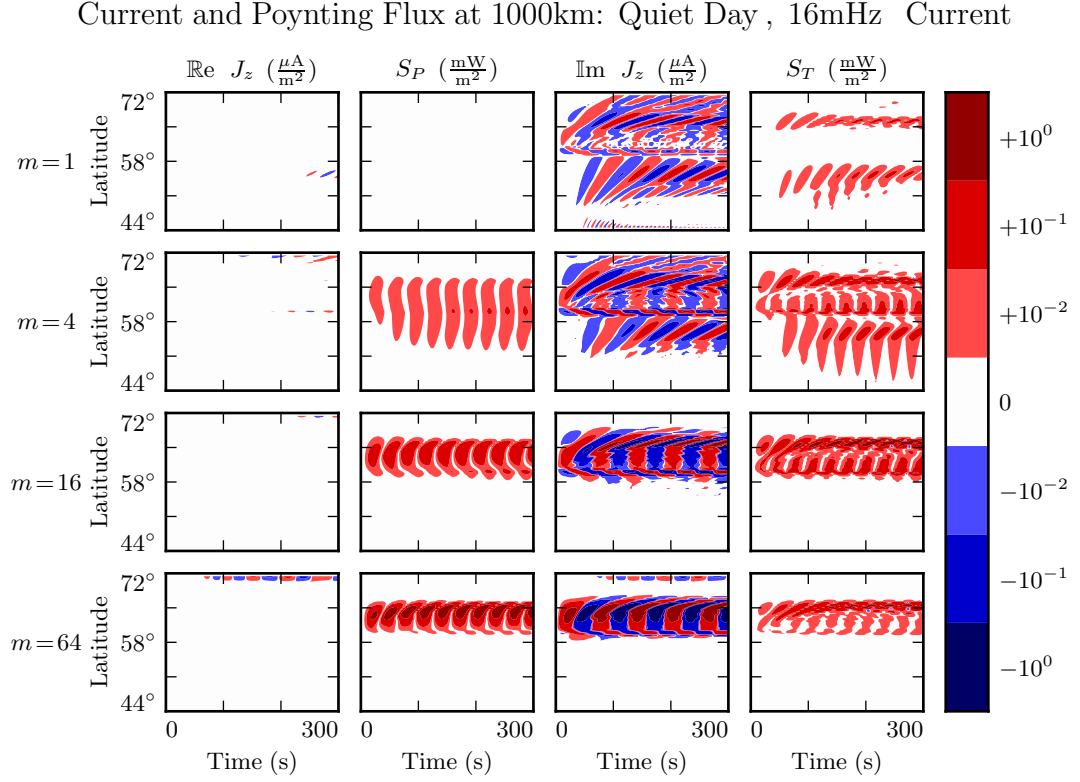


Figure 6.4: The above figure shows the same runs as Figure 6.3, except that the slices are taken at an altitude of 1000 km instead of 100 km. Morphological similarities are still evident between the imaginary parallel current and the toroidal Poynting flux. However, without the Hall conductivity to couple the modes, the poloidal mode does not appear to carry significant current along the field line.

It's also possible to consider the effect of parallel currents and electric fields on the ionosphere's energy budget, per Poynting's theorem:

$$\frac{\partial}{\partial t} u = -\nabla \cdot \underline{E} - \underline{J} \cdot \underline{E} \quad (6.7)$$

910 As shown in Figure 6.5, little energy transfer in the ionosphere is mediated by perpendicular components of the Poynting flux. The parallel component of  $\underline{J} \cdot \underline{E}$  is comparably  
 911 unimportant. The energy deposited in the ionosphere by the Poynting flux matches  
 912 closely with the energy lost to Joule dissipation — as it should, to conserve energy  
 913

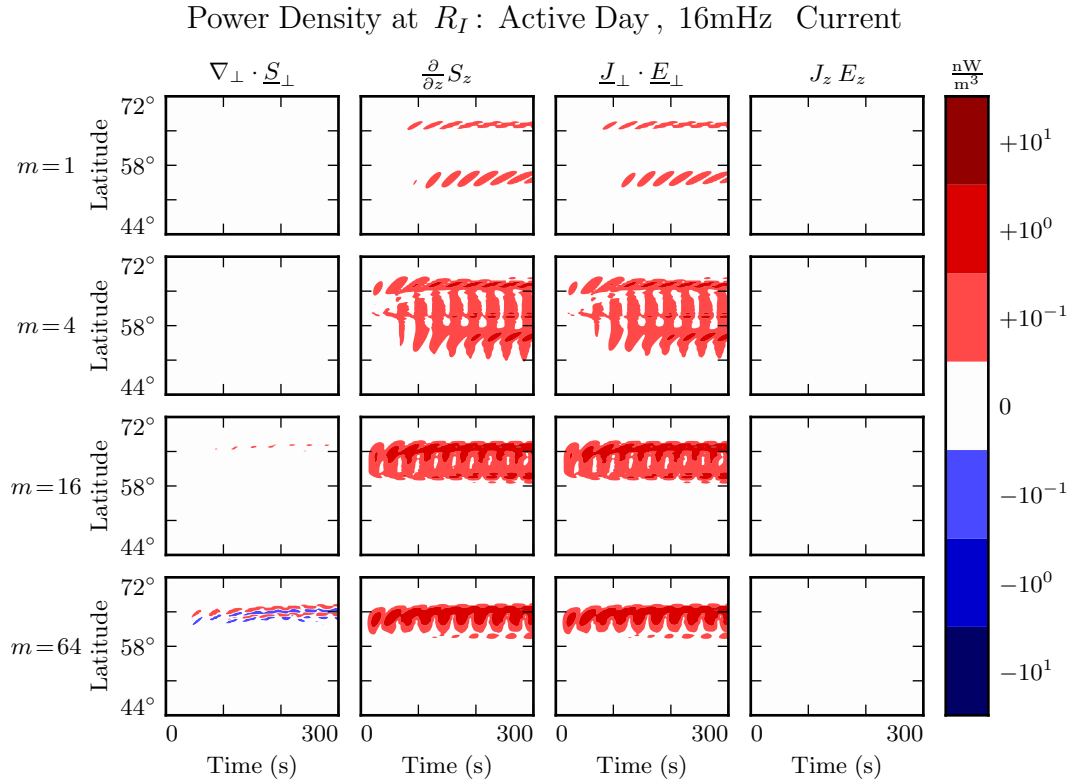


Figure 6.5: While field-aligned currents can be of significant size, they are not particularly good at depositing energy in the ionosphere. Energy deposited by the Poynting flux matches closely with Joule dissipation from the perpendicular currents, while  $J_z E_z$  is smaller by several orders of magnitude.

914 — but according to the model, parallel currents and electric fields do not contribute  
 915 significantly.

### 916 6.3 Inertial Length Scales

917 It's not quite fair to compare the parallel and perpendicular contributions to  $\nabla \times \underline{E}$  as  
 918 is done in Section 6.2. Perpendicular electric fields are on the order of 1 mV/m, with  
 919 wavelengths on the order of  $10^5$  km; they cause magnetic fields to change at a rate of

around 0.1 nT/s. Parallel electric fields, closer to  $10^{-6}$  mV/m, would need to vary over length scales of 0.1 km to match with that.

Such scales are believable. The characteristic length scale of the plasma oscillation is the electron inertial length,  $\frac{c}{\omega_P}$ , which is on the order of 1 km in the auroral ionosphere and 0.1 km in the low-altitude plasmasphere. However, Tuna's usual grid doesn't resolve structures so fine; its resolution bottoms out closer to 10 km. That is, with the inclusion of electron inertial effects, Tuna's grid is too coarse to resolve all of the waves expected to be present. The model is prone to instability as a result.

Figure 6.6 shows a run with perpendicular resolution smaller than the electron inertial length, side by side with an analogous run on the usual grid. In order to carry out the inertial-scale run, several concessions were made to computational cost. The run simulates only a duration of 100 s (other figures in the present chapter, and those in Chapter 7, show 300 s), and the grid covers only the auroral latitudes from  $L = 5$  to  $L = 7$ .

Parallel Electric Fields: Quiet Day, 100s of 16mHz Current,  $m = 16$

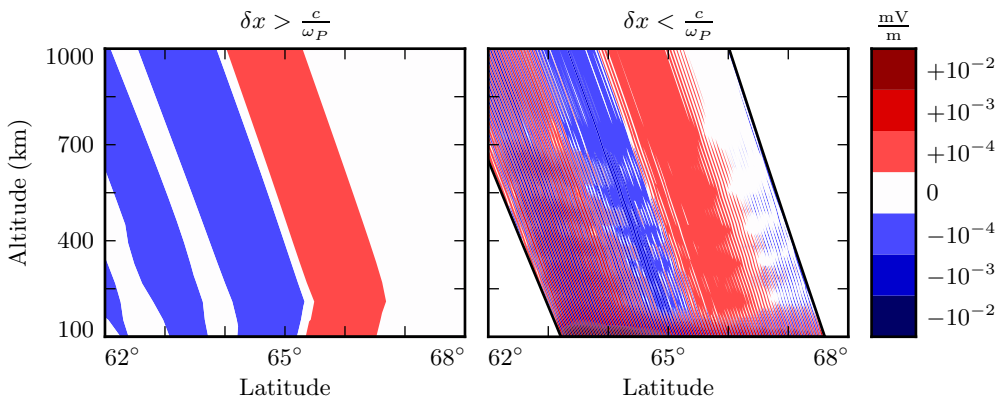


Figure 6.6: The parallel electric field develops significant structure when the perpendicular grid resolution is smaller than the electron inertial length. Unfortunately, such runs are prohibitively expensive. The subplot on the right — which still fails to resolve wave structure properly — represents a 100-fold increase in computational time.

934 Even so, the run presents a significant computational expense. Spread over 16 cores, a  
935 100 s run on Tuna’s usual grid takes well under an hour. The inertial-scale run barely  
936 finished in 96 hours, the cutoff at the Minnesota Supercomputing Institute<sup>7</sup>.

937 The snapshot shown in Figure 6.6 uses a perpendicular grid resolution of 0.7 km at the  
938 Earthward edge, which just satisfies the Nyquist rate for the minimum inertial length  
939 of 1.7 km. It’s still too coarse. There is clearly some small-scale structure developing in  
940 the ionosphere, but it’s not well resolved. The large number of “wiggles” portends an  
941 imminent crash.

## 942 6.4 Discussion

943 The present chapter is a proof of concept: the addition of electron inertial effects to  
944 Tuna presents a promising first-principles-based approach to the investigation of parallel  
945 currents and electric fields associated with field line resonances. Electric fields arise  
946 which are consistent in magnitude with those predicted by the dispersion relation, and  
947 parallel currents fall within an order of magnitude or so of observed values, even when  
948 inertial length scales are not properly resolved.

949 Results in Section 6.2 suggest a disparity between poloidal and toroidal FLRs in terms of  
950 the parallel current response. At low altitude, where the two modes are directly coupled  
951 by the Hall conductivity, both seem to be accompanied by parallel currents. However, in  
952 regions of low Hall conductivity, parallel currents appear to preferentially accompany  
953 toroidal waves. The cause is unclear, and a topic worthy of future investigation.

954 Future work in this vein may also consider the scales and structures that arise in regions  
955 of parallel current. For example, one might consider the relationship between the dy-  
956 namic height-integrated potentials and the accompanying parallel currents, specifically  
957 with respect to the Knight Relation[51]. Inertial effects could furthermore be accom-  
958 panied by test particles, in order to gauge the properties of particle precipitation that  
959 could accompany global Alfvénic potential structures.

---

<sup>7</sup>Runtime goes as the inverse square of grid resolution. Not only does finer resolution require more grid cells, but it also gives rise to proportionally smaller crossing times, imposing a smaller time step.

960 Unfortunately, simulations are prone to instability when inertial length scales are not  
961 properly resolved. And, at least at present, resolving those scales poses a prohibitive  
962 computational expense. For this reason, the consideration of inertial effects is limited to  
963 the present chapter; results in Chapter 7 make use of the core version of Tuna presented  
964 in Chapter 5, which does not include the effects of electron inertia.

965 Notably, the addition or omission of parallel currents and electric fields does not appear  
966 to significantly alter the behavior of perpendicular electric fields or magnetic fields.  
967 Because the parallel electric fields are relatively small,  $\nabla \times \underline{E}$  is essentially unaffected  
968 by their inclusion.

969 **Chapter 7**

970 **Numerical Results**

971 A primary motivation for the development of Tuna is the fact that FLRs vary in interesting ways as a function of azimuthal modenumber, and that existing numerical models  
972 are limited in their ability to examine such behaviors. The present chapter discusses  
973 the core results that have so far been obtained.  
974

975 **7.1 Modenumber and Compression**

976 It's well known that the poloidal FLR mode is compressional at low modenumber,  
977 but guided at high modenumber. However, the relationship is not well quantified.  
978 Theoretical work has historically been concerned with the limits  $m \rightarrow 0$  and  $m \rightarrow$   
979  $\infty$ [14, 78], and only a handful of satellite observations have explicitly considered an  
980 event's azimuthal modenumber[17, 70, 90]. Using results from Tuna, the present section  
981 examines the strength of the poloidal wave's compressional component at an ensemble  
982 of finite modenumbers.

983 Figures 7.1 and 7.2 show magnetic field snapshots taken from a pair of runs. The first  
984 uses a small azimuthal modenumber, and the second uses a large one. The runs are  
985 otherwise identical: both simulations use the quiet dayside ionospheric profile, and both  
986 are driven at 22 mHz.

987 The differences between the two runs are striking. At low modenumber, wave activity  
988 is visible throughout the simulation domain. Structure in the poloidal magnetic field is  
989 only vaguely governed by the dipole geometry, and the compressional magnetic field is  
990 comparably strong to the two perpendicular components.

991 In contrast, at high modenumber, the poloidal magnetic field is localized to the  $L$ -shells  
992 where the driving is delivered:  $4 \lesssim L \lesssim 6$ . The compressional field is weaker than  
993 the poloidal field by at least an order of magnitude. A third-harmonic poloidal mode  
994 is visible at the outer boundary — its magnitude is just barely large enough to be  
995 visible on the logarithmic scale. The gap between  $L \sim 5$  (where 22 mHz matches a first-  
996 harmonic FLR) and  $L \sim 10$  (where 22 mHz matches a third-harmonic FLR) speaks to  
997 the evanescence of non-guided waves above the compressional Alfvén cutoff frequency<sup>1</sup>.

998 In both the low- $m$  and high- $m$  runs, toroidal activity is more or less coincident with  
999 poloidal activity — as is to be expected, since the driving is purely poloidal, and the  
1000 poloidal mode rotates to the toroidal mode over time. It is further notable that the  
1001 toroidal mode is sharply guided. Particularly in Figure 7.2, strong, narrow, toroidal  
1002 FLRs of opposite phase can be seen oscillating very close to one another. Strong poloidal  
1003 waves, in contrast, are smeared in  $L$ .

1004 Snapshots are not shown for runs carried out using the other ionospheric profiles (active  
1005 day, quiet night, and active night). The morphology of their waves is qualitatively  
1006 similar. The differences between the profiles is considered in Sections 7.2 to 7.4.

1007 Figure 7.3 quantifies the compressional component of the poloidal mode as a function of  
1008 modenumber. Each subplot corresponds to a different run of Tuna — the runs shown in  
1009 Figures 7.1 and 7.2 are in the rightmost column, second from the top and second from the  
1010 bottom respectively. The red line indicates the ratio between the RMS compressional  
1011 magnetic field and the RMS poloidal magnetic field; both averages are taken over the  
1012 entire simulation “volume” each time step. Mean values are shown in black.

---

<sup>1</sup>See Section 4.4.

1013 At  $m = 1$ , the compressional and poloidal magnetic fields are comparable in magnitude.  
1014 As  $m$  increases, however, the compressional component quickly falls off. The compres-  
1015 sional component is half the strength of the poloidal component at  $m \sim 5$ , and a quarter  
1016 by  $m \sim 10$ .

1017 A slight frequency dependence is apparent across each row in Figure 7.3. Compressional  
1018 coupling falls off slower for waves at higher frequency. This is because higher-frequency  
1019 waves are that much closer to the cutoff frequency (described in Section 4.4), and so  
1020 their propagation across  $L$ -shells is that much less evanescent.

1021 Similarly, poloidal waves are more prone to compression on the nightside. Due to the  
1022 higher Alfvén speed on the nightside, driving is delivered at  $L \sim 6$  instead of  $L \sim 5$ . The  
1023 cutoff frequency depends inversely on radial distance. For nightside runs (not shown),  
1024  $\left| \frac{B_z}{B_x} \right|$  falls to 50% at  $m \sim 8$  and to 25% at  $m \sim 16$ .

1025 Notably, the waves considered in the present work are fundamental harmonics. The  
1026 compressional behavior of the poloidal mode may vary for the (more-common) second  
1027 harmonic: Radoski suggests that the asymptotic value of  $\left| \frac{B_z}{B_x} \right|$  is inversely proportional  
1028 to the harmonic number[78].

Magnetic Field Snapshots: Quiet Day , 22mHz Current,  $m = 2$

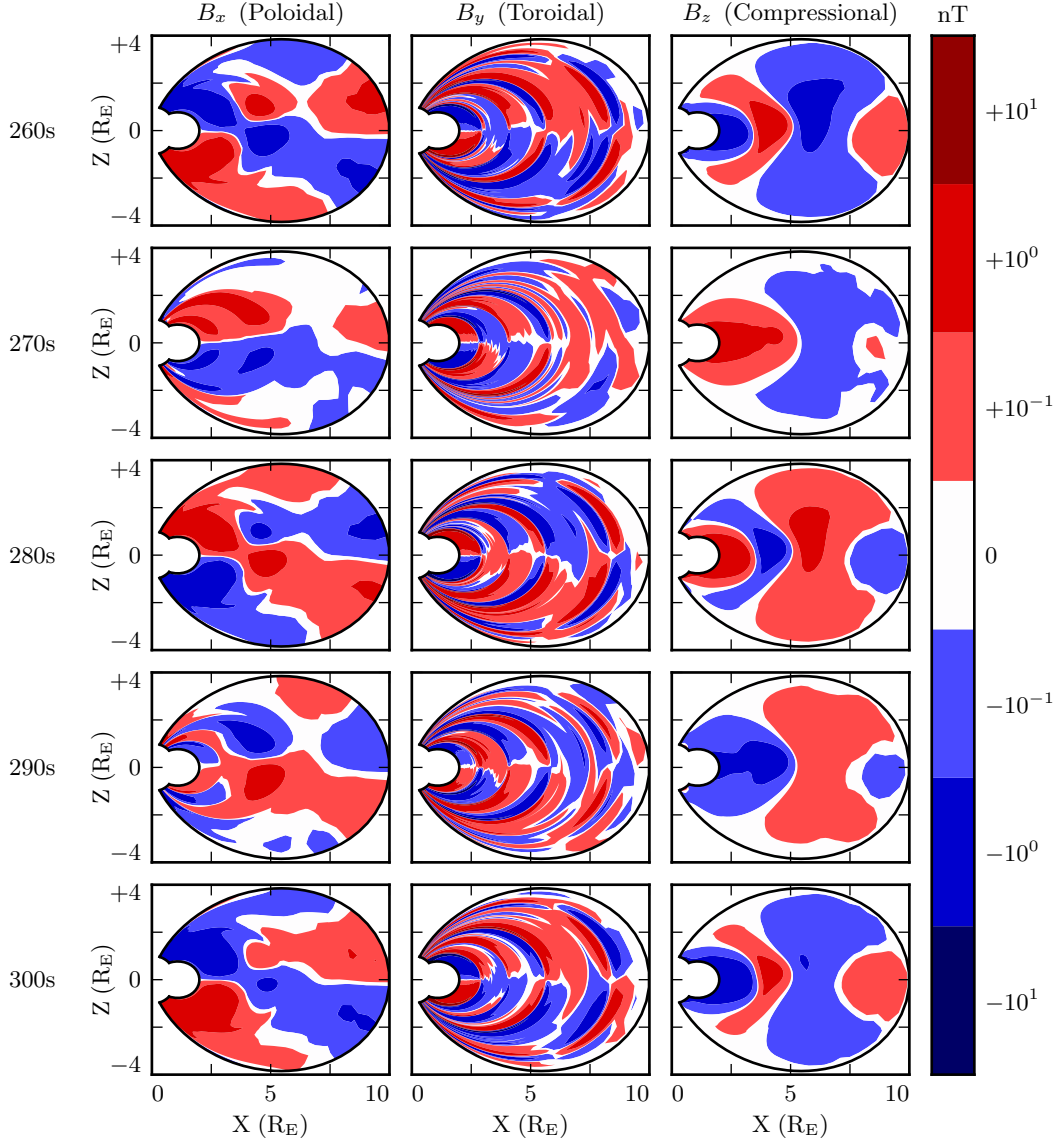


Figure 7.1: Each row in the above figure is a snapshot in time. The three columns show the simulated poloidal, toroidal, and compressional magnetic field. Due to the run's low azimuthal modenumber, the poloidal mode has a significant compressional component. This is visible both in the fact that  $B_z$  is comparable in size to  $B_x$ , and in that structure in  $B_x$  is only vaguely guided by the geometry of the magnetic field. Toroidal waves, in contrast, are sharply guided.

Magnetic Field Snapshots: Quiet Day , 22mHz Current,  $m = 32$

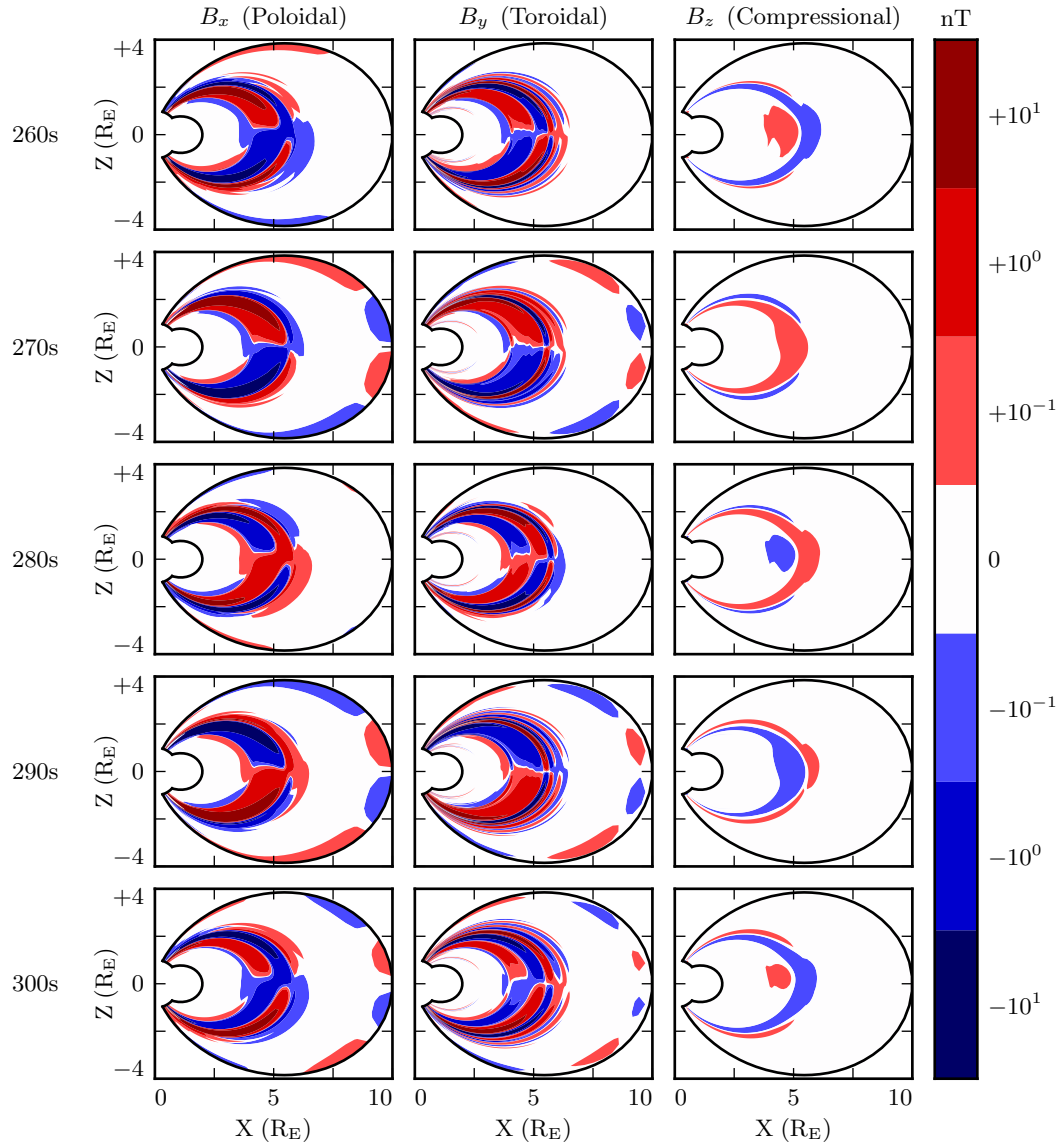


Figure 7.2: The above figure is analogous to Figure 7.1, but the runs use a larger azimuthal modenumber. The change has a dramatic effect. The poloidal wave is concentrated much more sharply in  $L$ , and its compressional component is weakener by an order of magnitude. Regardless of modenumber, toroidal waves exist at a range of  $L$  shells similar to poloidal waves, and show sharp definition across  $L$ -shells.

### Compressional Coupling to the Poloidal Mode: Quiet Day

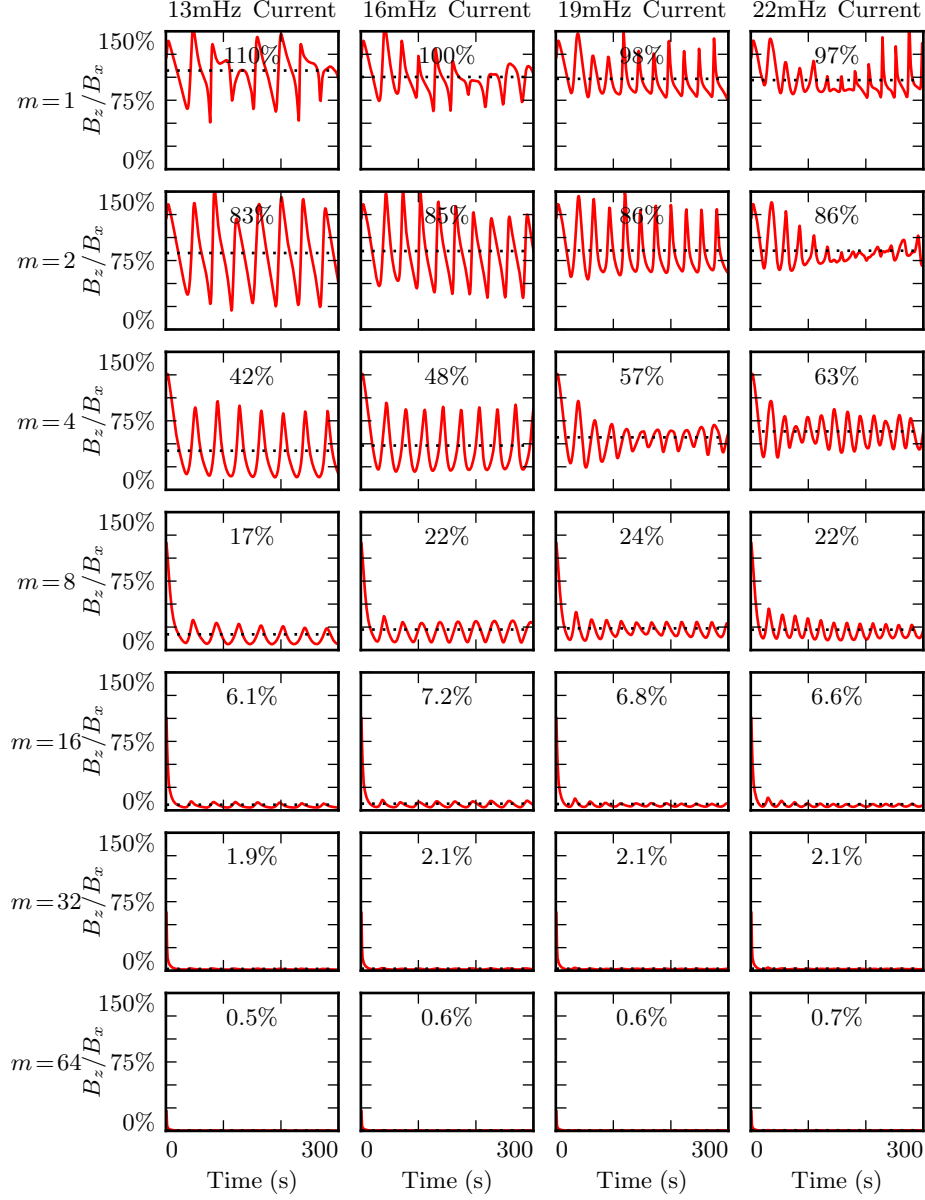


Figure 7.3: Each subplot above corresponds to a different run; the runs shown in Figures 7.1 and 7.2 are in the rightmost column, second from the top and second from the bottom respectively. Red lines indicate the ratio between the RMS compressional and poloidal magnetic fields. Mean values are shown in black. The compressional field is comparable to the poloidal field at  $m = 1$ , but falls quickly.

1029 **7.2 Resonance and Rotation on the Dayside**

1030 In his 1974 paper, Radoski argues that a poloidally-polarized wave should asymptotically  
1031 rotate to the toroidal polarization[78] as a result of the curved derivative in the  
1032 meridional plane. The question of finite poloidal lifetimes is considered further in a 1995  
1033 paper by Mann and Wright[66]. Their numerical work used a straightened field line,  
1034 with an Alfvén speed gradient in the “radial” direction. They also found a rotation over  
1035 time from poloidal to toroidal polarization, with the characteristic time proportional to  
1036 the azimuthal modenumber.

1037 The present section builds on the aforementioned results by relaxing several of their non-  
1038 physical assumptions. Tuna’s geometry is more realistic than Radoski’s half-cylinder or  
1039 the box model used by Mann and Wright. Previous work has considered the evolution  
1040 of an initial condition, while the simulations shown below include driving delivered  
1041 over time. In addition, Tuna features a finite, height-resolved ionospheric conductivity  
1042 profile, rather than the perfectly-reflecting boundaries used in the past.

Each subplot in Figure 7.4 is analogous to Figure 3 in Mann and Wright’s paper[66]. Blue lines show the total energy in the poloidal mode as a function of time. Red lines show toroidal energy. Runs are organized analogous to those in Figure 7.3: drive frequency is constant down each column, and azimuthal modenumber is constant across each row. Axis bounds are held constant across all subplots. The poloidal and toroidal energy are computed by integrating over the electromagnetic energy density, per Poynting’s theorem:

$$U_P = \int \frac{dV}{2\mu_0} \left( B_x^2 + \frac{1}{v_A^2} E_y^2 \right) \quad U_T = \int \frac{dV}{2\mu_0} \left( B_y^2 + \frac{1}{v_A^2} E_x^2 \right) \quad (7.1)$$

1043 Where the differential volume  $dV$  is computed using the Jacobian<sup>2</sup> to account for Tuna’s  
1044 unusual geometry. The integral is evaluated in  $u^1$  and  $u^3$  but not  $u^2$  (Tuna’s missing  
1045 half-dimension), which gives energy in units of gigajoule per radian. More than anything  
1046 else, this serves as a reminder that Pc4 pulsations are localized in MLT.

---

<sup>2</sup>See Section 5.1.

1047 The 28 runs shown in Figure 7.4 use an ionospheric profile corresponding to the dayside  
1048 during times of low solar activity, where the conductivity is relatively high. The active  
1049 and quiet dayside profiles are briefly contrasted in Section 7.4; for the most part, the  
1050 focus of the present work is on the difference between the dayside and the nightside  
1051 (Section 7.3). Differences between the two dayside profiles are small in comparison.

1052 The fact that red (toroidal) lines appear at all in Figure 7.4 speaks to a net rotation  
1053 of energy from the poloidal mode to the toroidal. As discussed in Section 5.3, Tuna’s  
1054 driving is delivered purely into the poloidal electric field (reflecting a perturbation in  
1055 the magnitude of the ring current).

1056 As expected, the rotation from poloidal to toroidal is slowest at large azimuthal mode-  
1057 numbers. The toroidal energy overtakes the poloidal energy within a single drive period  
1058 at  $m = 4$ ; at  $m = 64$ , the most of the energy is in the poloidal mode for  $\sim 10$  periods.  
1059 However, the relationship between azimuthal modenumber and rotation timescale is  
1060 not linear, as was suggested by Mann and Wright. Instead, in a practical setting, the  
1061 rotation is fastest at  $m \sim 4$ .

1062 This is explained by the compressional character of the poloidal mode. At very low  
1063 modenumber, energy in the poloidal mode moves readily across  $L$ -shells. A significant  
1064 fraction of that energy is lost to the outer boundary before rotating to the toroidal  
1065 mode. At high modenumber — as discussed in Section 7.1 — compressional propagation  
1066 is evanescent, so all energy in the poloidal mode must ultimately rotate to the toroidal  
1067 mode or be lost to Joule dissipation.

1068 Joule dissipation is a major player in the system’s energy economy. However, due to the  
1069 highly conductive dayside ionosphere, dissipation timescales are in the tens of Pc4 wave  
1070 periods. Energy loss through Joule dissipation asymptotically balances energy input  
1071 from driving, but most of that energy is not lost until after it has rotated from the  
1072 poloidal mode to the toroidal. As such, in most runs shown in Figure 7.4, the energy  
1073 content of the toroidal mode asymptotically exceeds that of the poloidal mode.

1074 The asymptotic energy content of the system also depends on how well the drive fre-  
1075 quency matches the local eigenfrequency. If the two do not match, energy is lost to  
1076 destructive interference between the standing wave and the driving.

1077 In principle, energy moves between the poloidal and toroidal modes due to their direct  
1078 coupling through the ionospheric Hall conductivity. In practice, this effect is small.  
1079 When the runs shown in Figure 7.4 are repeated with the Hall conductivity set to zero,  
1080 the resulting energy curves are not visibly different.

1081 The low- $m$  runs at 19 mHz merit additional discussion. These runs accumulate energy  
1082 over a large number of wave periods, while the low- $m$  waves at 13 mHz, 16 mHz, and  
1083 22 mHz do not. This effect is likely nonphysical. At 19 mHz, a third-harmonic resonance  
1084 forms very close to the outer boundary. The resonance is likely enhanced by nonphysical  
1085 reflections against the simulation’s boundary conditions.

1086 The presence of individual harmonics can be seen in the contours shown in Figures 7.5  
1087 and 7.6. These figures show the same runs as Figure 7.4, arranged in the same way on  
1088 the page. However, instead of showing the total energy integrated over the simulation  
1089 domain, the energy densities are averaged over the volume of each flux tube individually.  
1090 Figure 7.5 shows contours of poloidal energy density and Figure 7.6 shows toroidal  
1091 energy density.

1092 The top few rows of Figure 7.5 confirm that the poloidal mode’s compressional nature is  
1093 to blame for its failure to accumulate energy at low modenumber. Waves move so readily  
1094 across field lines that no visible amount of energy builds up at  $L \sim 5$ , the location of the  
1095 driving. Some energy moves inward, and is trapped by the peak in Alfvén speed just  
1096 inside the plasmapause, while the rest moves to the outer boundary. The time spent  
1097 moving across field lines counts against the poloidal mode’s finite lifetime, inhibiting  
1098 the buildup of poloidal energy density even at  $L$ -shells where the wave matches the local  
1099 eigenfrequency.

1100 As  $m$  increases, the energy distribution becomes more concentrated in  $L$ , though indi-  
1101 vidual features remain fairly broad. At  $m = 8$ , runs at 13 mHz and 16 mHz are inclined  
1102 to build up energy just inside the plasmapause, while those at 19 mHz and 22 mHz res-  
1103 onate just outside the plasmapause; in all four cases, the energy is spread over a range  
1104 of at least 1 in  $L$ .

1105 The peak energy density in the bottom-right run (22 mHz driving,  $m = 64$ ) is by far the  
1106 largest of any run in Figure 7.5. The azimuthal modenumber is large, so the poloidal

1107 mode is purely guided; energy is not smeared across multiple  $L$ -shells. And, crucially, the  
1108 frequency of the driving matches closely with the Alfvén frequency at  $L \sim 5$ . Other runs  
1109 on the bottom row are also guided, but they reach lower asymptotic energy densities  
1110 because of a mismatch between the drive frequency and the local eigenfrequency —  
1111 resulting in destructive interference between the standing wave and its driver.

1112 The eigenfrequencies in the magnetosphere are significantly affected by the location of  
1113 the plasmapause. When the runs in Figure 7.5 are repeated with the plasmapause at  
1114  $L = 5$  instead of  $L = 4$ , the strongest resonance at  $L \sim 5$  drops from 22 mHz to 16 mHz  
1115 (not shown).

1116 Whereas the poloidal contours are smeared over a swath of  $L$ -shells (though the high- $m$   
1117 runs less so), the toroidal contours in Figure 7.6 appear only where the wave frequency  
1118 matches the local eigenfrequency. A horizontal line drawn through the Alfvén speed  
1119 frequency profiles (recall Figure 3.1) intersects the profile up to three times: once as  
1120 the Alfvén frequency drops through the Pc4 range from its low-latitude peak, again as  
1121 the Alfvén frequency rises sharply at the plasmapause, and a third time as the Alfvén  
1122 frequency drops asymptotically. Toroidal waves can be seen resonating at all three of  
1123 these locations in the  $m = 4$ , 22 mHz run in Figure 7.6, along with a third harmonic at  
1124 large  $L$ . This is consistent with observations: toroidal resonances are noted for having  
1125 frequencies which depend strongly on  $L$ , in contrast to the poloidal mode's less-strict  
1126 relationship between frequency and location.

1127 In only one of the runs shown in Figure 7.5 does the poloidal mode attain an energy  
1128 density on the order of  $10^{-1}$  nJ/m<sup>3</sup>. On the other hand, the toroidal mode reaches  
1129  $\sim 10^{-1}$  nJ/m<sup>3</sup> in six of the runs in Figure 7.6. That is, the poloidal mode only exhibits  
1130 a high energy density on the dayside only when conditions are ideal; the toroidal mode  
1131 isn't nearly so particular.

Poloidal (Blue) and Toroidal (Red) Energy: Quiet Day

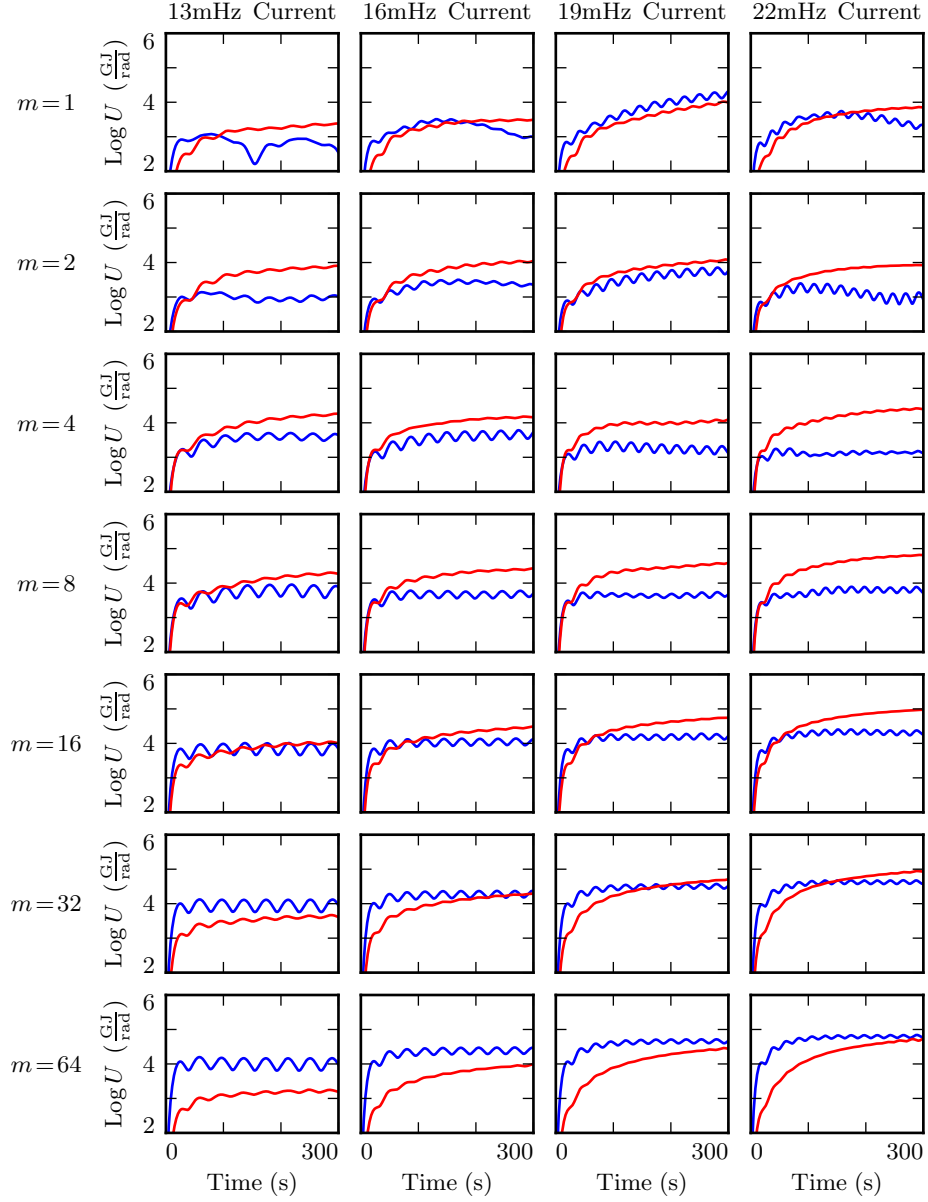


Figure 7.4: Each subplot above shows the poloidal (blue) and toroidal (red) energy for a simulation as a function of time. Each row contains four simulations, each with the same azimuthal modenumber; the seven rows in each column share a drive frequency. Driving is purely poloidal, but energy rotates asymptotically to the toroidal mode, and rotation is slowest at high modenumber.

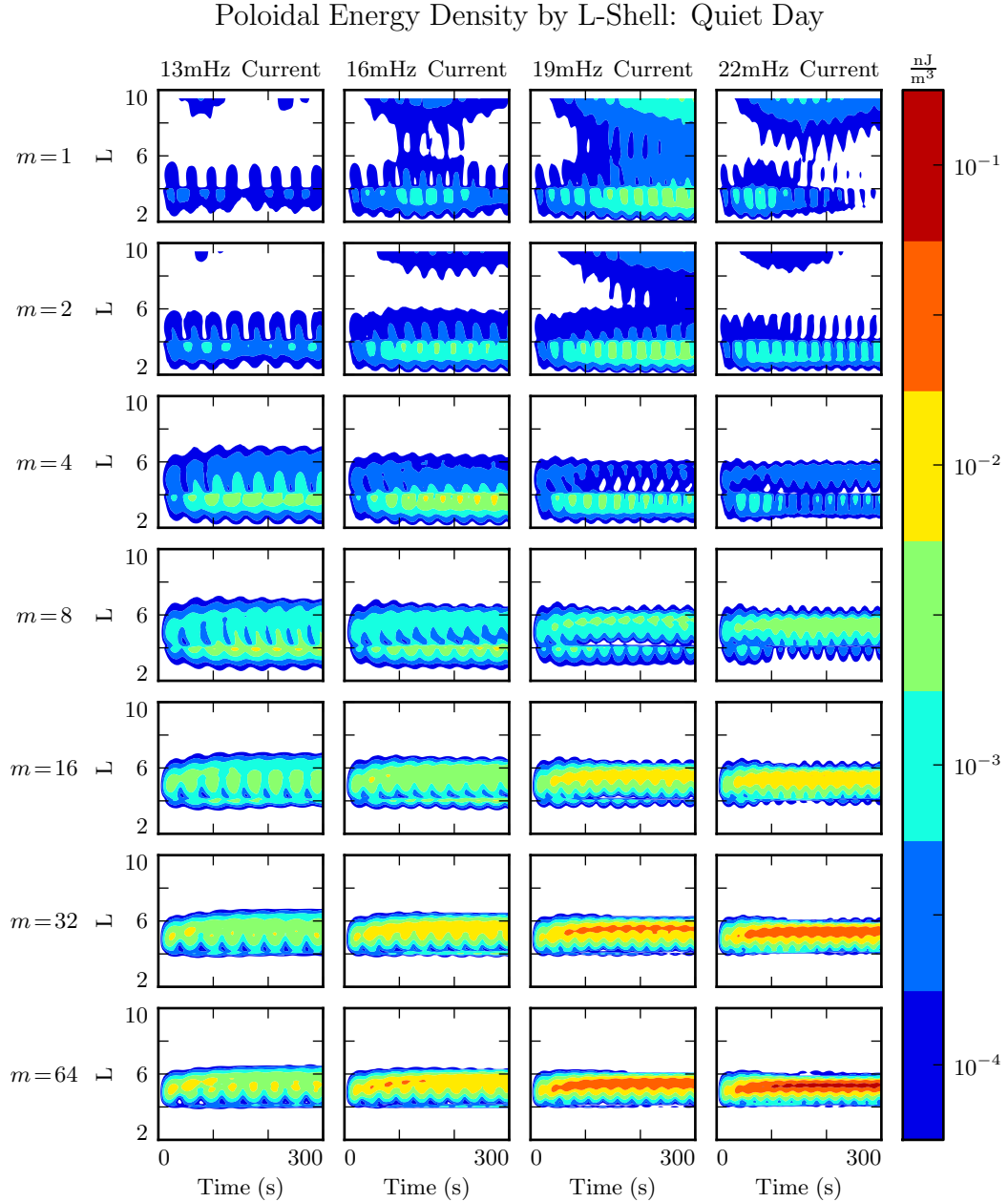


Figure 7.5: At low modenumber (top rows), the compressional nature of the poloidal mode allows energy to escape the simulation. At high modenumber (lower rows), the poloidal mode is guided; energy is trapped at the  $L$ -shell where it's injected, and rotation to the toroidal mode is slow — ideal conditions for resonance. But energy buildup is lackluster except where the drive frequency matches the local eigenfrequency (best in the rightmost row).

### Toroidal Energy Density by L-Shell: Quiet Day

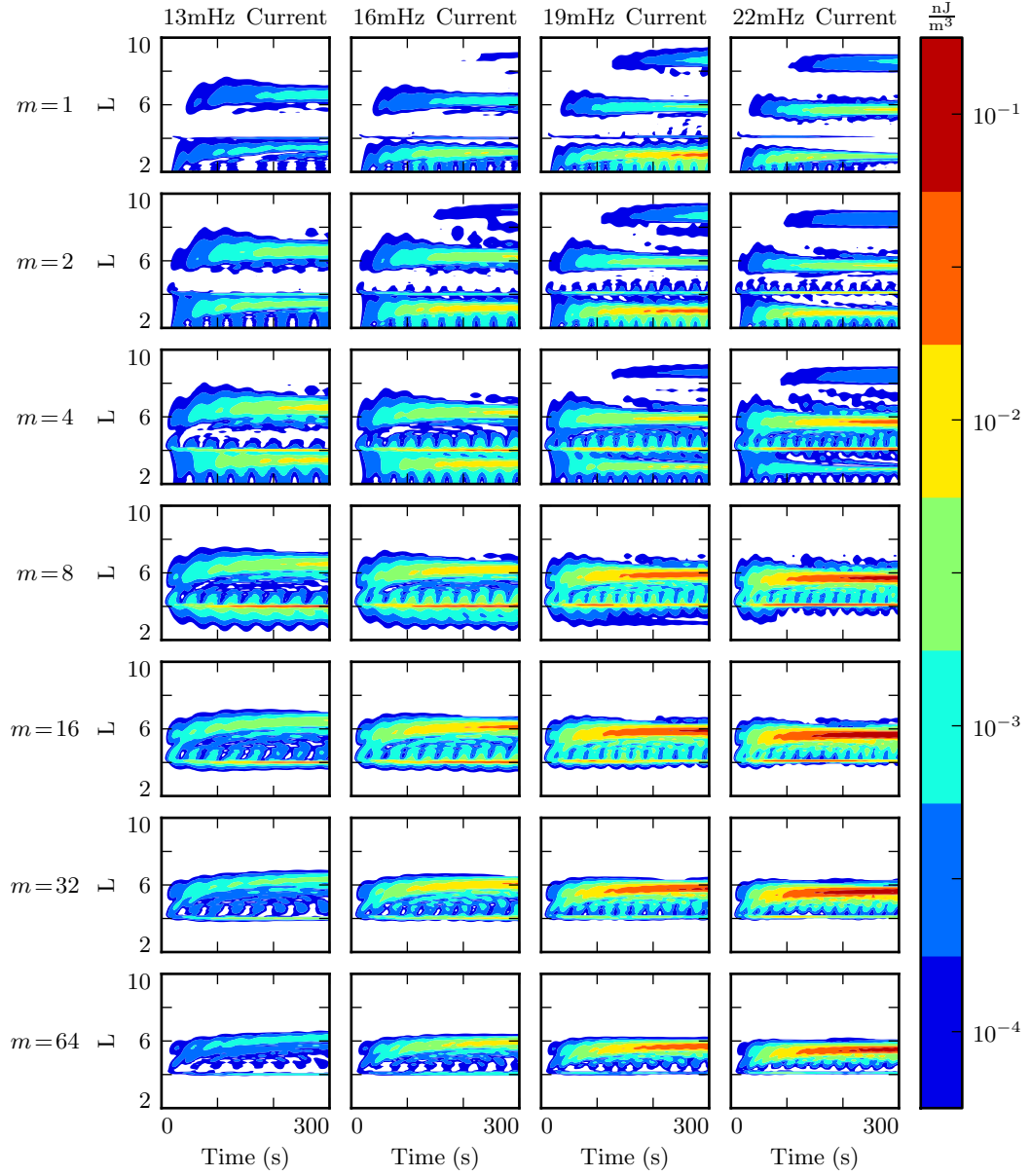


Figure 7.6: Whereas the poloidal mode is smeared in  $L$  due to its compressional nature, the toroidal mode is focused at  $L$  shells where it's resonant. In general, when the conductivity is high, the toroidal mode also exhibits a higher asymptotic energy density than the poloidal mode (Figure 7.5).

1132 **7.3 Resonance and Rotation on the Nightside**

1133 Compared to the dayside ionosphere employed in Section 7.2, the nightside exhibits two  
1134 major differences. The ionospheric conductivity is lower, and the Alfvén speed is higher.  
1135 Runs in the present section specifically use Tuna’s ionospheric profile corresponding to  
1136 the nightside during quiet solar conditions. Behavior on the active nightside is qualita-  
1137 tively similar, though less drastic, since the conductivity on the active nightside is not  
1138 so low. The two nightside profiles are briefly compared in Section 7.4, but for the most  
1139 part the present work is concerned with the behavior of the nightside compared to that  
1140 on the dayside.

1141 Other than the change in ionospheric profile, Figures 7.7 to 7.9 are analogous to Fig-  
1142 ures 7.4 to 7.6. Each subplot corresponds to a different 300 s run of Tuna. Drive  
1143 frequency is constant down each column, and azimuthal modenumber is constant across  
1144 each row.

1145 The low conductivity on the nightside gives rise to strong Joule dissipation. Waves are  
1146 damped out in just a few bounces, so asymptotic energy values are reached quickly.  
1147 No combination of frequency and modenumber gives rise to the accumulation of energy  
1148 over multiple drive periods.

1149 As on the dayside, rotation of energy from the poloidal to toroidal mode is fastest at  
1150  $m \sim 4$ . Unlike the dayside, however, dissipation on the nightside is fast compared to  
1151 the rotation of energy to the toroidal mode. Toroidal energy does not asymptotically  
1152 exceed the poloidal energy by a significant margin in any run. At  $m = 64$ , where the  
1153 rotation timescale is slowest, no more than 10 % of the energy in the poloidal mode  
1154 rotates to the toroidal mode before being lost.

1155 **TODO:** The damping on the quiet nightside is so severe that basically nothing resonates  
1156 anywhere. Should we show the active nightside instead?

1157 **TODO:** Timescale is probably about like the dayside, about one period at low  $m$  and  
1158 order of ten periods at high  $m$ .

Poloidal (Blue) and Toroidal (Red) Energy: Quiet Night

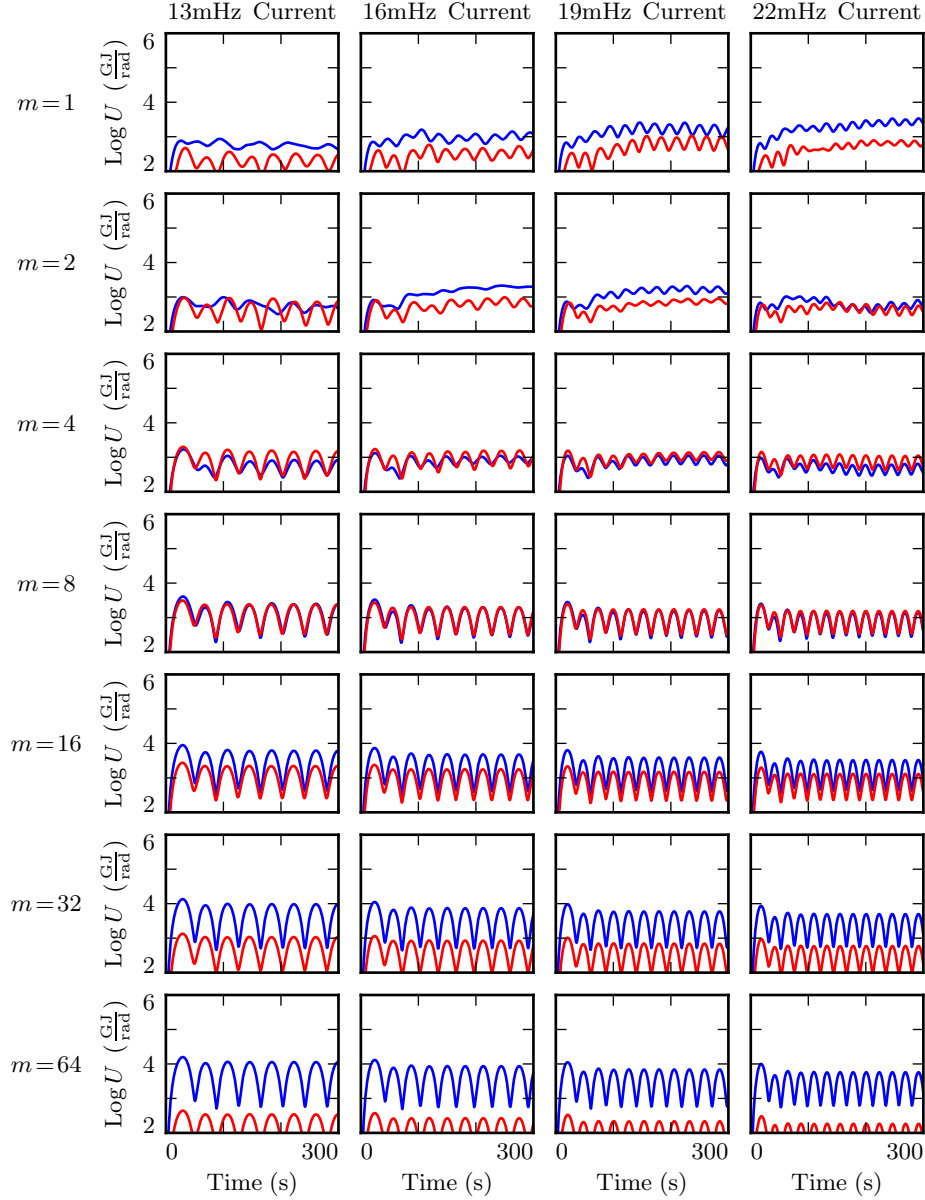


Figure 7.7: The energy content of each FLR on the nightside resembles that of a damped, driven oscillator. Energy is periodically added to the system, but most is lost too fast to rotate to the toroidal mode, particularly at high modenumber. There is no significant buildup of energy over multiple periods. Runs at  $m = 1$  (top row) are an apparent exception, likely due to a nonphysical interaction with the boundary.

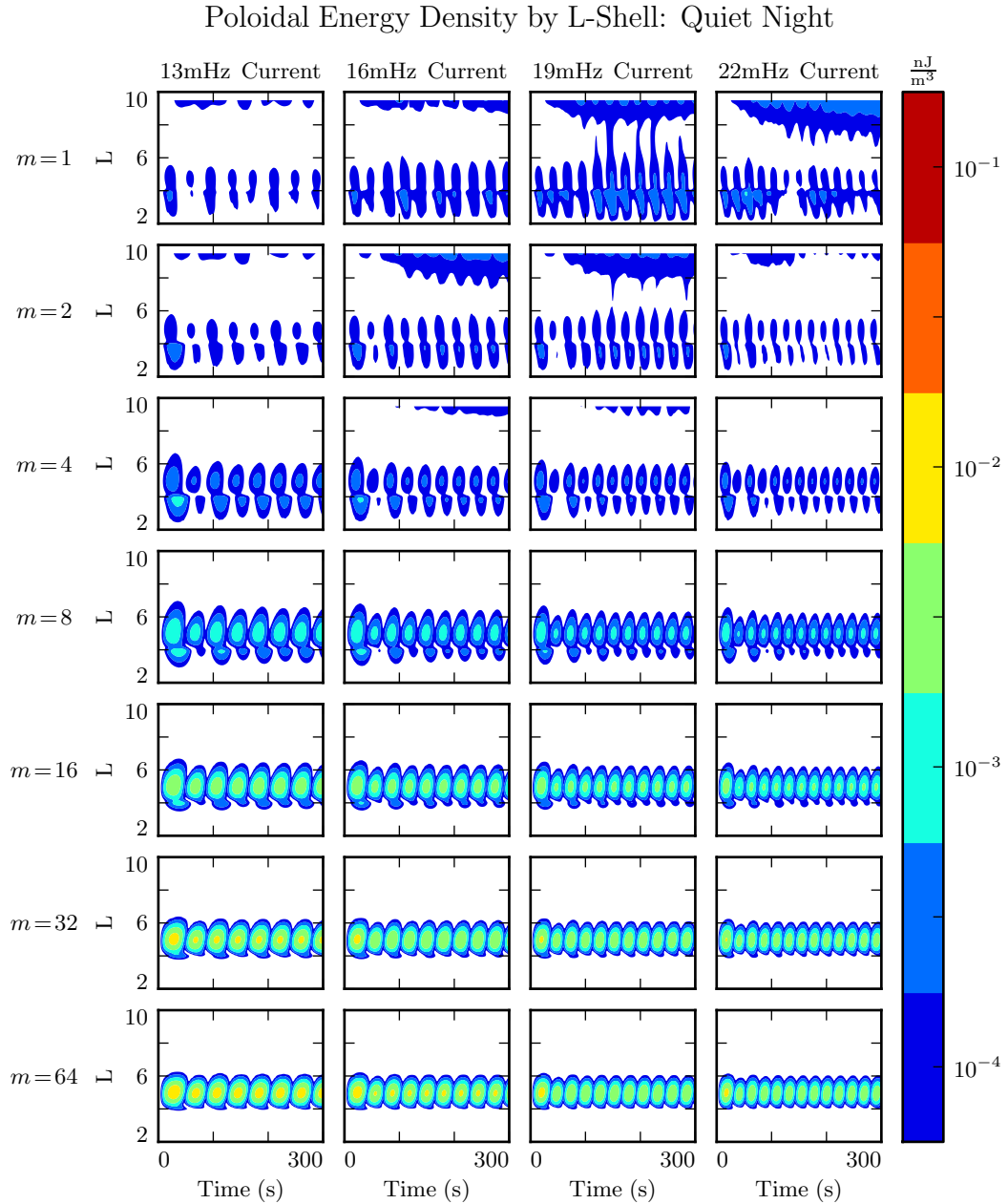


Figure 7.8: As on the dayside (Figure 7.8), low-modenumber poloidal waves (top rows) readily propagate across  $L$ -shells and escape the simulation domain. Energy density builds up most effectively at high modenumbers, where the poloidal mode is guided, and poloidal-to-toroidal rotation is slow. Even in this case, however, dissipation is fast enough to prevent energy from accumulating over multiple drive periods.

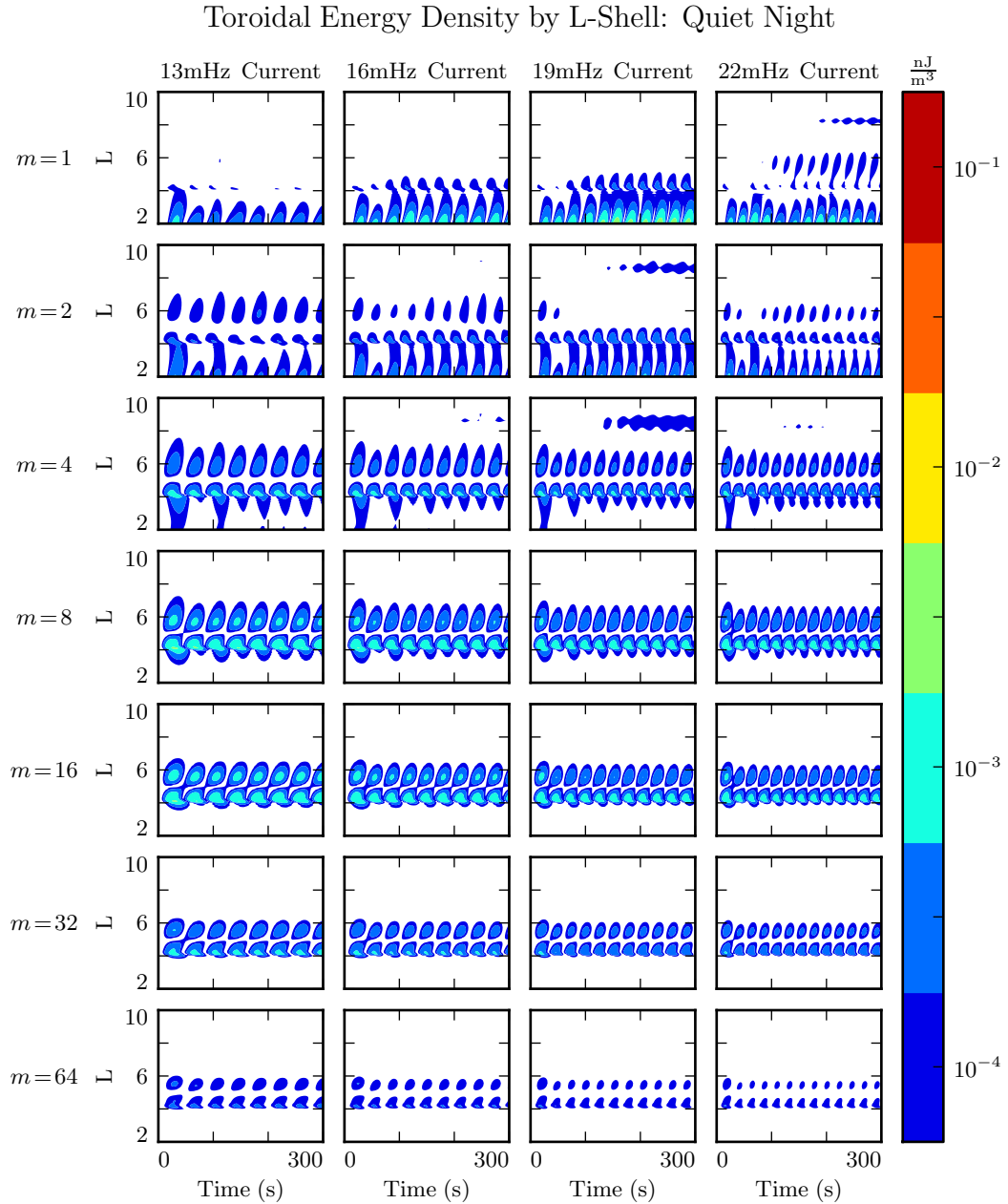


Figure 7.9: On the dayside (Figure 7.9), most energy rotates asymptotically to the toroidal mode. On the night side, the same is not true, since the poloidal mode quickly loses energy to Joule dissipation. At high modenumber, where the poloidal-to-toroidal rotation timescale is in the tens of wave periods, almost all of the energy is dissipated from the poloidal mode rather than rotating to the toroidal mode.

1159 **7.4 Ground Signatures and Giant Pulsations**

1160 While the majority of the action is in space, the majority of FLR observations have  
1161 historically been ground-based. The present section explores the same simulations dis-  
1162 cussed in Sections 7.2 and 7.3, but in terms of their ground signatures rather than their  
1163 broad energy distributions.

1164 As in the figures shown in Sections 7.2 and 7.3, each row in Figures 7.10 and 7.11 shows  
1165 runs at a different modenumber. The columns are magnetic field contours; the vertical  
1166 axis is latitude, and the horizontal axis is time. The four columns are components of  
1167 the magnetic field signatures at the ground: the north-south magnetic field (first and  
1168 third columns) and the east-west magnetic field (second and fourth columns). The pair  
1169 on the left show a simulation carried out using the active ionospheric profile, and the  
1170 pair on the right show a simulation using the quiet profile.

1171 Notably, the magnetic polarization of a low frequency Alfvén wave is rotated by  $\sim 90^\circ$  as  
1172 it passes through the ionosphere[41]. The east-west field on the ground ( $B_\phi$ ) corresponds  
1173 to the poloidal polarization in space, and the north-south field on the ground ( $B_\theta$ )  
1174 corresponds to the toroidal mode.

1175 The most striking feature of Figures 7.10 and 7.11 is the modenumber dependence.  
1176 As modenumber increases, the magnetic field signatures become sharply localized in  
1177 latitude. At high  $m$ , ground signatures are concentrated between  $60^\circ$  and  $70^\circ$ , peaking  
1178 near  $65^\circ$ , roughly coincident with the foot point of the  $L = 5$  field line.

1179 **TODO:** Is it weird that we see no ducting from the ionosphere? Does the ionosphere  
1180 duct ULF waves in the  $\theta$  direction, or just in  $\phi$ ?

1181 At low modenumber, magnetic signatures are weak on the ground because the waves  
1182 in space are also weak. At high modenumber, waves in space are strong, but so is  
1183 the attenuation of magnetic signatures by the ionosphere<sup>3</sup>. The “sweet spot” at which  
1184 magnetic ground signatures are maximized falls at  $m = 16$  to  $m = 32$ .

1185 Tuna shows stronger ground signatures on the dayside than on the nightside, more or  
1186 less in proportion with the difference in magnitude in space. Energy on the dayside

---

3See Equation (3.3).

1187 (which depends on field magnitude squared) peaks an order of magnitude larger than  
1188 that on the nightside. Peak ground signatures on the dayside are larger by a factor of  
1189 five: 45 nT compared to 10 nT. On both the dayside and the nightside, peak ground  
1190 signatures are in  $B_\phi$ , the east-west magnetic field component; both are also at  $m = 16$ ,  
1191 and both are seen in runs using the ionospheric profile for quiet solar activity.

1192 It's further notable that the ground signatures — particularly those on the nightside  
1193 — exhibit a change in chirality based on latitude. At low latitude,  $B_\theta$  leads  $B_\phi$ , which  
1194 creates a counterclockwise signature on the ground (in the northern hemisphere). At  
1195 high latitude, the phase is reversed, resulting in a clockwise ground signature.

1196 These results match well with observations of giant pulsations, which tend to be east-  
1197 west polarized, have a latitude-dependent chirality, and are most often observed near  
1198  $66^\circ$ , with azimuthal modenumbers of 16 to 35, at the bottom of the solar cycle[93]. Pgs  
1199 are most commonly observed pre-dawn, but dawn and dusk ionospheric profiles are not  
1200 implemented for Tuna at present.

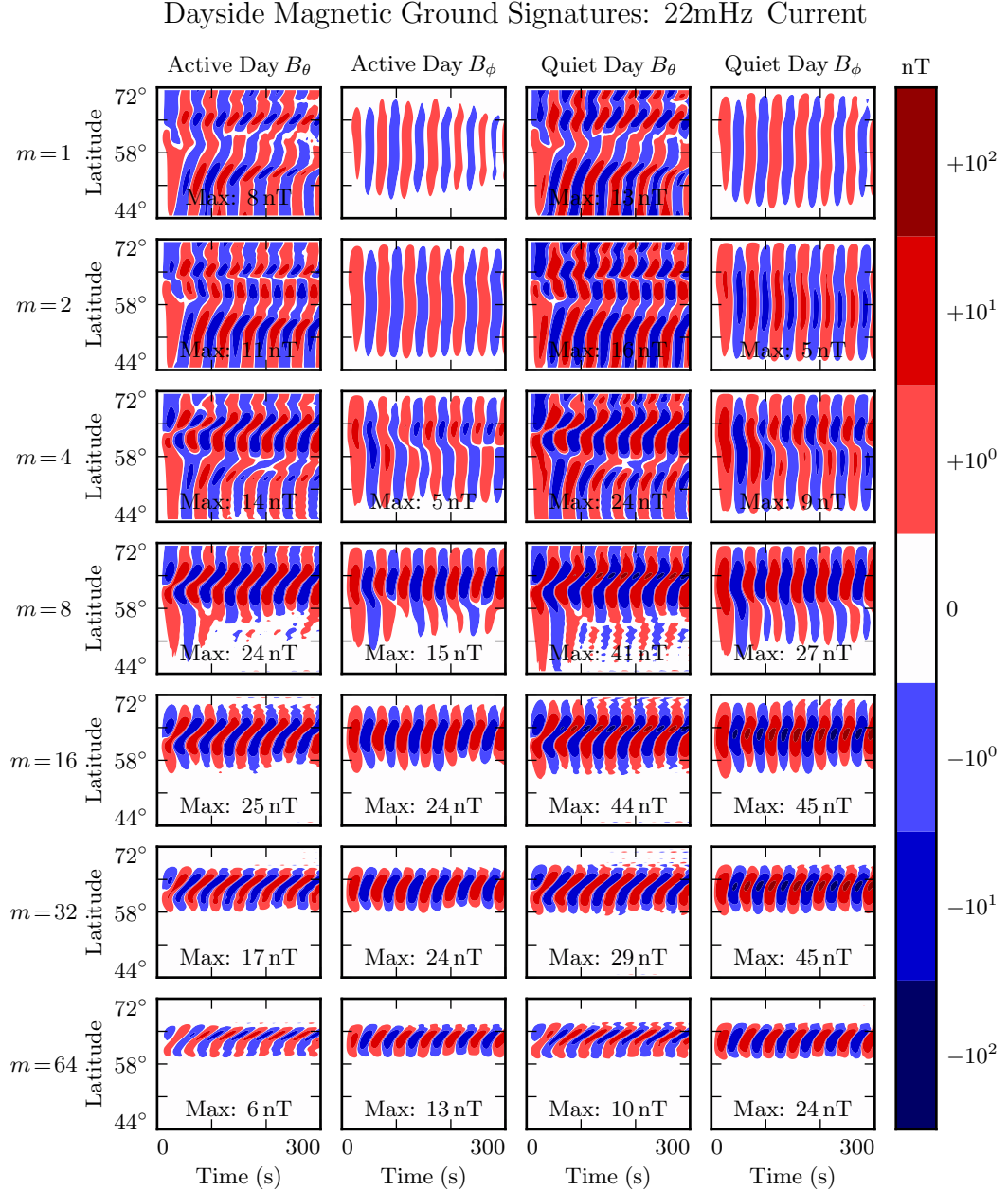


Figure 7.10: The magnetic ground signatures are shown for fourteen runs, two per row. Azimuthal modenumber is constant across each row. Polarization and ionospheric profile vary by column, per the headers. Ground signatures at low modenumber are not particularly strong because the waves in space are weak, while those at high modenumber are attenuated by the atmosphere. The “sweet spot” seems to fall around  $m = 16$  to  $m = 32$ . Peak amplitudes above 3 nT are marked.

### Nightside Magnetic Ground Signatures: 13mHz Current

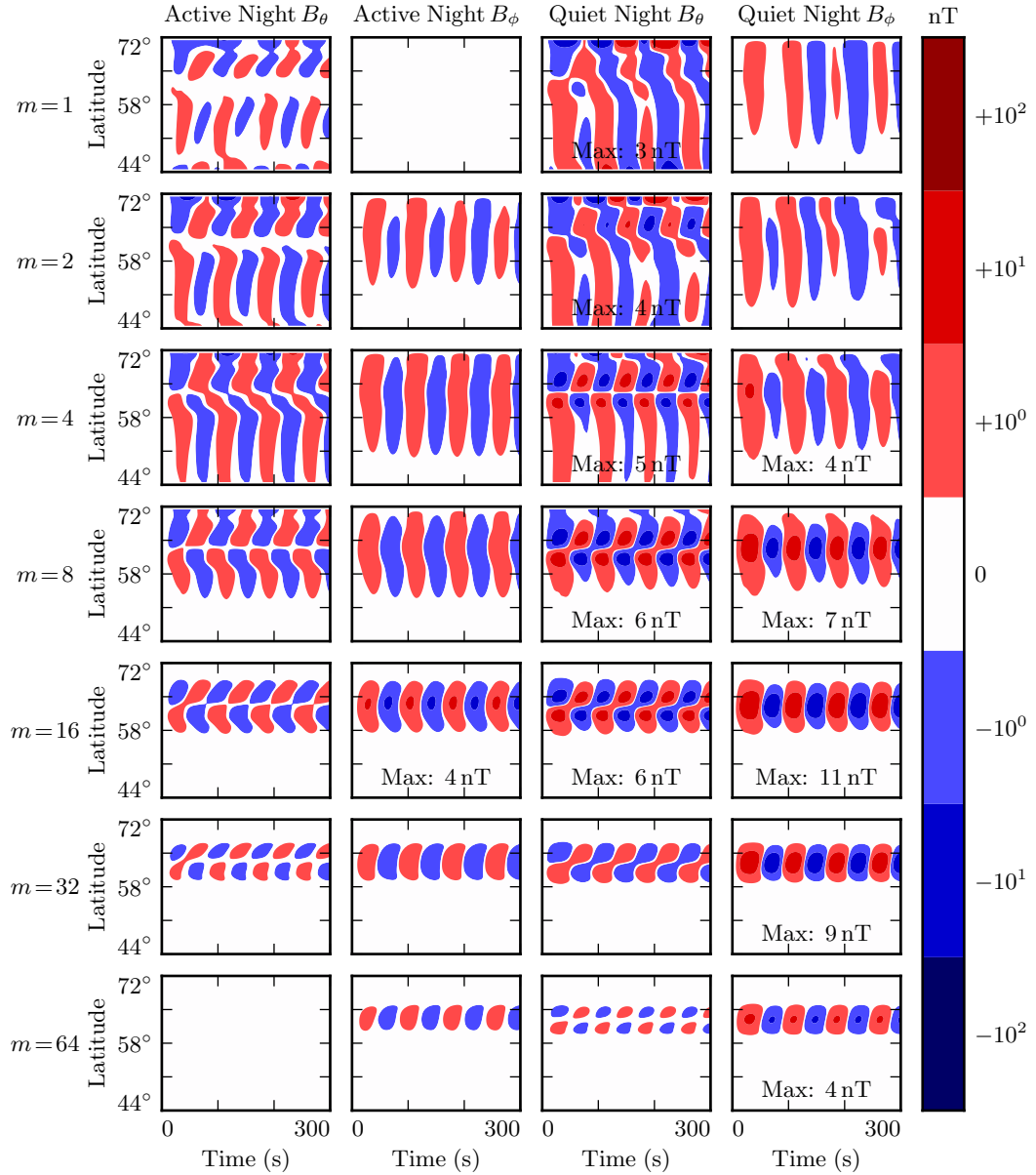


Figure 7.11: Nightside ground signatures are less strongly peaked than those on the dayside, but qualitative features are the same: the strongest signals are in  $B_\phi$ , peaked over just a few degrees in latitude, at a modenumber of 16 or 32, under quiet ionospheric conditions.

1201 **7.5 Discussion**

1202 **TODO:** Make this section read nicely.

1203 Poloidal FLRs rotate to the toroidal mode over time. Toroidal modes do not appear to  
1204 rotate back to the poloidal mode. When  $m$  is small, the rotation is comparable to an  
1205 oscillation period; when  $m$  is large, rotation timescales are comparable to ten periods,  
1206 sometimes more.

1207 On the dayside, little damping takes place over rotation timescales, so the toroidal mode  
1208 asymptotically exceeds the toroidal mode. The exception is waves with low modenumber,  
1209 where poloidal waves can escape by propagating across field lines. An evaluation  
1210 of what happens then — whether they bounce back off the magnetopause, for example  
1211 — is beyond the scope of the present work.

1212 On the nightside, the conductivity of the ionosphere is low enough that damping  
1213 timescales become comparable to oscillation timescales. Waves are weaker, since they  
1214 are unable to accumulate energy over as many periods. High- $m$  toroidal waves are  
1215 particularly weak, since the dissipation timescale is faster than the poloidal-to-toroidal  
1216 rotation timescale.

1217 Waves resonate best when the frequency of the driving matches the local eigenfrequency  
1218 where it's delivered. The eigenfrequency is significantly affected by the size of the  
1219 plasmasphere.

1220 The poloidal mode, due to its compressional character, exhibits an energy profile which  
1221 is smeared in  $L$ . The toroidal mode, on the other hand, forms sharp resonances where the  
1222 drive frequency matches the local eigenfrequency. This may explain why the observed  
1223 frequencies of poloidal waves depend weakly on  $L$ , while the frequencies of toroidal  
1224 waves are strongly dependent on  $L$ .

1225 At low  $m$ , ground signatures are weak because waves in space are weak because energy  
1226 can easily escape through the simulation's outer boundary. At large  $m$ , ground signatures  
1227 are attenuated by the ionosphere. The “sweet spot” in azimuthal modenumber at  
1228 which ground signatures are strongest is around 16 to 32. Furthermore, ground signatures  
1229 are strongest when ionospheric profiles corresponding to solar minimum are used.

1230 Driving in the poloidal electric field gives rise to primarily ground signatures polarized  
1231 primarily in the east-west direction at the ground. And, when the frequency of the  
1232 driving does not match the local eigenfrequency, the high- $m$  resonates weakly in place,  
1233 rather than tunneling across field lines to resonate strongly somewhere else.

1234 These findings imply, awkwardly, that the morphology of giant pulsations may reveal  
1235 relatively little about their origins. One can consider a hypothetical magnetosphere  
1236 subject to constant driving: broadband in frequency, broadband in modenumber, just  
1237 outside the plasmapause. Low- $m$  poloidal waves will quickly rotate to the toroidal mode  
1238 (and/or propagate away). High- $m$  waves will resonate in place, accumulating energy  
1239 over time, and giving rise to “multiharmonic toroidal waves”[89]; Fourier components  
1240 that do not match the local eigenfrequency will quickly asymptote. Waves with very high  
1241 modenumbers will be attenuated by the ionosphere. The response on the ground will be  
1242 significantly stronger during quiet solar conditions. In other words, the measurements  
1243 on the ground will look very much like a giant pulsation.

1244 **TODO:** Notably, the present work offers no explanation as to Pgs’ distinctive distribu-  
1245 tion in MLT!

<sub>1246</sub> **Chapter 8**

<sub>1247</sub> **Van Allen Probe Observations**

<sub>1248</sub> The results presented in Chapter 7 are interesting on their own, but become particularly  
<sub>1249</sub> valuable when combined with observational data. Unfortunately, only a small number  
<sub>1250</sub> of studies to date have explored how Pc4 observation rate is affected by the harmonic  
<sub>1251</sub> and polarization structure of those waves.

<sub>1252</sub> While Pc4 pulsations have previously been studied in terms of both harmonic[4, 14, 26,  
<sub>1253</sub> 44, 83, 92] and polarization[2, 16, 17, 53, 57], little work has considered both at the  
<sub>1254</sub> same time. This has largely been due to observational constraints. The classification of  
<sub>1255</sub> a wave’s harmonic is best carried out by computing the phase offset of the magnetic and  
<sub>1256</sub> electric field waveforms, simultaneous in situ measurements of which have only recently  
<sub>1257</sub> become available as part of the THEMIS[3] and Van Allen Probe[86] missions. The  
<sub>1258</sub> Van Allen Probes (launched in 2012) are particularly well-suited to the study of Pc4  
<sub>1259</sub> pulsations as their apogee of  $L \sim 6$  coincides closely with eigenfrequencies in the Pc4  
<sub>1260</sub> range.

<sub>1261</sub> The present chapter uses data from the Van Allen Probes’ EFW instrument[102] to  
<sub>1262</sub> survey the occurrence rate of FLRs in the Pc4 range as a function of harmonic parity  
<sub>1263</sub> and polarization, as well as magnitude, frequency, and phase. The tools used to perform  
<sub>1264</sub> the present analysis — SPEDAS and the SPICE kernel — are publicly available. They,  
<sub>1265</sub> along with the Python routines used to download, filter, and plot the data, can be found  
<sub>1266</sub> in a Git repository at <https://github.com/chizarlicious/RBSP>.

1267 TODO: Set this up, along with Tuna, at <https://github.com/UMN-Space-Physics>.

## 1268 8.1 Sampling Bias and Event Selection

1269 The present analysis makes use of Van Allen Probe data from October 2012 to August  
1270 2015 — the entire range available at the time of writing. Between the two probes, that's  
1271 just over 2000 days of observation.

1272 For the purposes of Pc4 pulsations, it's reasonable to consider the two probes to be  
1273 independent observers. Nearly all Pc4 events occur near apogee ( $L \gtrsim 5$ ), at which  
1274 point the two probes are several hours apart in MLT. Pc4 events are typically not large  
1275 enough to be seen by both probes simultaneously, and not long enough in duration to  
1276 be seen by two probes passing through the same region of space several hours apart.

1277 TODO: Quantify how often an event is seen by both probes?

1278 Electric and magnetic field waveforms are collected using the probes' EFW and EMFISIS  
1279 instruments respectively. Values are cleaned up by averaging over the ten-second spin  
1280 period. Three-dimensional electric field data is then obtained using the  $\underline{E} \cdot \underline{B} = 0$   
1281 assumption. Notably, this assumption is taken only when the probe's spin plane is  
1282 offset from the magnetic field by at least  $15^\circ$ . The rest of the data — about half — is  
1283 discarded, which introduces a sampling bias against the flanks.

1284 A further bias is introduced by the probes' non-integer number of precessions around  
1285 Earth. As of July 2014, apogee had precessed once around Earth[16]. The present work  
1286 considers roughly one and a half precessions; the nightside has been sampled at apogee  
1287 twice as often as the dayside.

1288 The spatial distribution of usable data — that is, data for which three-dimensional  
1289 electric and magnetic fields are available — is shown in Figure 8.1. Bins are unitary in  
1290  $L$  and in MLT. Distribution in magnetic latitude is not shown; the Van Allen Probes  
1291 are localized to within  $\sim 10^\circ$  of the equatorial plane.

1292 Field measurements are transformed from GSE coordinates into the same dipole coordi-  
1293 nates used in Chapters 5 and 7. The  $z$  axis (parallel to the background magnetic field)

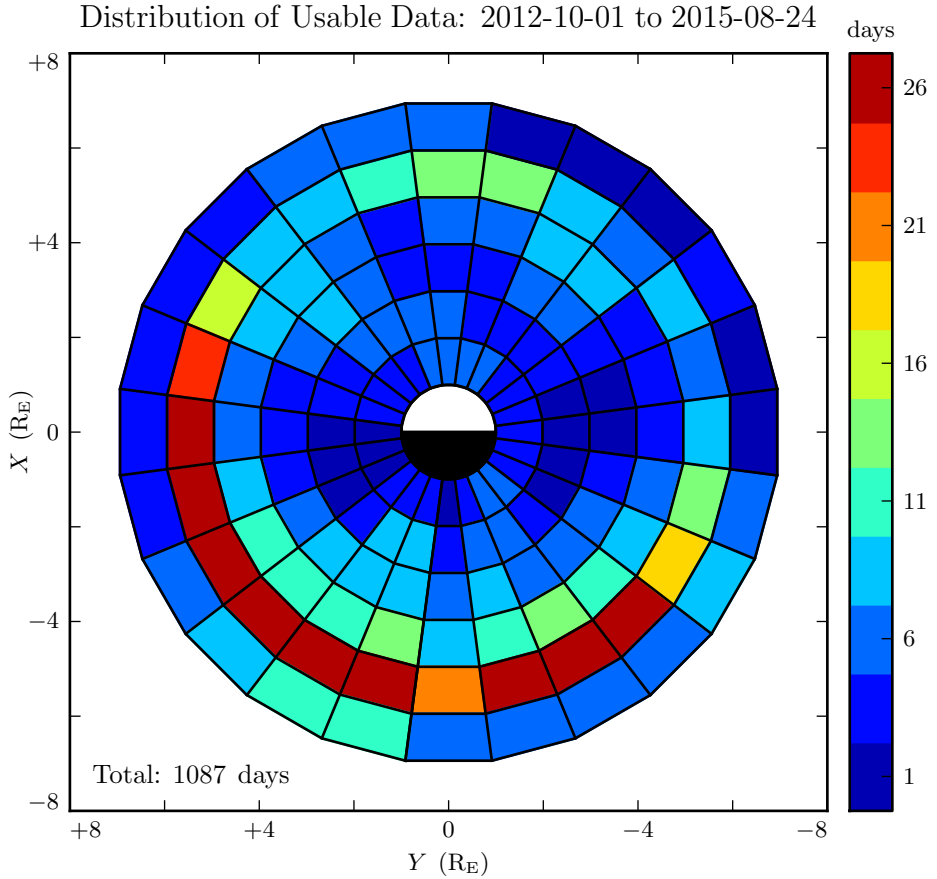


Figure 8.1: Three-dimensional electric field values are computed by assuming  $\underline{E} \cdot \underline{B} = 0$ . Data is discarded whenever the magnetic field falls within  $15^\circ$  of the spin plane, which introduces a bias against the flanks. Furthermore, the probes have completed one and a half precessions around Earth; the dayside has been sampled once at apogee, and the nightside twice.

- 1294 is estimated using a ten-minute running average of the magnetic field measurements.
- 1295 The  $y$  axis is set parallel to  $\hat{z} \times \underline{r}$ , where  $\underline{r}$  is the probe's geocentric position vector.
- 1296 The  $x$  axis is then defined per  $\hat{x} \equiv \hat{y} \times \hat{z}$ . This scheme guarantees that the axes are
- 1297 right-handed and pairwise orthogonal[57].
- 1298 The  $\sim 1000$  days of usable data are considered half an hour at a time, which gives a fre-
- 1299 quency resolution of  $\sim 0.5$  mHz in the discrete Fourier transform. Spectra are computed

1300 for all six field components:  $\tilde{B}_x$ ,  $\tilde{B}_y$ ,  $\tilde{B}_z$ ,  $\tilde{E}_x$ ,  $\tilde{E}_y$ , and  $\tilde{E}_z$ . The background magnetic  
 1301 field is subtracted before transforming the magnetic field components, leaving only the  
 1302 perturbation along each axis<sup>1</sup>. Each waveform is also shifted vertically so that its mean  
 1303 over the thirty minute event is zero.

Frequency-domain Poynting flux is computed from the electric and magnetic field transforms. A factor of  $L^3$  compensates the compression of the flux tube, so that the resulting values are effective at the ionosphere. Poloidal and toroidal Poynting flux, respectively, are given by:

$$\tilde{S}_P \equiv -\frac{L^3}{\mu_0} \tilde{E}_y \tilde{B}_x^* \quad \tilde{S}_T \equiv \frac{L^3}{\mu_0} \tilde{E}_x \tilde{B}_y^* \quad (8.1)$$

1304 The poloidal and toroidal channels are independently checked for Pc4 waves. For each  
 1305 channel, a Gaussian profile is fit to the magnitude of the Poynting flux,  $|\tilde{S}(\omega)|$ . If the  
 1306 fit fails to converge, or if the peak of the Gaussian does not fall within 5 mHz of the  
 1307 peak value of  $\tilde{S}$ , the event is discarded. Events are also discarded if their frequencies  
 1308 fall outside the Pc4 frequency range (7 mHz to 25 mHz) or if their amplitudes fall below  
 1309  $10^{-2}$  mW/m<sup>2</sup> (out of consideration for instrument sensitivity).

1310 Events are discarded if their parity is ambiguous. The electric field and the magnetic  
 1311 field must be coherent at a level of 0.9 or better (judged at the discrete Fourier transform  
 1312 point closest to the peak of the Gaussian fit). Any event within 3° of the magnetic  
 1313 equator is also not used; as discussed in Chapter 3, in order to distinguish an odd mode  
 1314 from an even mode, it's necessary to know whether the observation is made north or  
 1315 south of the equator.

1316 **TODO: How much time do the probes spend within 3° of the magnetic equator?**

1317 A visual inspection of events shows that those with broad “peaks” in their spectra  
 1318 are typically not peaked at all — they are noisy spectra with several spectral features  
 1319 grouped just closely enough to trick the fitting routine. A threshold is set at a FWHM

---

<sup>1</sup>As in Chapters 5 and 7,  $B_x$ , refers not to the full magnetic field in the  $x$  direction, but to the perturbation in the  $x$  direction from the zeroth-order magnetic field. The same is true for  $B_y$  and  $B_z$ .

1320 of 3 mHz (equally, a standard deviation of 1.27 mHz). Any event with a Gaussian fit  
1321 broader than that is discarded.

1322 Notably, events are not filtered on their phase — that is, on the division of their energy  
1323 between standing and traveling waves. This is the topic of Section 8.5.

1324 **TODO: Are we biased in terms of DST? What's the distribution look like for the good**  
1325 **data and for the bad data?**

## 1326 8.2 Events by Mode

1327 The filters described in Section 8.1 yield 762 Pc4 events, the spatial distribution of  
1328 which is shown in Figure 8.2. In each bin, the event count is normalized to the amount  
1329 of usable data, per Figure 8.1. Bins shown in white contain zero events. The rate in  
1330 the bottom corner is an overall mean, weighing each bin equally.

1331 Consistent with previous work, Pc4 events peak on the dayside and are rarely observed  
1332 at  $L < 4$ . Nearly 30 % of the usable data shown in Figure 8.1 is taken at  $L < 4$ , yet  
1333 only 16 of the 762 events appear there.

1334 On the other hand, the present work runs contrary to Dai's 2015 result in terms of Pc4  
1335 event rates with respect to the plasmapause (not shown). His analysis found (poloidal)  
1336 Pc4 pulsations to be comparably common inside and outside the plasmapause[16]. In  
1337 the present work, only 40 of the 762 events (5 %) fall inside the plasmasphere, despite  
1338 the fact that 40 % of the available data falls within the plasmasphere. The disparity is  
1339 not likely due to a difference in sampling — Dai's work, like the present work, uses data  
1340 from the Van Allen Probes mission. Rather, the difference is likely due to disagreement  
1341 in how the plasmapause is defined. Dai identifies the plasmapause by the maximum  
1342 gradient in electron number density, while the present work takes an electron density of  
1343  $100 \text{ /cm}^3$  to mark the plasmapause<sup>2</sup>.

1344 The same events in Figure 8.1 are shown again in Figure 8.3, partitioned by polarization  
1345 and parity.

---

<sup>2</sup>Per ongoing work by Thaller.

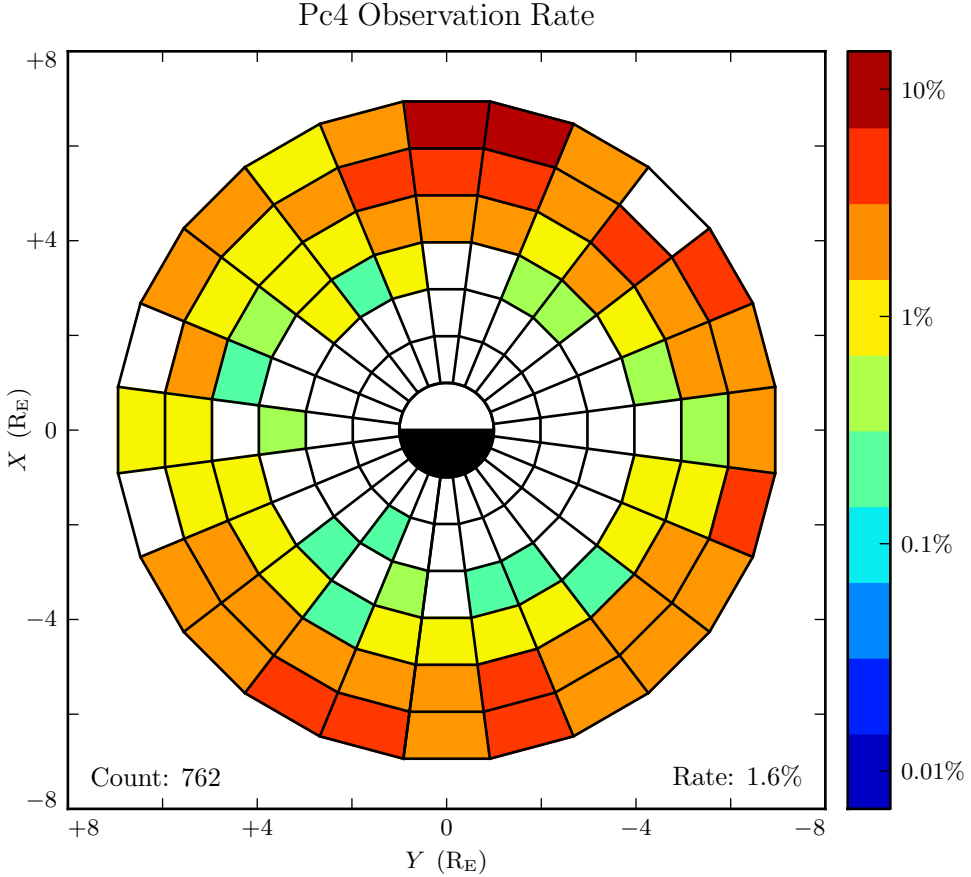


Figure 8.2: The above figure shows the spatial distribution of all 762 observed Pc4 events. Counts are normalized by the amount of usable data in each bin. The value in the bottom-right corner is the mean of the rate in each bin; it's an estimate of how often Pc4 events would be observed if the sampling were distributed uniformly in space. Events where the poloidal and toroidal channel trigger simultaneously ( $\sim 10\%$  of cases) are counted as only a single event. Bins shown in white contain zero events.

1346 The distribution of even poloidal events in Figure 8.3 is consistent with that reported  
 1347 by Dai[16]: the observation rate is peaked at noon, and smeared across the dusk side.  
 1348 Notably, Dai's work focused on even poloidal waves. While he did not explicitly remove  
 1349 odd events from his sample, he did introduce a threshold in the magnetic field. This  
 1350 threshold is preferentially satisfied by even waves (which have a magnetic field antinode  
 1351 near the equator) compared to odd waves (which have a magnetic field node). Dai

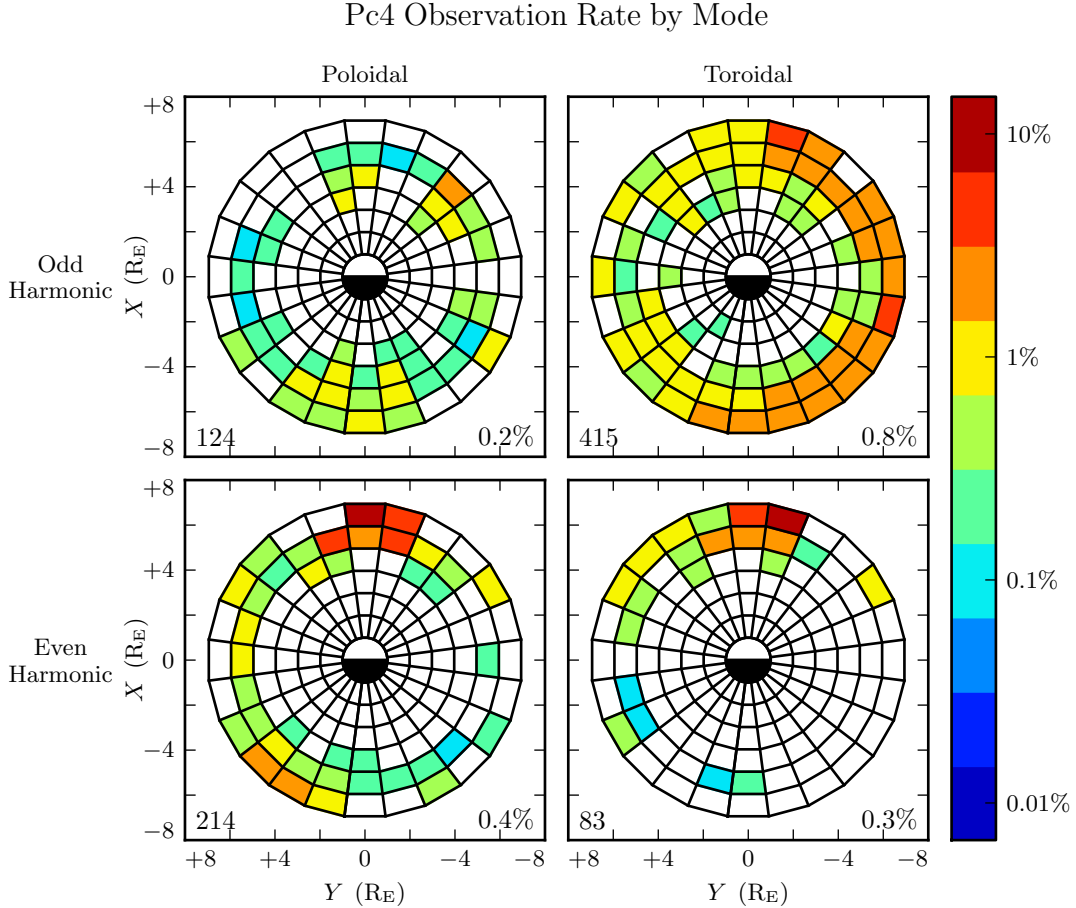


Figure 8.3: The above figure shows the spatial distribution for the same 762 events shown in Figure 8.2, partitioned by polarization and parity. The selection criteria described in Section 8.1 ensure that both properties are known for all events. Event counts are normalized by the time spent by the amount of usable data in each bin. Counts shown in the bottom-left corners do not sum to 762 because some events trigger on both the poloidal channel and the toroidal channel. Bins shown in white contain zero events.

characterized the parity of only a quarter of his events; among those, he found even harmonics to outnumber odd harmonics ten-to-one.<sup>1352</sup>

In fact — to the degree that they can be straightforwardly compared — the distributions in Figure 8.3 also show agreement with work by Anderson[2] (using AMPTE/CCE),<sup>1353</sup>

1356 Kokubun[53] (using ATS6), Liu[57] (using THEMIS), and Motoba[70] (using GOES).  
1357 Toroidal events dominate overall, and are primarily seen on the morning side. Poloidal  
1358 events are spread broadly in MLT, with a peak near noon and distinctive odd harmonics  
1359 in the early morning.

1360 Crucially, the present work can offer insight into how previous results fit together. Unlike  
1361 events considered in previous works, those shown in Figure 8.3 have all been categorized  
1362 in terms of both polarization and parity. And, perhaps more importantly, the selection  
1363 process has not introduced a bias with respect to polarization or parity (at least not an  
1364 obvious one).

1365 The even events shown in Figure 8.3 show good agreement with the numerical results  
1366 in Chapter 7. The distributions are qualitatively similar, as might be expected if even  
1367 poloidal waves served as a source for even toroidal waves. Even poloidal waves are more  
1368 prevalent, suggesting a typical event duration comparable to the poloidal-to-toroidal  
1369 rotation timescale. And even toroidal events are skewed dayward compared to even  
1370 poloidal events, suggesting that poloidal-to-toroidal rotation is inhibited by increased  
1371 Joule dissipation on the nightside.

1372 The same can be said to some extent for the odd events in Figure 8.3, though the trends  
1373 are less strong. Odd poloidal and odd toroidal events are both scarce on the dusk flank.  
1374 On the dawn flank, poloidal events skew nightward, while toroidal events are spread  
1375 broadly — that is, they are skewed dayward compared to the poloidal events. However,  
1376 it's unclear why odd toroidal events outnumber odd poloidal events to such a degree.

1377 **TODO:** Conventional explanation for dawn-dusk asymmetry.

1378 When the 762 events are broken down by mode in Figure 8.3, the result is 124 odd  
1379 poloidal events, 214 even poloidal events, 415 odd toroidal events, and 83 even toroidal  
1380 events — a total of 836 events. The total is greater than 762 because in  $\sim$ 10 % of  
1381 events, the poloidal and toroidal channels trigger independently. Such cases are marked  
1382 as a single event in Figure 8.2, but the toroidal and poloidal events are both shown in  
1383 Figure 8.3.

1384 Double-triggering can be taken as a vague proxy for event quality. When the channels  
1385 both trigger independently, the two events almost always (71 of 74 events) exhibit the

1386 same parity. This suggests a poloidal wave with sufficient power, and a sufficient narrow  
 1387 spectral peak, that it can still be seen after much of its energy has rotated to the toroidal  
 1388 mode.

### Rate of Double Events by Parity and Storm Index

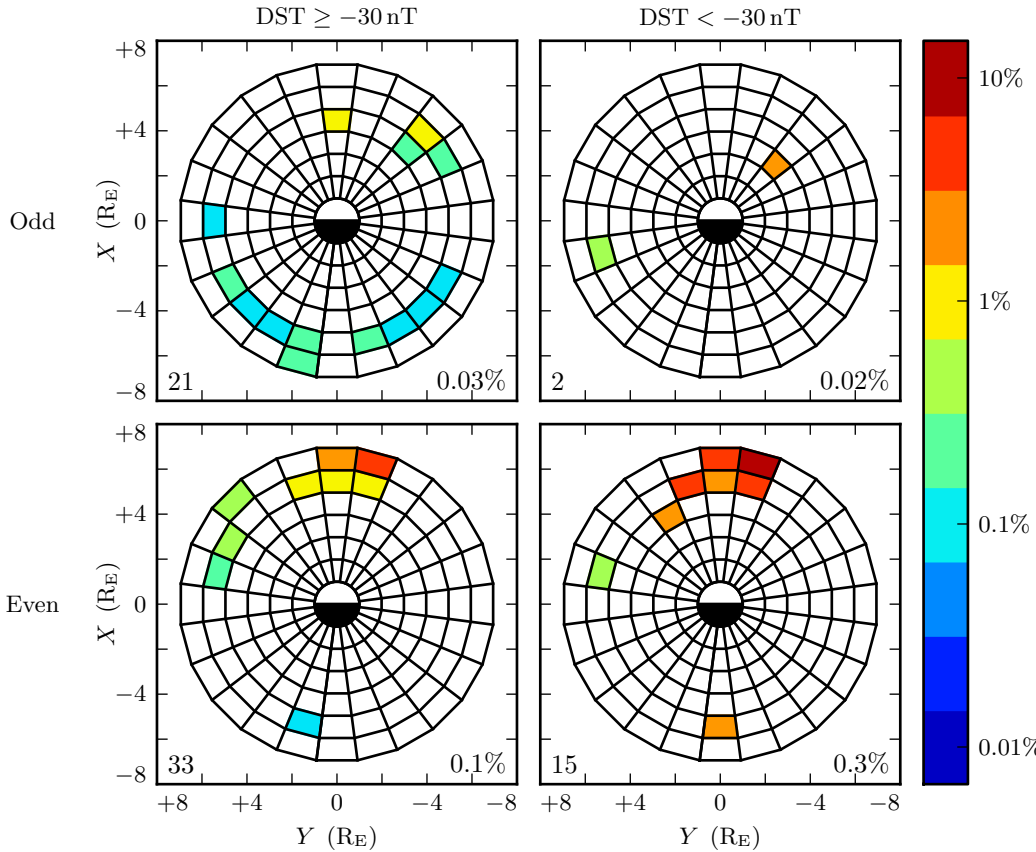


Figure 8.4: A double event is a simultaneous triggering of the poloidal and toroidal channels on the same probe. In such cases, the two channels almost always exhibit the same parity. Double events serve as a vague proxy for event quality — a poloidal event with sufficient strength and clarity to be seen even after much of its energy has rotated to the toroidal mode. Odd double events are spread broadly; even events are concentrated near noon, and become more common during geomagnetically active times.

1389 The spatial distribution of double events is shown in Figure 8.4. The left column shows  
 1390 events observed with  $DST \geq -30$  nT, normalized by the amount of usable data at

1391 DST  $\geq -30$  nT. The right column shows events at DST  $< -30$  nT, normalized by the  
1392 amount of data with DST  $< -30$  nT.

1393 Odd double-triggering events are spread broadly in MLT. They rarely occur twice on  
1394 the same day; the 23 events shown take place over 20 different dates. Odd double events  
1395 occur at similar rates regardless of DST.

1396 Even-harmonic double-triggering events, on the other hand, are mostly seen near noon,  
1397 and are significantly more common during geomagnetically active times. Even events  
1398 are also more concentrated than odd ones. The 48 even-harmonic double-events shown  
1399 in the bottom row of Figure 8.4 are spread over 20 days, and 35 of them are spread over  
1400 just 7 days. This clustering — where the poloidal and toroidal channel both trigger for  
1401 five to ten half-hour events in the same day — is prevalent regardless of DST.

### 1402 8.3 Events by Amplitude

1403 One might reasonable be concerned that the spatial distributions presented in Figure 8.3  
1404 are dominated by these small events, while Pc4 events large enough to be noteworthy  
1405 follow a different distribution entirely. The goal of the present section is to address that  
1406 concern.

1407 The distribution of event magnitudes is presented in Figure 8.5, graded based on the  
1408 peak of the Gaussian fit of each event's Poynting flux,  $|\tilde{S}(\omega)|$ . Mean and median  
1409 values are listed for each mode. Most events are small, with Poynting flux well below  
1410  $0.1 \text{ mW/m}^2$  when mapped to the ionosphere. Only a handful of events — 3 out of 762  
1411 — exceed  $1 \text{ mW/m}^2$ , typically taken to be the threshold at which visible auroral arcs  
1412 form. One such event is shown in Figure 8.6.

1413 TODO: Say something about this event? Not really clear what purpose is served by this  
1414 example, actually. As a matter of curiosity, the apparent wave activity in the toroidal  
1415 channel did not pass the event selection trigger because the electric and magnetic wave-  
1416 forms are not coherent.

Amplitude Distribution of Pc4 Events by Mode

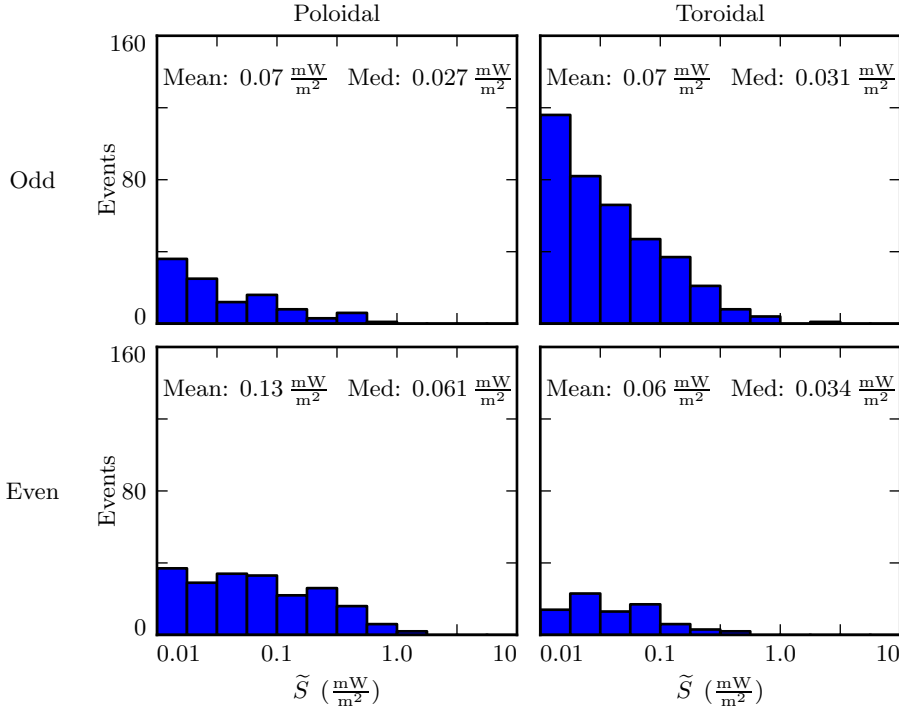


Figure 8.5: Amplitude distribution is shown for Pc4 events by parity and polarization, based on the peak of the spectrum's Gaussian fit. Odd poloidal events, odd toroidal events, and even toroidal events fall off sharply with increasing amplitude, while the even poloidal events are distributed more broadly — the mean and median of the even poloidal distribution is twice as large as that of the others.

1417 Perhaps the most notable feature of Figure 8.5 is the relative uniformity of the distri-  
 1418 bution of even poloidal events. If a higher magnitude threshold is imposed, as shown in  
 1419 Figure 8.7, the proportion of even poloidal events rises.

1420 The spatial bins in Figure 8.7 are larger than those in Section 8.2; this change reflects  
 1421 an effort to keep the number of events large compared to the number of bins, even when  
 1422 considering relatively small subsets of the data. The larger bins — two hours wide in  
 1423 MLT and divided at  $L = 5$  radially — are also used in Sections 8.4 and 8.5. All of the  
 1424 large-binned bullseye plots also share a common logarithmic color bar.

1425 All else being equal, one might expect the amplitude distribution of even toroidal modes  
1426 to mimic that of even poloidal modes, since poloidal waves asymptotically rotate to  
1427 toroidal waves. However, this does not seem to be the case. The mean and median  
1428 magnitudes are more or less consistent for even toroidal modes, odd toroidal modes,  
1429 and odd poloidal modes, while even poloidal modes are twice as large by those metrics.  
1430 This would seem to imply that large even poloidal modes have disproportionately high  
1431 modenumbers, and thus deliver energy to the toroidal mode less efficiently. This expla-  
1432 nation is also unsatisfying, however; Figure 8.7 shows that even poloidal and toroidal  
1433 modes both become more concentrated near noon at high amplitude, suggesting a com-  
1434 mon origin.

### Waveforms and Spectra: Odd Poloidal Wave

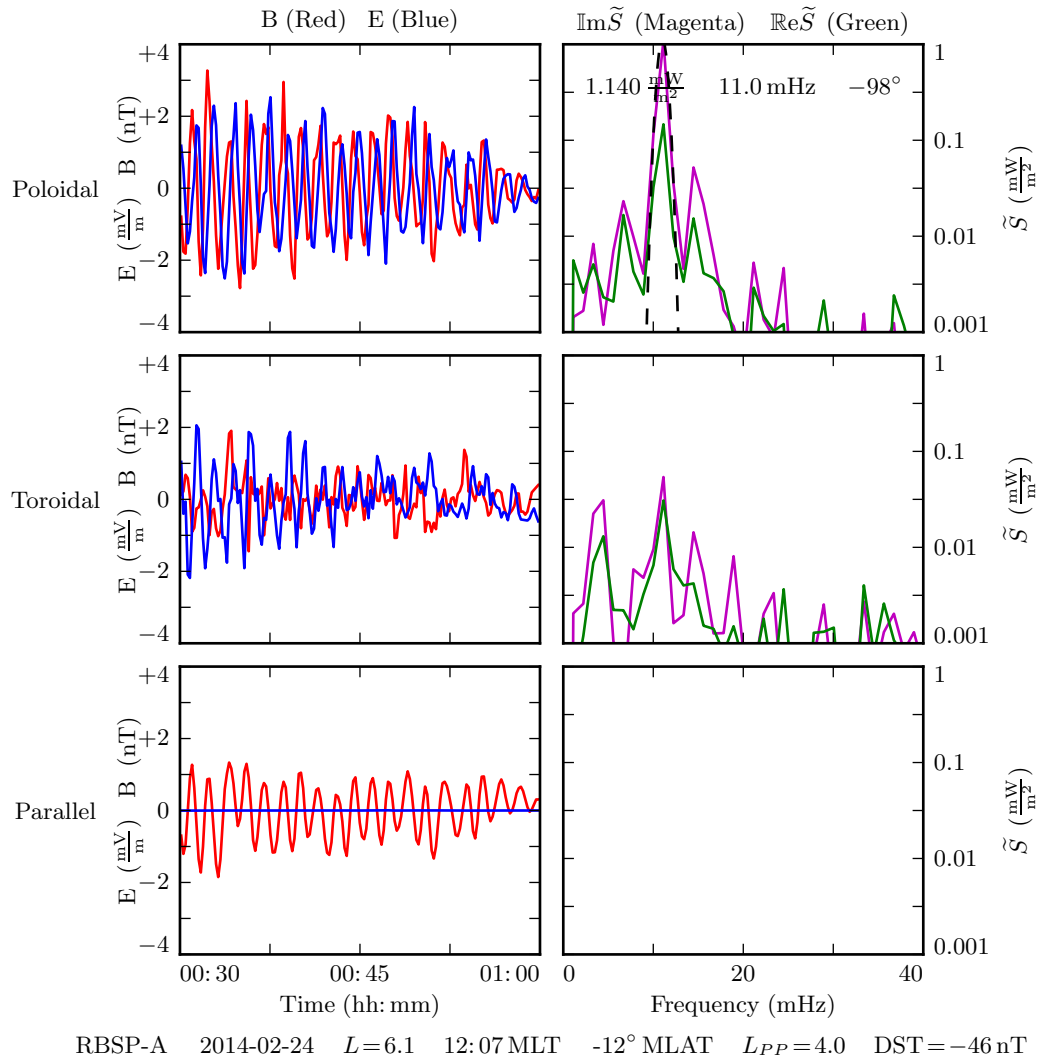


Figure 8.6: **TODO:** ...

### Distribution of Pc4 Events by Mode and Amplitude

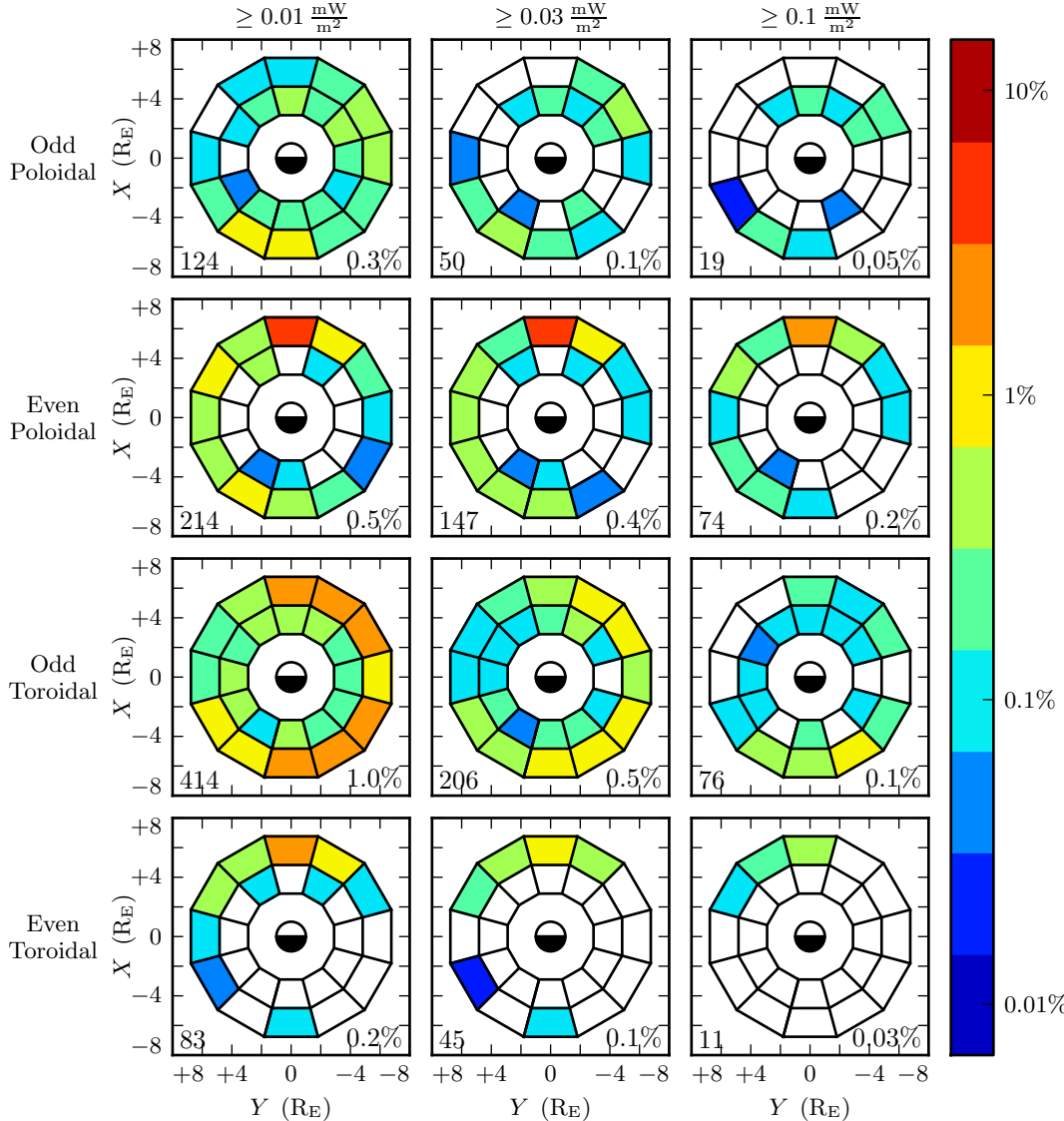


Figure 8.7: The above figure shows the distribution of Pc4 event observations by mode. Event magnitude cutoff is constant down each column, and increases from left to right. Stronger even events appear to become more concentrated on the dayside as the amplitude increases. Even poloidal events also become significantly more numerous relative to the other three modes, from 26 % at a cutoff of  $0.01 \text{ mW/m}^2$  to 41 % at  $0.1 \text{ mW/m}^2$ .

## <sup>1435</sup> 8.4 Events by Frequency

<sup>1436</sup> The difference in magnetospheric conditions between the dayside and the nightside  
<sup>1437</sup> suggest that different eigenfrequencies should arise between dayside and nightside res-  
<sup>1438</sup> onances at the same  $L$ -shell. In fact, this phenomenon has been observed directly;  
<sup>1439</sup> the frequencies of azimuthally-drifting FLRs have been shown to change over time[70].  
<sup>1440</sup> The effect is attributed to the difference in mass loading (and thus Alfvén speed) as a  
<sup>1441</sup> function of MLT.

<sup>1442</sup> This effect was furthermore apparent in the numerical results shown in Chapter 7, where  
<sup>1443</sup> Alfvén speeds on the dayside (based on empirical profiles) gave rise to significantly higher  
<sup>1444</sup> eigenfrequencies than those on the nightside.

<sup>1445</sup> In Figure 8.8, events at 11 mHz to 17 mHz (center column) do seem to be shifted night-  
<sup>1446</sup> ward compared to those at 7 mHz to 11 mHz (left column), but the effect is far more  
<sup>1447</sup> pronounced than what is suggested by Sections 7.2 and 7.3.

<sup>1448</sup> **TODO:** We should show the runs driven at  $L \sim 5$  across the board. Dayside and  
<sup>1449</sup> nightside. That way we can make a fair comparison.

<sup>1450</sup> As might be expected, even events are more prevalent than first-harmonic-dominated  
<sup>1451</sup> odd events higher in the Pc4 range. Events at 7 mHz to 11 mHz (left column) outnumber  
<sup>1452</sup> those at 17 mHz to 25 mHz (right column) ten-to-one or more for odd events. Among  
<sup>1453</sup> even events, the comparison is closer to three-to-one.

<sup>1454</sup> The spatial distribution of odd toroidal events above 17 mHz warrants specific consid-  
<sup>1455</sup> eration. Whereas odd toroidal events overall show an overwhelming preference for the  
<sup>1456</sup> morning side, those at the top of the Pc4 frequency band instead appear from noon  
<sup>1457</sup> to dusk. It's possible that this distribution is a consequence of the small number of  
<sup>1458</sup> events (25). More likely, however, is that these are third-harmonic events, and that  
<sup>1459</sup> their source more closely resembles the source for second-harmonic waves than it does  
<sup>1460</sup> first-harmonics.

<sup>1461</sup> **TODO:** Have people looked at third harmonics?

<sup>1462</sup> The frequency distribution for each mode is shown in Figure 8.9. The most distinctive  
<sup>1463</sup> feature, certainly, is the frequency peak in the odd toroidal mode near 9 mHz. This is  
<sup>1464</sup> in line with the idea that toroidal waves exhibit frequencies that depend sharply on  $L$ ,  
<sup>1465</sup> as discussed in Chapter 7. While the Van Allen Probes' orbits do cover a large range of  
<sup>1466</sup>  $L$ -shells, their observations (and thus the selected events) are concentrated near apogee  
<sup>1467</sup> at  $L \sim 6$ .

<sup>1468</sup> TODO: Maybe put the Gaussian fit back on top of these distributions? The distributions  
<sup>1469</sup> are not particularly Gaussian, but it gives a quantitative estimate of the spread.

### Distribution of Pc4 Events by Mode and Frequency

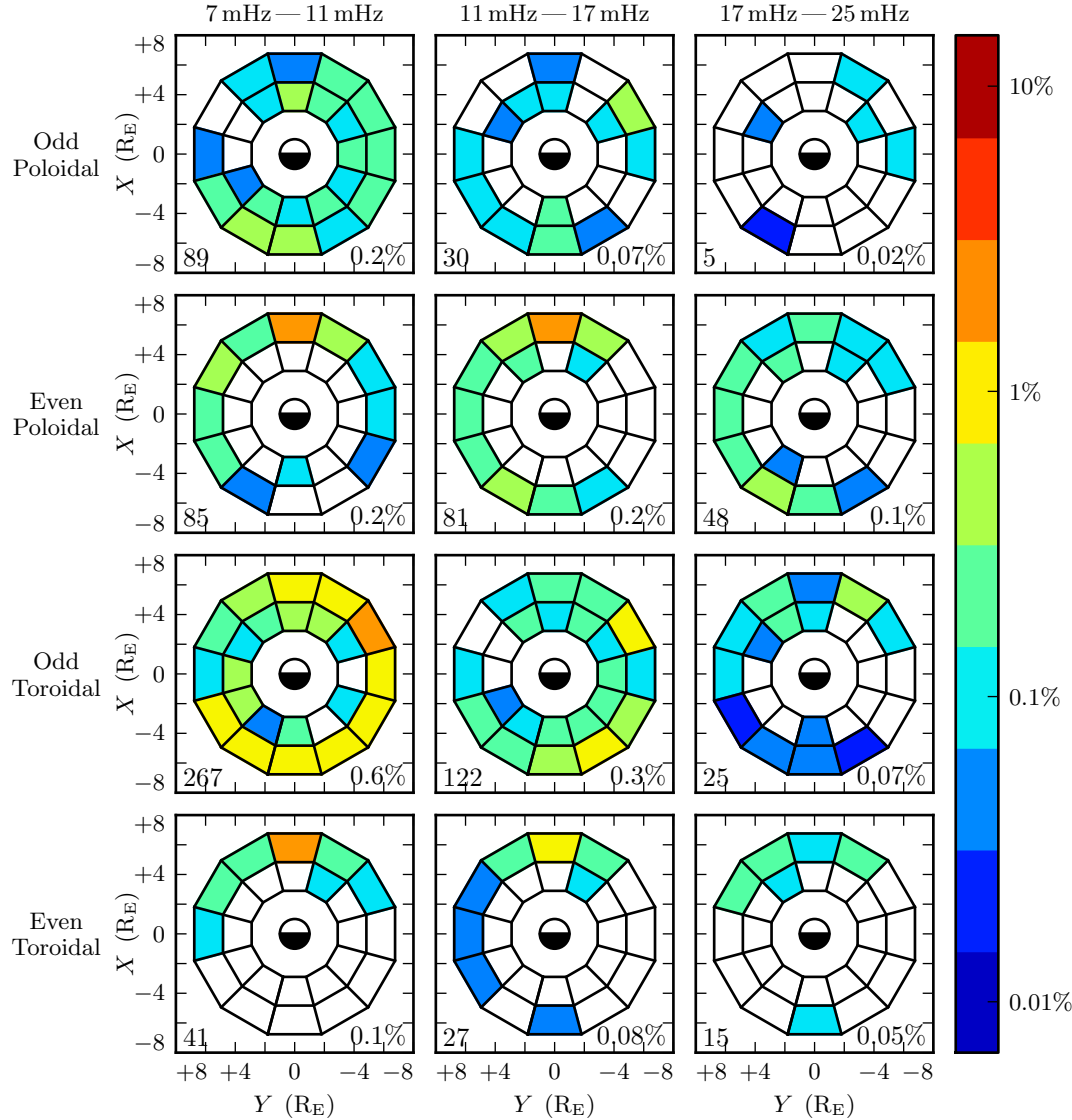


Figure 8.8: Event distributions above are shown in terms of mode (row) as well as event frequency (column). Mid-frequency Pc4 events are shifted somewhat nightward compared to low-frequency Pc4 events, as might be expected from the dayside's faster Alfvén speed. At the top of the Pc4 band, the distribution of odd toroidal events takes on a decidedly different character; this is likely because they are third harmonics rather than first harmonics.

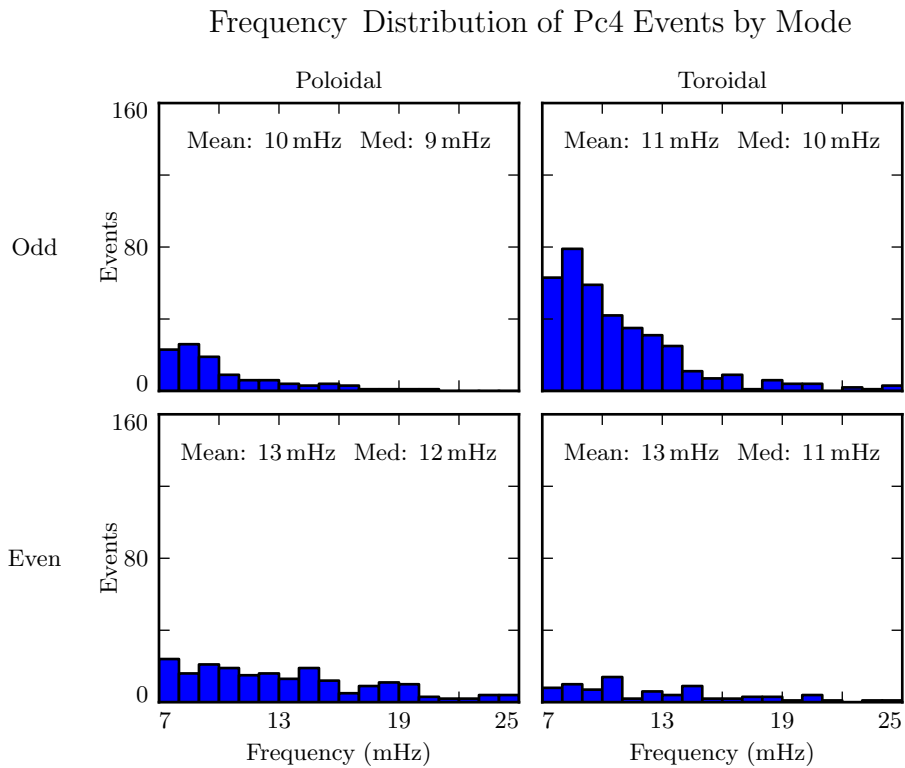


Figure 8.9: Frequency distributions are shown for all events, divided by harmonic and polarization. Odd toroidal events exhibit a particularly sharp peak in frequency, which is consistent with the toroidal mode's strong correlation with the local eigenfrequency. Poloidal modes appear more spread out in frequency, which is also consistent with past observations and with the numerical results in Chapter 7.

## 1470 8.5 Events by Phase

1471 The phase of a wave — that is, the phase offset between a wave's electric and magnetic  
1472 fields — indicates how its energy is partitioned between the standing and traveling  
1473 wave modes. An ideal standing wave has a phase of  $\pm 90^\circ$ , and thus its Poynting flux is  
1474 completely imaginary. A traveling wave, on the other hand, has electric and magnetic  
1475 fields in phase (or in antiphase), and is associated with a net movement of energy,  
1476 usually toward the ionosphere.

1477 Wave phase is a topic of significant interest, since it allows an estimate to be made of  
1478 the wave's lifetime. And, because phase can only be determined using simultaneous  
1479 electric and magnetic field measurements, it has only recently become observable.

1480 **TODO: Do people really care about phase, or is it just John?**

The energy per unit volume, and the rate at which energy is carried out of that volume  
by Poynting flux, are respectively given by:

$$U = \frac{R^3}{2\mu_0} B^2 \quad \frac{\partial}{\partial t} U = \frac{R^2}{\mu_0} EB \cos \varphi \quad (8.2)$$

1481 Where  $B$ ,  $E$ , and  $R$  are the characteristic magnetic field magnitude, electric field mag-  
1482 nitude, and length scale. The phase,  $\varphi \equiv \arctan \frac{\text{Im}S}{\text{Re}S}$ , enters because only real Poynting  
1483 flux carries energy.

The ratio of the two quantities in Equation (8.2) gives a characteristic timescale over  
which energy leaves the system

$$\tau \equiv \frac{BR}{2E \cos \varphi} \quad (8.3)$$

1484 In the present case, magnetic fields are on the order of 1 nT and electric fields are on  
1485 the order of 1 mV/m. A reasonable scale length might be  $10^4$  km, the distance traversed  
1486 by the probe over the course of a half-hour event (notably, back-to-back events are  
1487 unusual).

1488 At a phase of  $80^\circ$ , this timescale is comparable to a  $Pc4$  wave period. At  $135^\circ$ , where  
1489 energy is divided evenly between the standing and traveling wave, the timescale is only  
1490 7 seconds. A wave with a phase so far from  $90^\circ$  would quickly vanish unless it were  
1491 constantly being replenished.

1492 An example of just such an event is shown in Figure 8.10. The left column shows  
1493 electric and magnetic field waveforms in blue and red respectively. The right shows  
1494 the corresponding spectra: imaginary Poynting flux in magenta (corresponding to the  
1495 strength of the standing wave) and real Poynting flux in green (for the traveling wave).  
1496 The black line is a Gaussian fit to the magnitude of the Poynting flux.

1497 The poloidal channel shows a mostly-standing wave, with a phase of  $79^\circ$ . The coherent  
1498 activity in the compressional magnetic field implies a low azimuthal modenumber, and  
1499 thus a fast rotation of energy from the poloidal mode to the toroidal mode. It's likely  
1500 the rotation of energy from the poloidal mode contributes significantly to the toroidal  
1501 mode's lifetime; the toroidal wave's phase is  $130^\circ$ , so its energy should be carried away  
1502 quickly by Poynting flux.

1503 The selection process described in Section 8.1 does not explicitly consider phase. How-  
1504 ever, the discrete Fourier transform is performed over a half-hour time span. An event  
1505 with a comparatively short lifetime would be unlikely to register. It's unsurprising to  
1506 see the events in Figure 8.11 tightly clustered near  $90^\circ$ .

1507 It's further notable in Figure 8.11 that the odd events are more spread out in phase  
1508 than the even events. Near the equator, odd modes have an electric field antinode and  
1509 a magnetic field node; per Equation (8.3), an odd mode's lifetime should be longer than  
1510 that of an even mode with the same phase. Figure 8.11 uses the absolute value of each  
1511 event's phase, as does Figure 8.12.

1512 Unlike amplitude (Section 8.3) and frequency (Section 8.4), events of different phase do  
1513 not seem to exhibit different spatial distributions, as shown in Figure 8.12. Comparisons  
1514 are limited by the small event counts in several of the subplots; however, coarsely  
1515 speaking, events with phases of  $75^\circ$  and worse (left column) show spatial distributions  
1516 more or less in proportion with events phased  $85^\circ$  or better (right column).

## Waveforms and Spectra: Odd Poloidal Wave and Odd Toroidal Wave

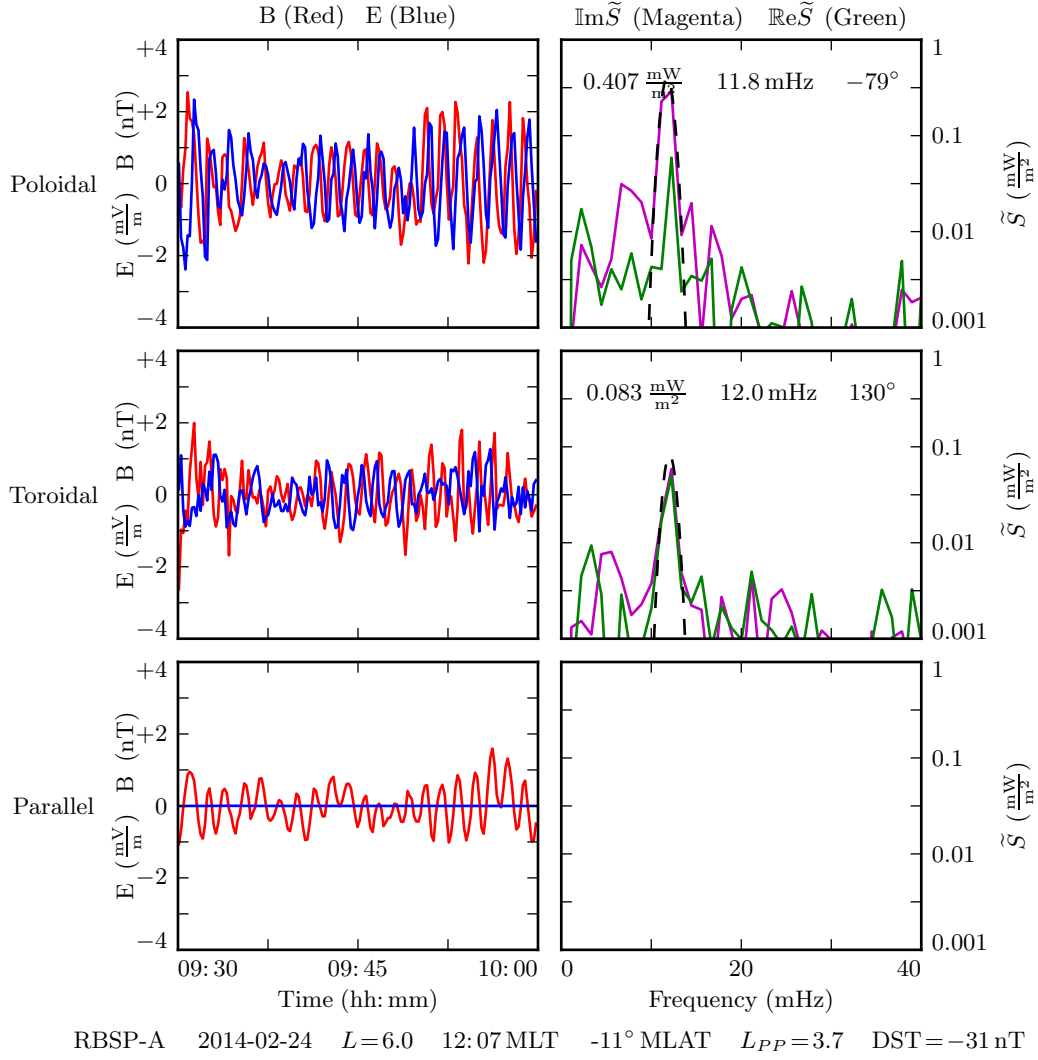


Figure 8.10: The above is a double event, where the poloidal and toroidal channels have been independently selected as events. The poloidal channel shows a wave with most of its energy in the standing wave (phase of  $79^\circ$ ). The toroidal mode has a significant traveling component (phase of  $130^\circ$ ). The compressional activity implies a low modenumber, which would cause energy to rotate quickly from the poloidal mode to the toroidal mode — evidently at a sufficient rate to replenish the losses due to the traveling mode's real Poynting flux.

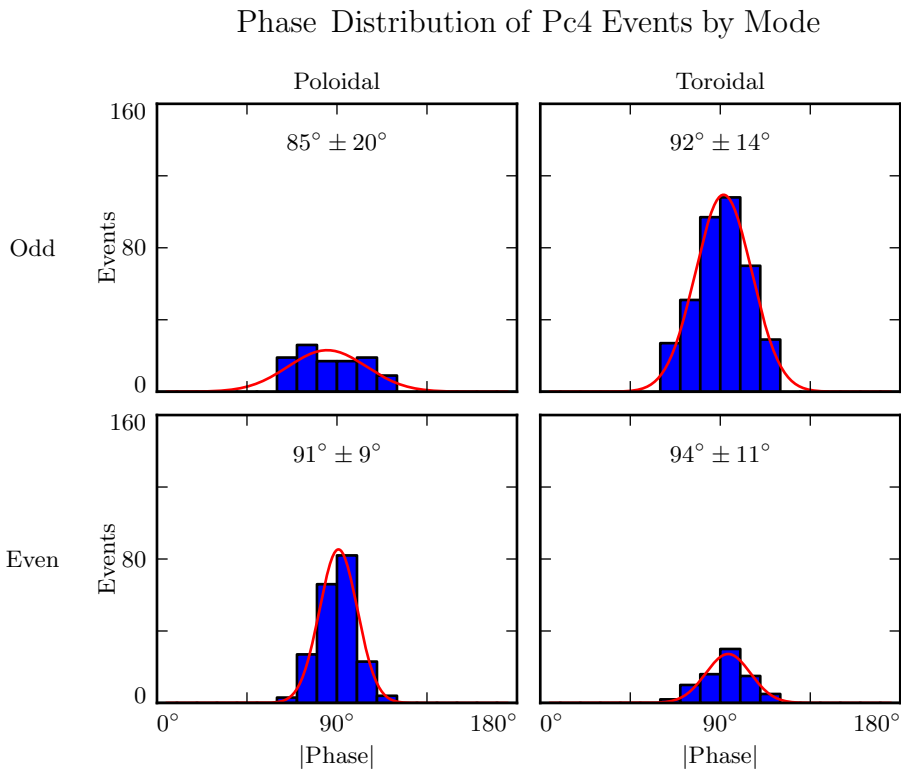


Figure 8.11: The (absolute) phase of the selected Pc4 events is shown above. All modes show phase distributions peaked around  $90^\circ$ . This reflects the fact that a significant traveling wave component quickly carries energy away from an FLR. Odd events are spread more broadly in phase than even events. This is consistent with the odd modes' electric field antinode near the equator, where events are observed; the characteristic loss timescale depends on  $\frac{B}{E}$  per Equation (8.3).

### Distribution of Pc4 Events by Mode and Phase

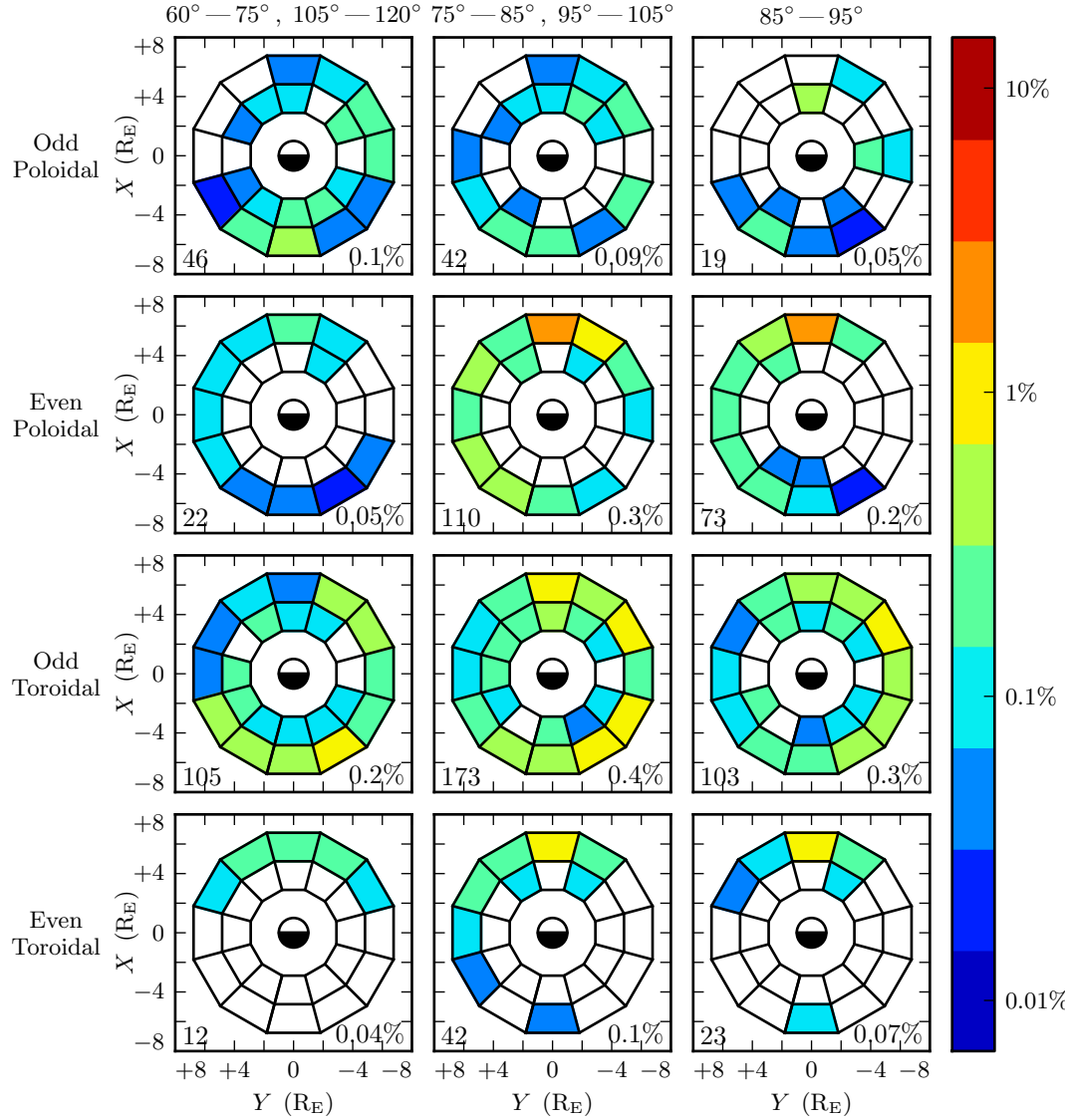


Figure 8.12: The observation rate of events is shown above, divided by (absolute) phase as well as mode. The closer a phase to  $90^\circ$ , the more of an event's energy is in the standing wave, rather than the traveling wave. The spatial distribution of events is more or less consistent between waves with phases very close to  $90^\circ$  and those with a significant traveling wave component.

1517 **8.6 Discussion**

1518 TODO: Odd poloidal events and odd toroidal events are distributed similarly in space.  
1519 Even poloidal events and even toroidal events too. Toroidal events are skewed dayward  
1520 compared to poloidal events, which makes sense, since on the nightside poloidal-to-  
1521 toroidal rotation timescales are comparable to dissipation timescales.

1522 TODO: Poloidal events are mostly even. Toroidal events are mostly odd. Maybe this  
1523 indicates a different preference in modenumber?

1524 TODO: Even poloidal events are skewed toward high amplitude compared to the other  
1525 modes. Stronger even poloidal events are also skewed dayward.

1526 TODO: Odd toroidal events near the top of the Pc4 frequency range exhibit qualitatively  
1527 different behavior from the other odd toroidal modes. They are probably third harmon-  
1528 ics. Maybe third harmonics have a source mechanism more like second harmonics than  
1529 like first.

1530 TODO: Most events have (absolute) phase in the range  $80^\circ$  to  $100^\circ$ , indicating that  
1531 most of the energy is in the standing wave. Odd events are spread a bit more broadly  
1532 in phase. This makes sense, since they ahve an electric field antinode near the equator  
1533 (where measurements are made) which makes them less susceptible to energy loss from  
1534 the traveling wave.

<sub>1535</sub> **Chapter 9**

<sub>1536</sub> **Conclusion**

<sub>1537</sub> **9.1 Summary of Results**

<sub>1538</sub> TODO: Code development... Chapters 5 and 6

<sub>1539</sub> TODO: Make the Git repository public, and link to it.

<sub>1540</sub> TODO: Numerical results... Chapter 7

<sub>1541</sub> TODO: Re-summarize the Discussion sections, I guess.

<sub>1542</sub> TODO: Observational results... Chapter 8

<sub>1543</sub> TODO: Link to the Git repository.

<sub>1544</sub> **9.2 Future Work**

<sub>1545</sub> TODO: Code development.

<sub>1546</sub> Arbitrary deformation of grid. Get  $\hat{e}_i = \frac{\partial}{\partial u^i} \underline{x}$ , then  $g_{ij} = \hat{e}_i \cdot \hat{e}_j$ , then invert the metric tensor for contravariant components.

<sub>1548</sub> MPI. Time to compute vs time to broadcast. This might make sense for inertial length scales.

- 1550 Better ionospheric profiles. Distinction between the dawn and dusk flanks. Maybe even  
1551 update the conductivity based on energy deposition — precipitation causes ionization!
- 1552 IRI ionosphere model. Solar illumination effects.
- 1553 **TODO: Numerical work.**
- 1554 More complicated driving. Higher harmonics, non-sinusoidal waveforms. Maybe even  
1555 drive based on events?
- 1556 Look at the phase of waves in Tuna. How much is standing/traveling?
- 1557 **TODO: Analysis of RBSP data.**
- 1558 Basically just do everything over again, twice as well, once the probes have finished  
1559 sampling the dayside again.

1560

# References

- 1561 [1] H. Alfvén. On the cosmogony of the solar system III. *Stockholms Observatoriums*  
1562 *Annaler*, 14:9.1–9.29, 1946.
- 1563 [2] B. J. Anderson, M. J. Engebretson, S. P. Rounds, L. J. Zanetti, and T. A. Potemra.  
1564 A statistical study of Pc 3-5 pulsations observed by the AMPTE/CCE magnetic  
1565 fields experiment, 1. occurrence distributions. *J. Geophys. Res.*, 95(A7):10495,  
1566 1990.
- 1567 [3] V. Angelopoulos. The THEMIS mission. *Space Science Reviews*, 141(1-4):5–34,  
1568 2008.
- 1569 [4] C. W. Arthur and R. L. McPherron. The statistical character of Pc 4 magnetic  
1570 pulsations at synchronous orbit. *J. Geophys. Res.*, 86(A3):1325, 1981.
- 1571 [5] K. Birkeland. Expédition norvégienne de 1899-1900 pour l'étude des aurores  
1572 boréales. *Mat. Naturvidensk. Kl.*, KI(I), 1901.
- 1573 [6] J. P. Boris. A physically motivated solution of the Alfvén problem. *NRL Memo-*  
1574 *randum Report*, 2167, 1970.
- 1575 [7] A. Brekke, T. Feder, and S. Berger. Pc4 giant pulsations recorded in Tromsø,  
1576 1929-1985. *Journal of Atmospheric and Terrestrial Physics*, 49(10):1027–1032,  
1577 1987.
- 1578 [8] C. W. Carlson, R. F. Pfaff, and J. G. Watzin. The fast auroral Snapshot (FAST)  
1579 mission. *Geophys. Res. Lett.*, 25(12):2013–2016, 1998.

- 1580 [9] A. A. Chan, M. Xia, and L. Chen. Anisotropic alfvén-balloonning modes in Earth's  
1581 magnetosphere. *J. Geophys. Res. Space Physics*, 99(A9):17351–17366, 1994.
- 1582 [10] L. Chen and A. Hasegawa. A theory of long-period magnetic pulsations: 1. steady  
1583 state excitation of field line resonance. *J. Geophys. Res.*, 79(7):1024–1032, 1974.
- 1584 [11] L. Chen and A. Hasegawa. Kinetic theory of geomagnetic pulsations: 1. internal  
1585 excitations by energetic particles. *J. Geophys. Res.*, 96(A2):1503, 1991.
- 1586 [12] C. Z. Cheng and Q. Qian. Theory of ballooning-mirror instabilities for anisotropic  
1587 pressure plasmas in the magnetosphere. *J. Geophys. Res.*, 99(A6):11193, 1994.
- 1588 [13] G. Chisham and D. Orr. Statistical studies of giant pulsations (pgs): Harmonic  
1589 mode. *Planetary and Space Science*, 39(7):999–1006, 1991.
- 1590 [14] W. D. Cummings, R. J. O'Sullivan, and P. J. Coleman. Standing Alfvén waves in  
1591 the magnetosphere. *J. Geophys. Res.*, 74(3):778–793, 1969.
- 1592 [15] L. Dai. Collisionless magnetic reconnection via Alfvén eigenmodes. *Phys. Rev.*  
1593 *Lett.*, 102(24), 2009.
- 1594 [16] L. Dai, K. Takahashi, R. Lysak, C. Wang, J. R. Wygant, C. Kletzing, J. Bonnell,  
1595 C. A. Cattell, C. W. Smith, R. J. MacDowall, S. Thaller, A. Breneman, X. Tang,  
1596 X. Tao, and L. Chen. Storm time occurrence and spatial distribution of Pc4  
1597 poloidal ULF waves in the inner magnetosphere: A Van Allen Probes statistical  
1598 study. *J. Geophys. Res. Space Physics*, 120:4748–4762, 2015.
- 1599 [17] L. Dai, K. Takahashi, J. R. Wygant, L. Chen, J. Bonnell, C. A. Cattell, S. Thaller,  
1600 C. Kletzing, C. W. Smith, R. J. MacDowall, D. N. Baker, J. B. Blake, J. Fennell,  
1601 S. Claudepierre, H. O. Funsten, G. D. Reeves, and H. E. Spence. Excitation of  
1602 poloidal standing Alfvén waves through drift resonance wave-particle interaction.  
1603 *Geophys. Res. Lett.*, 40:4127–4132, 2013.
- 1604 [18] A. W. Degeling, R. Rankin, and Q.-G. Zong. Modeling radiation belt electron  
1605 acceleration by ULF fast mode waves, launched by solar wind dynamic pressure  
1606 fluctuations. *J. Geophys. Res. Space Physics*, 119(11):8916–8928, 2014.

- 1607 [19] W. D. D'haeseleer, W. N. G. H. J. D. Callen, and J. L. Shohet. *Flux Coordinates*  
1608 *and Magnetic Field Structure*. Springer-Verlag, New York, 1991.
- 1609 [20] J. W. Dungey. The attenuation of Alfvén waves. *J. Geophys. Res.*, 59(3):323–328,  
1610 1954.
- 1611 [21] J. W. Dungey. Interplanetary magnetic field and the auroral zones. *Phys. Rev.*  
1612 *Lett.*, 6(2):47–48, 1961.
- 1613 [22] A. Einstein. Die grundlage der allgemeinen relativitätstheorie. *Ann. Phys.*,  
1614 354:769–822, 1916.
- 1615 [23] S. R. Elkington, M. K. Hudson, and A. A. Chan. Acceleration of relativistic  
1616 electrons via drift-resonant interaction with toroidal-mode Pc-5 ULF oscillations.  
1617 *Geophys. Res. Lett.*, 26(21):3273–3276, 1999.
- 1618 [24] M. J. Engebretson, D. L. Murr, K. N. Erickson, R. J. Strangeway, D. M. Klumpar,  
1619 S. A. Fuselier, L. J. Zanetti, and T. A. Potemra. The spatial extent of radial  
1620 magnetic pulsation events observed in the dayside near synchronous orbit. *J.*  
1621 *Geophys. Res.*, 97(A9):13741, 1992.
- 1622 [25] M. J. Engebretson, L. J. Zanetti, T. A. Potemra, and M. H. Acuna. Harmonically  
1623 structured ulf pulsations observed by the ampte cce magnetic field experiment.  
1624 *Geophysical Research Letters*, 13(9):905–908, 1986.
- 1625 [26] M. J. Engebretson, L. J. Zanetti, T. A. Potemra, D. M. Klumpar, R. J. Strange-  
1626 way, and M. H. Acuña. Observations of intense ULF pulsation activity near the  
1627 geomagnetic equator during quiet times. *J. Geophys. Res.*, 93(A11):12795, 1988.
- 1628 [27] S. Fujita and T. Tamao. Duct propagation of hydromagnetic waves in the upper  
1629 ionosphere, 1, electromagnetic field disturbances in high latitudes associated with  
1630 localized incidence of a shear Alfvén wave. *J. Geophys. Res.*, 93(A12):14665, 1988.
- 1631 [28] K.-H. Glassmeier. Magnetometer array observations of a giant pulsation event. *J.*  
1632 *Geophys.*, 48:127–138, 1980.
- 1633 [29] K.-H. Glassmeier. On the influence of ionospheres with non-uniform conductivity  
1634 distribution on hydromagnetic waves. *J. Geophys.*, 54(2):125–137, 1984.

- 1635 [30] K.-H. Glassmeier, S. Buchert, U. Motschmann, A. Korth, and A. Pedersen. Con-  
1636 cerning the generation of geomagnetic giant pulsations by drift-bounce resonance  
1637 ring current instabilities. *Ann. Geophysicae*, 17:338–350, 1999.
- 1638 [31] C. Goertz. Kinetic alfvén waves on auroral field lines. *Planetary and Space Science*,  
1639 32(11):1387–1392, 1984.
- 1640 [32] C. K. Goertz and R. W. Boswell. Magnetosphere-ionosphere coupling. *J. Geophys.*  
1641 *Res.*, 84(A12):7239, 1979.
- 1642 [33] J. Goldstein. Plasmasphere response: Tutorial and review of recent imaging re-  
1643 sults. *Space Science Reviews*, 124(1-4):203–216, 2006.
- 1644 [34] C. A. Green. Giant pulsations in the plasmasphere. *Planetary and Space Science*,  
1645 33(10):1155–1168, 1985.
- 1646 [35] J. L. Green and S. Boardsen. Duration and extent of the great auroral storm of  
1647 1859. *Advances in Space Research*, 38(2):130–135, 2006.
- 1648 [36] C. Greifinger and P. S. Greifinger. Theory of hydromagnetic propagation in the  
1649 ionospheric waveguide. *J. Geophys. Res.*, 73(23):7473–7490, 1968.
- 1650 [37] B. C. Hall. *Lie Groups, Lie Algebras, and Representations*. Graduate Texts in  
1651 Mathematics. Springer, New York, second edition, 2015.
- 1652 [38] Y. X. Hao, Q.-G. Zong, Y. F. Wang, X.-Z. Zhou, H. Zhang, S. Y. Fu, Z. Y.  
1653 Pu, H. E. Spence, J. B. Blake, J. Bonnell, J. R. Wygant, and C. A. Kletzing.  
1654 Interactions of energetic electrons with ULF waves triggered by interplanetary  
1655 shock: Van allen probes observations in the magnetotail. *J. Geophys. Res. Space*  
1656 *Physics*, 119(10):8262–8273, 2014.
- 1657 [39] L. Harang. *Pulsations in the terrestrial magnetic records at high latitude stations*.  
1658 Grondahl, 1942.
- 1659 [40] O. Hillebrand, J. Muench, and R. L. McPherron. Ground-satellite correlative  
1660 study of a giant pulsation event. *Journal of Geophysics Zeitschrift Geophysik*,  
1661 51:129–140, 1982.

- 1662 [41] W. J. Hughes. The effect of the atmosphere and ionosphere on long period mag-  
1663 netospheric micropulsations. *Planet. Space Sci.*, 22:1157–1172, 1974.
- 1664 [42] W. J. Hughes. Magnetospheric ULF waves: A tutorial with a historical perspec-  
1665 tive. In M. J. Engebretson, K. Takahashi, and M. Scholer, editors, *Solar Wind*  
1666 *Sources of Magnetospheric Ultra-Low-Frequency Waves*, volume 81 of *Geophys.*  
1667 *Monogr.*, pages 1–12. American Geophysical Union, Washington, DC, 1994.
- 1668 [43] W. J. Hughes and D. J. Southwood. The screening of micropulsation signals by  
1669 the atmosphere and ionosphere. *J. Geophys. Res.*, 81(19):3234–3240, 1976.
- 1670 [44] W. J. Hughes, D. J. Southwood, B. Mauk, R. L. McPherron, and J. N. Barfield.  
1671 Alfvén waves generated by an inverted plasma energy distribution. *Nature*,  
1672 275(5675):43–45, 1978.
- 1673 [45] J. A. Jacobs, Y. Kato, S. Matsushita, and V. A. Troitskaya. Classification of  
1674 geomagnetic micropulsations. *J. Geophys. Res.*, 69(1):180–181, 1964.
- 1675 [46] T. Karlsson and G. T. Marklund. A statistical study of intense low-altitude electric  
1676 fields observed by freja. *Geophys. Res. Lett.*, 23(9):1005–1008, 1996.
- 1677 [47] Y. Kato and T. Tsutomu. Hydromagnetic oscillations in a conducting medium  
1678 with hall couduct-ivity under the uniform magnetic field. *Science reports of the*  
1679 *Tohoku University. Ser. 5, Geophysics*, 7(3):147–164, 1956.
- 1680 [48] M. C. Kelley. *The Earth’s Ionosphere*. Academic Press, San Diego, second edition,  
1681 1989.
- 1682 [49] R. L. Kessel. Solar wind excitation of pc5 fluctuations in the magnetosphere and  
1683 on the ground. *J. Geophys. Res.*, 113(A4), 2008.
- 1684 [50] D. Y. Klimushkin, P. N. Mager, and K.-H. Glassmeier. Toroidal and poloidal  
1685 Alfvén waves with arbitrary azimuthal wavenumbers in a finite pressure plasma  
1686 in the earth’s magnetosphere. *Annales Geophysicae*, 22(1):267–287, 2004.
- 1687 [51] S. Knight. Parallel electric fields. *Planetary and Space Science*, 21:741–750, 1973.
- 1688 [52] S. Kokubun. Observations of Pc pulsations in the magnetosphere: Satellite-ground  
1689 correlation. *J. Geomagn. Geoelec*, 32(Supplement2):SII17–SII39, 1980.

- 1690 [53] S. Kokubun, K. N. Erickson, T. A. Fritz, and R. L. McPherron. Local time asymmetry of Pc 4-5 pulsations and associated particle modulations at synchronous  
1691 orbit. *J. Geophys. Res.*, 94(A6):6607–6625, 1989.
- 1693 [54] D.-H. Lee and K. Kim. Compressional MHD waves in the magnetosphere: A new  
1694 approach. *J. Geophys. Res.*, 104(A6):12379–12385, 1999.
- 1695 [55] A. S. Leonovich and V. A. Mazur. Structure of magnetosonic eigenoscillations of  
1696 an axisymmetric magnetosphere. *J. Geophys. Res.*, 105(A12):27707–27715, 2000.
- 1697 [56] W. Liu, J. B. Cao, X. Li, T. E. Sarris, Q.-G. Zong, M. Hartinger, K. Takahashi,  
1698 H. Zhang, Q. Q. Shi, and V. Angelopoulos. Poloidal ULF wave observed in the  
1699 plasmasphere boundary layer. *J. Geophys. Res. Space Physics*, 118(7):4298–4307,  
1700 2013.
- 1701 [57] W. Liu, T. E. Sarris, X. Li, S. R. Elkington, R. Ergun, V. Angelopoulos, J. Bonnell,  
1702 and K. H. Glassmeier. Electric and magnetic field observations of Pc4 and Pc5  
1703 pulsations in the inner magnetosphere: A statistical study. *J. Geophys. Res.*,  
1704 114(A12), 2009.
- 1705 [58] W. Liu, T. E. Sarris, X. Li, Q.-G. Zong, R. Ergun, V. Angelopoulos, and K. H.  
1706 Glassmeier. Spatial structure and temporal evolution of a dayside poloidal ULF  
1707 wave event. *Geophys. Res. Lett.*, 38(19), 2011.
- 1708 [59] R. L. Lysak. Magnetosphere-ionosphere coupling by Alfvén waves at midlatitudes.  
1709 *J. Geophys. Res.*, 109, 2004.
- 1710 [60] R. L. Lysak and D. hun Lee. Response of the dipole magnetosphere to pressure  
1711 pulses. *Geophys. Res. Lett.*, 19(9):937–940, 1992.
- 1712 [61] R. L. Lysak and Y. Song. A three-dimensional model of the propagation of Alfvén  
1713 waves through the auroral ionosphere: first results. *Adv. Space Res.*, 28:813–822,  
1714 2001.
- 1715 [62] R. L. Lysak and Y. Song. Nonlocal kinetic theory of alfvn waves on dipolar field  
1716 lines. *Journal of Geophysical Research: Space Physics*, 108(A8), 2003. 1327.

- 1717 [63] R. L. Lysak, C. L. Waters, and M. D. Sciffer. Modeling of the ionospheric Alfvén  
1718 resonator in dipolar geometry. *J. Geophys. Res. Space Physics*, 118, 2013.
- 1719 [64] P. N. Mager and D. Y. Klimushkin. Giant pulsations as modes of a transverse  
1720 Alfvénic resonator on the plasmapause. *Earth, Planets and Space*, 65(5):397–409,  
1721 2013.
- 1722 [65] I. R. Mann, E. A. Lee, S. G. Claudepierre, J. F. Fennell, A. Degeling, I. J. Rae,  
1723 D. N. Baker, G. D. Reeves, H. E. Spence, L. G. Ozeke, R. Rankin, D. K. Milling,  
1724 A. Kale, R. H. W. Friedel, and F. Honary. Discovery of the action of a geophysical  
1725 synchrotron in the Earth’s Van Allen radiation belts. *Nature Communications*, 4,  
1726 2013.
- 1727 [66] I. R. Mann and A. N. Wright. Finite lifetimes of ideal poloidal Alfvén waves. *J.  
1728 Geophys. Res.*, 100:23677–23686, 1995.
- 1729 [67] I. R. Mann, A. N. Wright, and A. W. Hood. Multiple-timescales analysis of ideal  
1730 poloidal Alfvén waves. *J. Geophys. Res.*, 102(A2):2381–2390, 1997.
- 1731 [68] T. Maynard, N. Smith, S. Gonzalez, et al. Solar storm risk to the North American  
1732 electric grid. 2013.
- 1733 [69] R. L. McPherron. The role of substorms in the generation of magnetic storms.  
1734 *Washington DC American Geophysical Union Geophysical Monograph Series*,  
1735 98:131–147, 1997.
- 1736 [70] T. Motoba, K. Takahashi, J. V. Rodriguez, and C. T. Russell. Giant pulsations on  
1737 the afternoonside: Geostationary satellite and ground observations. *J. Geophys.  
1738 Res. Space Physics*, 120:8350–8367, 2015.
- 1739 [71] NASA. Coordinated data analysis (workshop) web.
- 1740 [72] NASA. Near miss: The solar superstorm of july 2012.
- 1741 [73] M. Nicolet. The collision frequency of electrons in the ionosphere. *Journal of  
1742 Atmospheric and Terrestrial Physics*, 3(4):200–211, 1953.
- 1743 [74] L. G. Ozeke and I. R. Mann. Energization of radiation belt electrons by ring  
1744 current ion driven ULF waves. *J. Geophys. Res.*, 113(A2), 2008.

- 1745 [75] E. M. Poulter, W. Allan, E. Nielsen, and K.-H. Glassmeier. Stare radar observations of a PG pulsation. *J. Geophys. Res.*, 88(A7):5668, 1983.
- 1746
- 1747 [76] J. A. Proehl, W. Lotko, I. Kouznetsov, and S. D. Geimer. Ultralow-frequency magnetohydrodynamics in boundary-constrained geomagnetic flux coordinates. *J. Geophys. Res.*, 107(A9):1225, 2002.
- 1748
- 1749
- 1750 [77] H. R. Radoski. A note on oscillating field lines. *J. Geophys. Res.*, 72(1), 1967.
- 1751 [78] H. R. Radoski. A theory of latitude dependent geomagnetic micropulsations: The asymptotic fields. *J. Geophys. Res.*, 79, 1974.
- 1752
- 1753 [79] R. Rankin, J. C. Samson, and V. T. Tikhonchuk. Parallel electric fields in dispersive shear alfvén waves in the dipolar magnetosphere. *Geophys. Res. Lett.*, 26(24):3601–3604, 1999.
- 1754
- 1755
- 1756 [80] B. Rolf. Giant micropulsations at abisko. *J. Geophys. Res.*, 36(1):9, 1931.
- 1757 [81] G. Rostoker, H.-L. Lam, and J. V. Olson. PC 4 giant pulsations in the morning sector. *J. Geophys. Res.*, 84(A9):5153, 1979.
- 1758
- 1759 [82] J. C. Samson, L. L. Cogger, and Q. Pao. Observations of field line resonances, auroral arcs, and auroral vortex structures. *J. Geophys. Res.*, 101(A8):17373–17383, 1996.
- 1760
- 1761
- 1762 [83] H. J. Singer, W. J. Hughes, and C. T. Russell. Standing hydromagnetic waves observed by ISEE 1 and 2: Radial extent and harmonic. *J. Geophys. Res.*, 87(A5):3519, 1982.
- 1763
- 1764
- 1765 [84] D. J. Southwood. Some features of field line resonances in the magnetosphere. *Planetary and Space Science*, 22(3):483–491, 1974.
- 1766
- 1767 [85] D. J. Southwood. A general approach to low-frequency instability in the ring current plasma. *J. Geophys. Res.*, 81(19):3340–3348, 1976.
- 1768
- 1769 [86] J. Stratton and N. J. Fox. Radiation belt storm probes (RBSP) mission overview. In *2012 IEEE Aerospace Conference*. Institute of Electrical & Electronics Engineers (IEEE), 2012.
- 1770
- 1771

- 1772 [87] E. Sucksdorff. Giant pulsations recorded at sodankyl during 19141938. *Terrestrial*  
1773 *Magnetism and Atmospheric Electricity*, 44(2):157–170, 1939.
- 1774 [88] K. Takahashi, J. Bonnell, K.-H. Glassmeier, V. Angelopoulos, H. J. Singer, P. J.  
1775 Chi, R. E. Denton, Y. Nishimura, D.-H. Lee, M. Nosé, and W. Liu. Multipoint  
1776 observation of fast mode waves trapped in the dayside plasmasphere. *J. Geophys.*  
1777 *Res.*, 115(A12), 2010.
- 1778 [89] K. Takahashi, K.-H. Glassmeier, V. Angelopoulos, J. Bonnell, Y. Nishimura, H. J.  
1779 Singer, and C. T. Russell. Multisatellite observations of a giant pulsation event.  
1780 *J. Geophys. Res.*, 116:A11223, 2011.
- 1781 [90] K. Takahashi, M. D. Hartinger, V. Angelopoulos, K.-H. Glassmeier, and H. J.  
1782 Singer. Multispacecraft observations of fundamental poloidal waves without  
1783 ground magnetic signatures. *J. Geophys. Res. Space Physics*, 118:4319–4334, 2013.
- 1784 [91] K. Takahashi, R. W. McEntire, A. T. Y. Lui, and T. A. Potemra. Ion flux oscillations  
1785 associated with a radially polarized transverse Pc 5 magnetic pulsation. *J.*  
1786 *Geophys. Res.*, 95(A4):3717, 1990.
- 1787 [92] K. Takahashi and R. L. McPherron. Standing hydromagnetic oscillations in the  
1788 magnetosphere. *Planetary and Space Science*, 32:1343–1359, 1984.
- 1789 [93] K. Takahashi, N. Sato, J. Warnecke, H. Lühr, H. E. Spence, and Y. Tonegawa.  
1790 On the standing wave mode of giant pulsations. *J. Geophys. Res. Space Physics*,  
1791 97(A7):10717–10732, 1992.
- 1792 [94] B. J. Thompson and R. L. Lysak. Electron acceleration by inertial alfvén waves.  
1793 *J. Geophys. Res.*, 101(A3):5359–5369, 1996.
- 1794 [95] V. T. Tikhonchuk and R. Rankin. Electron kinetic effects in standing shear alfvén  
1795 waves in the dipolar magnetosphere. *Physics of Plasmas*, 7(6):2630, 2000.
- 1796 [96] B. T. Tsurutani, W. D. Gonzalez, G. S. Lakhina, and S. Alex. The extreme  
1797 magnetic storm of 12 september 1859. *Journal of Geophysical Research: Space*  
1798 *Physics*, 108(A7), 2003. 1268.

- 1799 [97] A. Y. Ukhorskiy. Impact of toroidal ULF waves on the outer radiation belt electrons. *J. Geophys. Res.*, 110(A10), 2005.
- 1800
- 1801 [98] J. A. Wanliss and K. M. Showalter. High-resolution global storm index: Dst versus sym-h. *Journal of Geophysical Research: Space Physics*, 111(A2):n/a–n/a, 2006.
- 1802
- 1803 A02202.
- 1804 [99] C. L. Waters, R. L. Lysak, and M. D. Sciffer. On the coupling of fast and shear Alfvén wave modes by the ionospheric Hall conductance. *Earth Planets Space*, 65:385–396, 2013.
- 1805
- 1806
- 1807 [100] C. L. Waters and M. D. Sciffer. Field line resonant frequencies and ionospheric conductance: Results from a 2-d MHD model. *J. Geophys. Res.*, 113(A5), 2008.
- 1808
- 1809 [101] D. M. Wright and T. K. Yeoman. High-latitude HF doppler observations of ULF waves: 2. waves with small spatial scale sizes. *Ann. Geophys.*, 17(7):868–876,
- 1810
- 1811 1999.
- 1812 [102] J. R. Wygant, J. W. Bonnell, K. Goetz, R. E. Ergun, F. S. Mozer, S. D. Bale,
- 1813 M. Ludlam, P. Turin, P. R. Harvey, R. Hochmann, K. Harps, G. Dalton, J. Mc-
- 1814 Cauley, W. Rachelson, D. Gordon, B. Donakowski, C. Shultz, C. Smith, M. Diaz-
- 1815 Aguado, J. Fischer, S. Heavner, P. Berg, D. M. Malsapina, M. K. Bolton, M. Hud-
- 1816 son, R. J. Strangeway, D. N. Baker, X. Li, J. Albert, J. C. Foster, C. C. Chaston,
- 1817 I. Mann, E. Donovan, C. M. Cully, C. A. Cattell, V. Krasnoselskikh, K. Kersten,
- 1818 A. Brenneman, and J. B. Tao. The electric field and waves instruments on the
- 1819 radiation belt storm probes mission. *Space Science Reviews*, 179(1):183–220, 2013.
- 1820 [103] J. R. Wygant, A. Keiling, C. A. Cattell, R. L. Lysak, M. Temerin, F. S. Mozer,
- 1821 C. A. Kletzing, J. D. Scudder, V. Streltsov, W. Lotko, and C. T. Russell. Evidence
- 1822 for kinetic alfvén waves and parallel electron energization at 46 re altitudes in the
- 1823 plasma sheet boundary layer. *Journal of Geophysical Research: Space Physics*,
- 1824 107(A8):SMP 24–1–SMP 24–15, 2002.
- 1825 [104] K. Yee. Numerical solution of initial boundary value problems involving maxwell's
- 1826 equations in isotropic media. *IEEE Trans. Antennas Propagat.*, 14(3), 1966.

- 1827 [105] T. K. Yeoman and D. M. Wright. ULF waves with drift resonance and drift-bounce  
1828 resonance energy sources as observed in artificially-induced HF radar backscatter.  
1829 *Ann. Geophys.*, 19(2):159–170, 2001.
- 1830 [106] Q.-G. Zong, X.-Z. Zhou, X. Li, P. Song, S. Y. Fu, D. N. Baker, Z. Y. Pu, T. A.  
1831 Fritz, P. Daly, A. Balogh, and H. Réme. Ultralow frequency modulation of ener-  
1832 getic particles in the dayside magnetosphere. *Geophys. Res. Lett.*, 34(12), 2007.
- 1833 [107] Q.-G. Zong, X.-Z. Zhou, Y. F. Wang, X. Li, P. Song, D. N. Baker, T. A. Fritz,  
1834 P. W. Daly, M. Dunlop, and A. Pedersen. Energetic electron response to ULF  
1835 waves induced by interplanetary shocks in the outer radiation belt. *J. Geophys.*  
1836 *Res.*, 114(A10), 2009.